Measurement of the Strange Sea of the Proton

A Dissertation Presented to
The Faculty of the Department of Physics
The College of William and Mary in Virginia
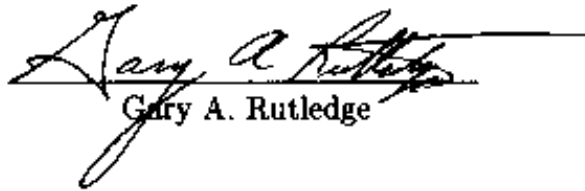
In Partial Fulfillment
Of the Requirements for the Degree of
Doctor of Philosophy
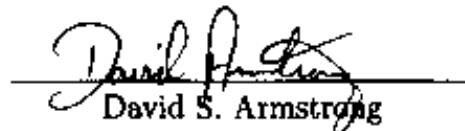
---

by

Gary A. Rutledge
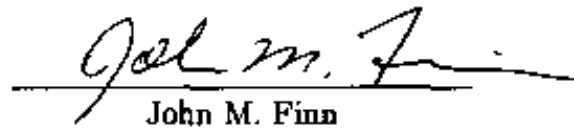
2001

APPROVAL SHEET

This dissertation is submitted in partial fulfillment of
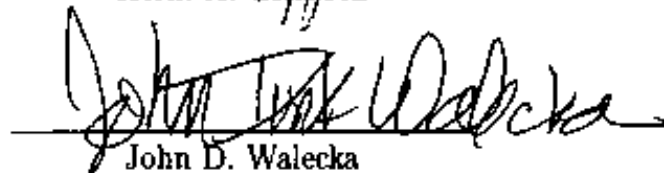
the requirements for the degree of

Doctor of Philosophy

_____

Gary A. Rutledge

Approved, December 2000

_____

David S. Armstrong

_____

John M. Finn

_____

Keith A. Griffioen

_____

John D. Walecka

_____

Jian P. Chen

Jefferson Lab, VA.

In memory of

David Scott Burke

"Only by our spirits and our minds may we experience the wonders of this Universe. Only through discipline of intellect can we unlock the deepest passions of our souls."

–Summer of the Young Lions,
Orcas Island, WA.

Contents

Acknowledgments

A great number of people have contributed to the results of this experiment. A large effort was made by people not usually mentioned in collaboration lists, and without whom this experiment would not have been nearly so successful or pleasant. I would like therefore, to give first mention to the efforts of the support personnel of Jefferson Lab in general and the Hall A staff in particular for their courtesy, humility and competence.

It has been my distinct pleasure to work with Ed Folts and his technical staff: Mark Stevens, Scot Spiegel, Rusty Salmons and Gary Dezern. Without doubt, the attitudes, consideration and open-mindedness of these individuals contributed not only to the unequivocal success of HAPPEX but to the camaraderie and good spirits and group Tao of Hall A in general.

The contributions and efforts of Jack Segal are ubiquitous and so well known that I originally intended not to mention them; But that would have been asinine. Therefore I would like to thank Jack for his instruction, patience, suggestions and advice about things electronic and not electronic.

I would also like to thank Forrest Ellingsworth for his guidance and suggestions in design of HAPPEX components.

I would like to mention that a fundamental success of HAPPEX was the reliability of the Hall A Cryotarget. Special mention is in order for the professionally executed fabrication of hardware by Mark Hoegerl, Steve Knight, and Dave Griffiths. In addition, the control system and GUIs for the Cryotarget were produced and implemented almost exclusively by Kathy McCormick (Old Dominion University) and Fraser Duncan (University of Maryland) with the aid of Johnny Tang (Accelerator Division).

This experiment and its overall success was conducted with the experience and guidance of co-spokespersons Mike Finn and Paul Souder.

And thank you to the DOE and NSF for all the fine money. And finally, my appreciation and thanks to Marie, and my professors, for their patience.

List of Tables

List of Figures

Abstract

The differential cross section for elastic scattering of longitudinally-polarized electrons from protons exhibits a parity-violating asymmetry, due to the interference between weak and electromagnetic amplitudes. The asymmetry is extracted from the detector counting rates as $A^{PV} = (D_r - D_l)/(D_r + D_l)$ where $D_{r(l)}$ are related to the right (left) differential cross sections σ_r, σ_l respectively. Thus $A^{PV} = (\sigma_r - \sigma_l)/(\sigma_r + \sigma_l)$ for right-handed and left-handed electrons. This asymmetry is sensitive to the presence of strange sea quarks in the proton, in particular to the strange vector matrix elements G_E^s and G_M^s.

In an experiment performed in April-May 1998 and May 1999 in Hall A at the Continuous Electron Beam Accelerator Facility (CEBAF) at Jefferson Lab, data were obtained for a total of 179.6 Coulombs of incident electrons. Elastically-scattered electrons corresponding to an average $Q^2 = 0.477(\text{GeV}/c)^2$ were detected in a pair of high-resolution spectrometers.

The excellent stability of the CEBAF beam led to negligible contribution from false asymmetries; Averaged over the experiment, the helicity-correlated beam position differences were less than 10nm and the helicity-correlated beam intensity asymmetries were less than 1 ppm.

The result $A^{PV} = -15.05 \pm 0.98(stat) \pm 0.56(syst)$ ppm was measured at the kinematic point $\langle \theta_{\text{lab}} \rangle = 12.3°$ and $\langle Q^2 \rangle = 0.447$ $(\text{GeV}/c)^2$. Comparing the experimental asymmetry with the theoretical asymmetry, A_{th}, allows extraction for the value of the strange form factor $(G_E^s + 0.392 G_M^s)/(G_M^p/\mu_p) = 0.069 \pm 0.056 \pm 0.039$, where the first error is experimental and the second arises from uncertainty in the electromagnetic form factors.

MEASUREMENT OF THE
STRANGE SEA
OF THE PROTON

Chapter 1

Introduction

"Why does it do that?" - Our basic curiosity and our desire to understand the causal effects of the universe always leads us to ask this question. The answers invariably bring up the question again. This process has lead us to develop a structured philosophy for exploring the very essence of matter. The process of curiosity has become, itself, a tool for exploration. It leads us from basic questions about our universe to questions about our understanding of nuclear structure. This, in turn, leads us to questions about our models of the universe.

Early explorers such as Rutherford, Thompson, Millikan (to name a but a few) gave us the electron and much of its subtlety. At the time, people asked 'what is the importance of the electron?'. The answer to this is self-evident today. When we look at the accomplishments of our technological society, based on our understanding of the electron, it is then with awe that we look to the potential of our expanding knowledge of particle physics. The powerful promise of things to come from this new knowledge, drive us to investigate thoroughly, the subatomic world, in a rigorous and deliberate manor.

We build our understanding of nuclear structure into models which help guide our studies of deeper and deeper subtleties of sub-atomic particles. Insights gained from these investigations are then used to modify and reshape our models.

Investigations into nuclear structure over the past five decades have tested the theoretical descriptions of the nucleon. Models have been built, which explain, fairly well, the standard, daily workings of the atomic and subatomic world. This, the 'Standard Model', is subject to further inquiry as answers are sought for questions

1

which do not yet fit within its scope.

Coming back to our understanding of the electron, we use it now to probe the structure of the nucleon. Here, we build experiments designed to test the workings of our models. As we broaden the scope of our questions, we learn not only the physical basics of nuclear structure, but we learn to ask about the implications of this structure. In this way our understanding guides us to further questions, deeper understanding, and better models.

From these experiments we learn for example, the nucleon consists of three valence quarks which give it most of its structure. As we explore the working of our nuclear models, we know, for instance, that a majority of the nucleon's momentum is carried by the binding forces within the nucleon.

These binding forces also give rise to a 'sea' of quark-antiquark pairs within the nucleon. To build a useful description of the nucleon's properties one must establish all of its relevant degrees of freedom. Results from some of these investigations, such as data from deep inelastic scattering experiments and π-N scattering, suggest strange-quark pairs may be abundant in this sea. Now, we ask, "What is the importance of this quark sea?", or "how much to the $s\bar{s}$ pairs contribute to the proton's charge radius and magnetic moment distribution?". In pursuit of these questions we strive to contribute to the understanding of the Standard Model.

The following chapters will describe the investigation into this question starting with the description of the electromagnetic properties of the nucleon and the role of strangeness in chapter 2, the theoretical development of this inquiry in chapter 3, the experimental devices and methods in chapter 4, and analysis of the data, results and discussion in chapters 5 and 6, respectively.

Chapter 2

Strange Quarks in the Nucleon

2.1   Quark model of the nucleon

The proton consists of three "valence" quarks: two up quarks and a down quark. Its isospin partner, the neutron, consists of an up and two down valence quarks. They are called valence (in analogy to the valence electrons of atomic theory) because within the quark model they govern much of the nucleon's behavior. Binding these quarks together is the strong force mediated by gluons. Besides holding the nucleon together, the gluons also determine much of the phenomenology of the proton. For instance, from deep inelastic electron-proton scattering experiments (DIS) it is known that only $\approx 50\%$ of the proton's momentum is carried by charged particles (quarks). The uncharged gluons are believed to carry the rest.

The gluons play another important role inside the proton, by occasionally fluctuating into quark-antiquark pairs. In principle, any flavor of quark (u, d, s, c, b, or t) may be created, along with its antiparticle. The mean life time for $q\bar{q}$ pairs falls inversely with the mass of the quark species being produced, thus the extremely heavy $c\bar{c}$, $b\bar{b}$ and $t\bar{t}$ quark pairs, while possible, should be relatively rare inside the proton. A reasonable model of the nucleon ground state therefore, could consist primarily of the u, and d valence quarks and the $u\bar{u}$, $d\bar{d}$ and $s\bar{s}$ pairs, along with the gluons. These $q\bar{q}$ pairs comprise the quark "sea" inside the proton (see Fig. 2.1).

3
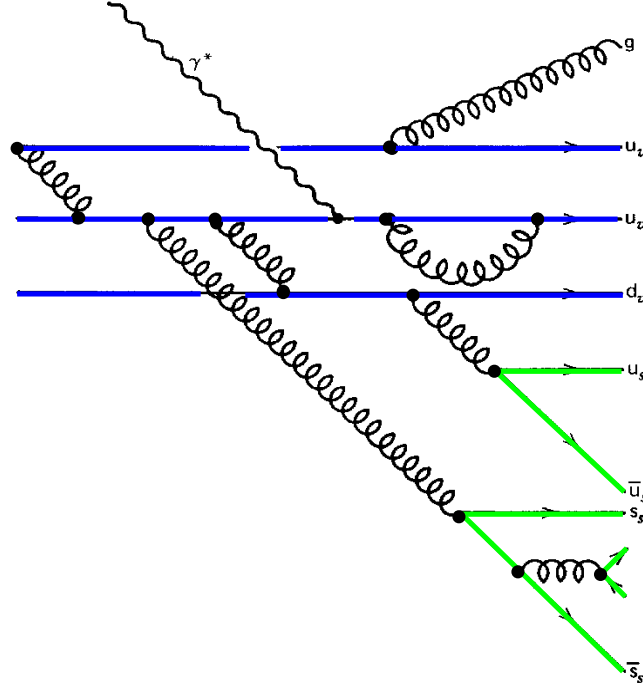
Figure 2.1: The proton has a complex structure with three valence quarks and a sea of quark-antiquark pairs created by gluons.

2.2 The Electromagnetic Structure of the Nucleon

The electromagnetic structure (i.e., the charge and current distributions) of the nucleon is described by electromagnetic form factors which depend not only on valence quarks but also on the sea.

At relativistic energies, Rutherford's formula for scattering off of a point charge must be expanded to include the spins of the electron and of the target. The Mott cross-section, which describes electron scattering and includes the spin effects of the electron, may be written[1]

$$\left(\frac{d\sigma}{d\Omega}\right)^*_{Mott} = \left(\frac{d\sigma}{d\Omega}\right)_{Rutherford} \left(1 - \beta^2 \sin^2 \frac{\theta}{2}\right), \quad \text{with} \ \ \beta = \frac{v}{c}. \tag{2.1}$$

where θ is the angle of the scattered electron with respect to the beam.

In the case of extremely relativistic electrons, where

$$\lim_{v \to c} \left(1 - \beta^2 \sin^2 \frac{\theta}{2}\right) = \cos^2 \frac{\theta_{lab}}{2}. \tag{2.2}$$

the Mott cross-section becomes

$$\left(\frac{d\sigma}{d\Omega}\right)^*_{Mott} = \left(\frac{d\sigma}{d\Omega}\right)_{Rutherford} \left(\cos^2\frac{\theta}{2}\right) = \frac{4Z^2\alpha^2(\hbar c)^2 E'^2}{|Qc|^4}\cos^2\frac{\theta}{2}. \qquad (2.3)$$

where Z is the number of electrons in the neutral target,

$\quad E'$ is the energy of the scattered electron,

$\quad \alpha$ is the fine structure constant, and

$\quad Q^2$ is the negative of the square of the four-momentum.

The asterisk indicates nucleon that recoil has been neglected. The Mott cross-section works well enough in the limit as $|q| \to 0$. At larger values, the wavelength of the photon decreases and spatial resolution increases. The scattered electron no longer "sees" the total charge of the nucleon, but only parts of it. The cross-section therefore decreases. To account for the phenomenological effects of reduced cross-section at higher q^2, we introduce the 'form factor', $F(Q^2)$ which is dependent only upon the 4-momentum transfer, $Q^2 = -q_\mu q^\mu$.

$$\left(\frac{d\sigma}{d\Omega}\right)_{exp} = \left(\frac{d\sigma}{d\Omega}\right)^*_{Mott} \left|F(Q^2)\right|^2 \qquad (2.4)$$

The form factor $F(Q^2)$ is the Fourier transform of the charge distribution $\rho(\vec{x})$:

$$F(Q^2) = \int e^{i\vec{q}\cdot\vec{x}/\hbar}\rho(\vec{x})d^3x \qquad (2.5)$$

At momentum transfers on the order of the proton's rest energy, the Mott cross-section is modified to include non-negligible target recoil. In addition, two form factors are required, which describe both the electric and magnetic distributions. Using these Dirac and Pauli form factors the elastic scattering cross-section becomes[2]

$$\left(\frac{d\sigma}{d\Omega}\right)_{exp} = \left(\frac{d\sigma}{d\Omega}\right)^*_{Mott} \frac{E'}{E}\left[F_1^2 + \frac{Q^2}{4M^2}\left(2(F_1+F_2)^2\tan^2\left(\frac{\theta}{2}\right) + (F_2)^2\right)\right], \quad (2.6)$$

where M is the mass of the nucleon, F_1 is the Dirac form factor and F_2 is the Pauli form factor and E'/E accounts for target recoil[3].

2.2.1   Dirac, Pauli and Sachs Form Factors

The interpretation of the Dirac and Pauli form factors is seen in the limit as $Q^2 \to 0$. Then

$$F_1^p \to 1, \ F_2^p \to 1, \ F_1^n \to 0, \ \text{and} \ F_2^n \to 1, \qquad (2.7)$$

The Dirac and Pauli form factors are not, however, the most convenient formalism. Due to the $(F_1 + F_2)^2$ term in Eqn. 2.6 for example, these form factors lead to an entanglement of cross terms which make separate extraction from experiment difficult. Instead we can use different linear combinations to eliminate the cross terms. This set is known as the 'Sachs' form factors and are linearly related to the Pauli and Dirac form factors as[4]:

$$G_E^p(Q^2) = F_1^p(Q^2) - \tau F_2^p(Q^2) \qquad G_E^n(Q^2) = F_1^n(Q^2) - \tau F_2^n(Q^2)$$
$$G_M^p(Q^2) = F_1^p(Q^2) + F_2^p(Q^2) \quad , \text{ and } \quad G_M^n(Q^2) = F_1^n(Q^2) + F_2^n(Q^2) \qquad (2.8)$$

where $G_E(Q^2)$, $G_M(Q^2)$ are the electric and magnetic form factors, respectively, and $\tau = Q^2/4M^2$.

Rewriting Eqn. 2.6 in terms of the Sach's form factors, the cross-section for the scattering of an electron off a nucleon is described by the *Rosenbluth formula*[5]:

$$\left(\frac{d\sigma}{d\Omega}\right)_{exp} = \left(\frac{d\sigma}{d\Omega}\right)_{Mott}^* \frac{E'}{E} \left[\frac{G_E^2(Q^2) + \tau G_M^2(Q^2)}{1 + \tau} + 2\tau G_M^2(Q^2) \tan^2\frac{\theta_e}{2}\right] \qquad (2.9)$$

In this new formalism, the cross terms disappear and $G_E^{n,p}$ and $G_M^{n,p}$ can be separated directly from the data using the Rosenbluth technique.[1, 3, 5].

In order to independently determine $G_E(Q^2)$ and $G_M(Q^2)$, the cross-sections must be measured at fixed values of Q^2 for various scattering angles θ. The measured cross-sections are then divided by the Mott cross-sections. A linear fit is then made of Eqn. 2.9 to the data. In the limiting case as $Q^2 \to 0$, G_E coincides with the electric charge of the target, normalized to units of electron charge, and G_M is equal to the magnetic moment μ of the target, normalized to the nuclear magneton[1]. The limiting values are:

$$G_E^p(Q^2 = 0) = Z_p = 1 \qquad G_E^n(Q^2 = 0) = Z_n = 0$$
$$G_M^p(Q^2 = 0) = \mu_p \cong 2.79 \quad G_M^n(Q^2 = 0) = \mu_n \cong -1.91 \qquad (2.10)$$

The elastic form factors reflect the spatial distribution of the charge and magnetic moment in the nucleon. Since the charge of the nucleon is carried by the quarks, therefore the electromagnetic form factors describe the distributions of these charges within the nucleon and thus relate to the distribution and movement of the quarks. As fundamental properties of the nucleon, the behavior of these form factors should be predicted by any theoretical model of the nucleon's structure.

2.2.2   Proton Form Factors

2.2.2.1 G_M^p

The magnetic form factor of the proton, G_M^p has been well measured through a momentum transfer range of $0 < Q^2 < 8\,(GeV/c)^2$[6, 7], with an accuracy of better than 5%. In the momentum region we are interested in $(Q^2 \simeq 0.5(GeV/c)^2)$, it is
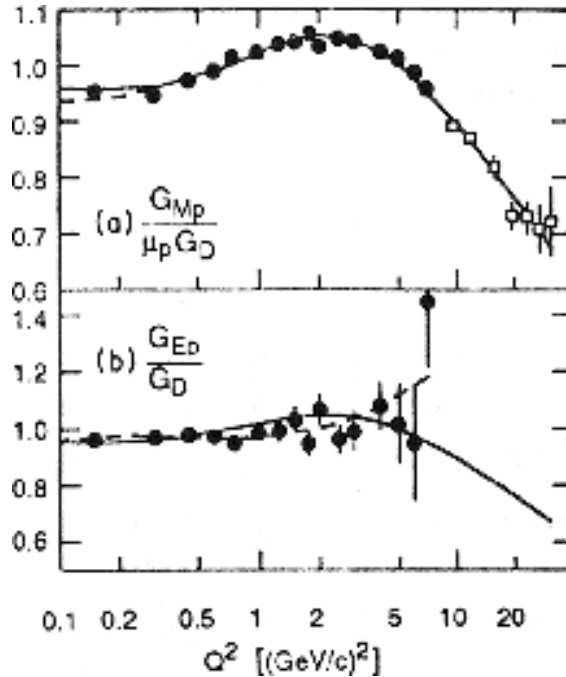
Figure 2.2: World Data for G_M^p[6]. The upper plot in this figure shows the Bosted fit for $G_M^p/(\mu_p G_D)$.

known to $\sim$ 2-3%.

All data on G_M^p up to the previous decade have been obtained using the Rosenbluth separation technique using the form of Eqn. **??**. This method is dependent on knowledge of the electron's energy, the total luminosity and the detector acceptance. Kinematically, G_M^p dominates the cross section at high Q^2 due to the factor $\tau = Q^2/4M^2c^2$. As a result it is easily measured. As a reliable description of the proton's magnetic moment, G_M^p is then used in extracting other nucleon form factors. Measurements are frequently cast as a ratio to G_M^p in the form of $\mu_p G_E^p/G_M^p$, $\mu_n G_M^n/G_M^p$ and $\mu_p G_E^p/G_M^p$.

Most papers quote the form factors relative to the empirical dipole fit of G_M^p.

$$G_M^p(Q^2) = \mu_p G^{dipole}(Q^2) \cong 2.79 \left(1 + \frac{Q^2}{0.71(GeV/c)^2}\right)^{-2} \tag{2.11}$$

An exponential radial distribution of the protons charge would imply such a dipole form factor. This lacks, however, physical motivation and is not a precise description of the proton's magnetic form factor, as shown in Fig. 2.2.

2.2.2.2 G_E^p

The proton's electric form factor, G_E^p, is the Fourier transform of the proton's charge distribution in the Breit frame. This was first demonstrated by Hofstadter at SLAC in the 1950's when he showed the proton was not a point particle and thus had structure[8]. At higher energies, the proton's electric properties show substructure indicating the presence of a combination of charges within the proton. Although the shape of the proton's charge distribution can be qualitatively explained with the quark model of the nucleon, the detailed charge distribution must be determined by experiment.

G_E^p has been accurately measured at low Q^2[7]. Accuracy at higher Q^2 using the Rosenbluth technique becomes more difficult as the cross-section becomes dominated by G_M^p. In addition, these data are limited by systematic error which makes interpretation of the results difficult. The systematic errors can be reduced by scattering longitudinally-polarized electrons off of hydrogen and measuring the ratio of transverse, (P_t) to longitudinal, (P_l) polarization of the recoiling proton. The ratio of the form factors is [16]

$$\frac{G_E^p}{G_M^p} = -\frac{P_t}{P_l} \frac{(E + E')}{2M_p} \tan\left(\frac{\theta_e}{2}\right). \tag{2.12}$$

The first measurements using this technique were conducted at MIT-Bates[17] to measure G_E^p/G_M^p at low Q^2. Recent work by Jones *et al.* [9] in Hall A at JLab further improves these numbers. In particular, the recent JLab data shown in Fig. 2.4 shows a marked reduction in G_E^p/G_M^p with increasing Q^2. Since G_M^p closely follows the dipole parameterization, as can be seen in Fig. 2.2, the decreasing values in Fig. 2.4 implies that G_E^p falls with Q^2 faster than the dipole model.
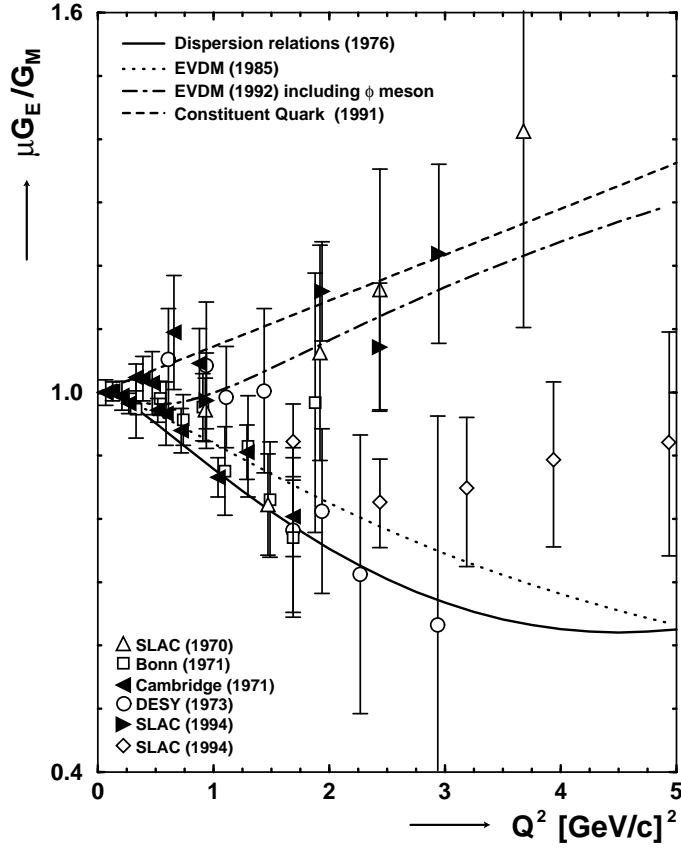
Figure 2.3: The ratio of $\mu_p G^p_E / G^p_M$ as a function of Q^2 determined with the Rosenbluth separation technique. Data symbols are explained in ref. [9]. Theory: full[7], dotted, [10], dashed[11], dash-dot[12]. See Fig. 2.4 for results obtained using the polarization transfer technique.

2.2.3   Neutron Form Factors

Measuring the electromagnetic form factors of the neutron has proven more challenging. Difficulties arise in that targets with free neutrons do not exist. Measurements of the neutron's form factors have been done indirectly by means of a number of clever techniques. Neutron form factors are measured primarily via scattering off deuterons. Polarized ^{3}He targets are used as well since the spin of this nucleus is primarily carried by the neutron as the proton's spins are anti-aligned($\uparrow+\downarrow=$ spin 0) in keeping with the Pauli principle. The reactions used are, by necessity, quasi-elastic.
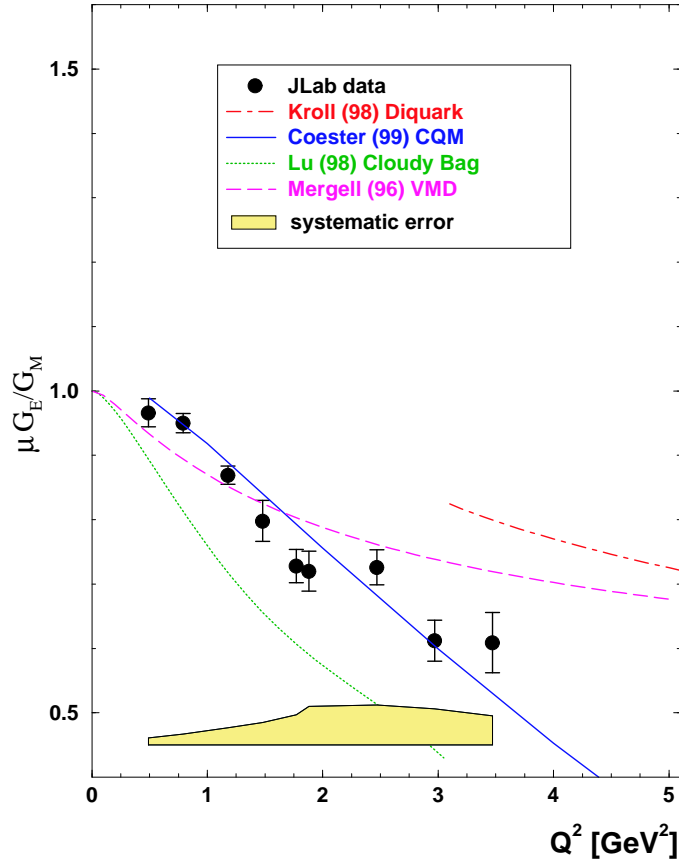
Figure 2.4: JLab data[9] for the ratio of $\mu_p G_E^p/G_M^p$ as a function of Q^2 compared to recent theoretical predictions (full[11], dotted[13], dashed[14], and dot-dashed[15]). The shaded region denotes the size of the systematic error in the data.

2.2.3.1 G_M^n

Until recently, most data on G_M^n have been extracted from elastic and inclusive quasi-elastic electron-deuteron scattering experiments. These techniques require the subtraction of large proton contributions which suffer large systematic uncertainties [18].

Progress in the measurements of G_M^n at low Q^2 has been made recently by measuring the ratio of quasi-elastic neutron and proton knock-out from a deuterium target by detecting the electron in coincidence with the neutron or proton in separate spectrometers[6]. While accuracy improves by refinement of this technique, this method is limited by the absolute calibration of the neutron detection efficiency. The latest results for G_M^n are from Bates[24], Mainz[21], NIKHEF[22] and Bonn[20]. Figure 2.5 shows results of four experiments. The NIKHEF and Mainz detectors
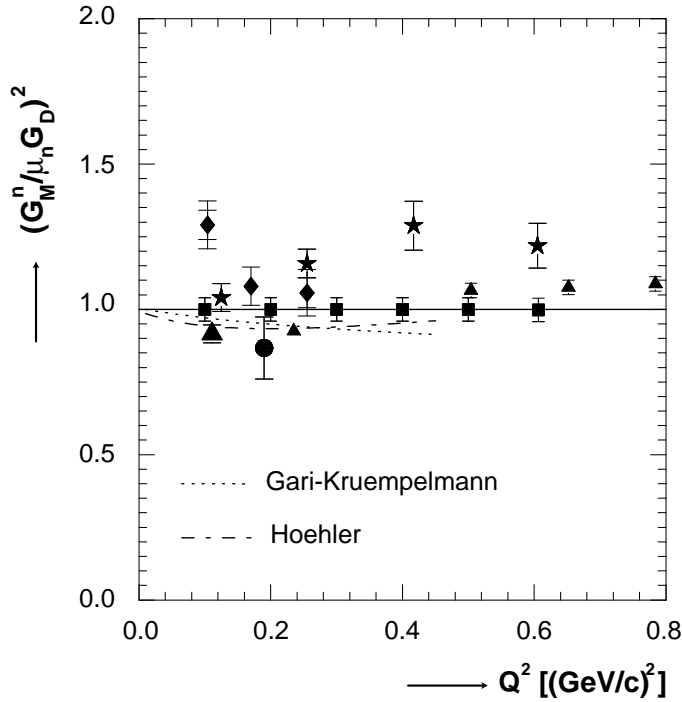
Figure 2.5: Latest Data on $G_M^n/\mu_n G_D$ as a function of Q^2, compared to predictions by Gari[10] and Höhler[7]. Expected precision of JLab experiment E95-001[19] are indicated by the solid squares. The Bonn data[20] are indicated by the stars while the Mainz data[21]are indicated by the small triangles. Data from NIKHEF[22] is indicated by the large triangle and data from Bates is indicated by diamonds[23] and the solid circle[24], respectively.

were calibrated off site (using the kinematically complete $p(n,p)n$ reaction) at the PSI neutron beam facility. The measurements for the Bonn data were calibrated in situ using the $D(\gamma,p)n$ or $p(\gamma,\pi^+)$ reaction. The Bates experiment was calibrated using the $D(\gamma,p)n$ reaction. Systematic differences between these experiments can be seen. In particular, we are interested in knowing the value of G_M^n at $Q^2 = 0.47\ (GeV/c)^2$ where there are data from Bonn and Meinz. The most precise error claim of 1% is quoted by the Mainz group[21]. This number systematically disagrees with the Bonn measurement[20] by 8-10%. The discrepancies among world data indicate that it would be useful to do additional experiments to resolve this issue. A recent experiment in Hall A at JLab, E95-001, has measured G_M^n at $Q^2 \sim 0.2$ by inclusive quasi-elastic scattering of polarized electrons off of a polarized ^{3}He target[19]. Figure 2.5 shows the expected accuracy of experiment E95-001 at JLab which will further illuminate these issues.

2.2.3.2 G_E^n

The initial measurements of the neutron's ele   form factor were done using single arm spectrometers and Rosenbluth separat   Analysis of quasi-elastic electron scattering off of bound neutrons in deuteriun   gets requires the subtraction of the proton's electric form-factor contribution:

$$\frac{d\sigma}{d\Omega}(en) = \frac{d\sigma}{d\Omega}(ed) \qquad (ep) \qquad (2.13)$$

The subtraction of two large numbers from e   other *before* Rosenbluth separation contributes sizable uncertainties to the resu   The most extensive measurements are the elastic scattering results by Platchk   al.[25]. These results have large systematics errors on the order of 50% or s   Platchkov's data are shown as the open circles in Fig. 2.6. The grey band indic   the uncertainty due to the nucleon-nucleon potential. Advances in polarized be   and polarized targets allow a new
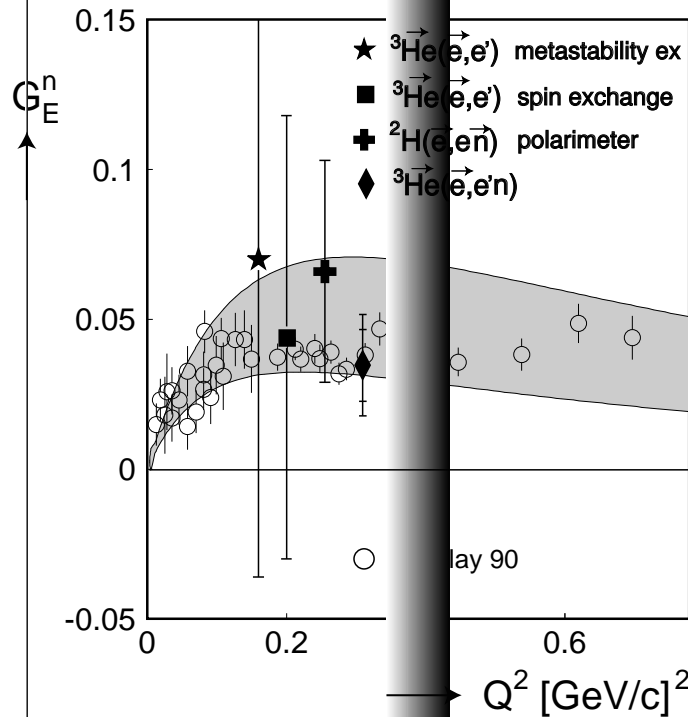
Figure 2.6: Older results for G_E^n as a function of Q^2 are shown as star[26, 27], square[28], cross[29], and diamond[30]. The open circles depict the results of Platchkov *et. al.*[25] using the Paris potential. The shaded area is the systematic uncertainty in the Platchkov (*et. al.*) data due to the choice of the NN-potential.

series of spin-dependent measurements of G_E^n. The ratio of G_E^n/G_M^n can be related

to the scattering asymmetry by[31]:

$$\frac{G_E^n}{G_M^n} = \frac{A_\perp}{A_\parallel}\sqrt{\tau + \tau(1+\tau)\tan^2(\theta_e/2)} \qquad (2.14)$$

where $A \perp (A_\parallel)$ is the asymmetry for target polarization perp   icular(parallel) to the momentum transfer. Complementary measurements can   made using polarization transfer techniques similar to those used by Jones et for G_E^p/G_M^p. The equation is similar to Eqn. 2.12.

A third technique involves using polarized helium in the ^{3}H $\vec{e}, e'$) reaction. Re-cent results using this method are shown in Fig. 2.7.
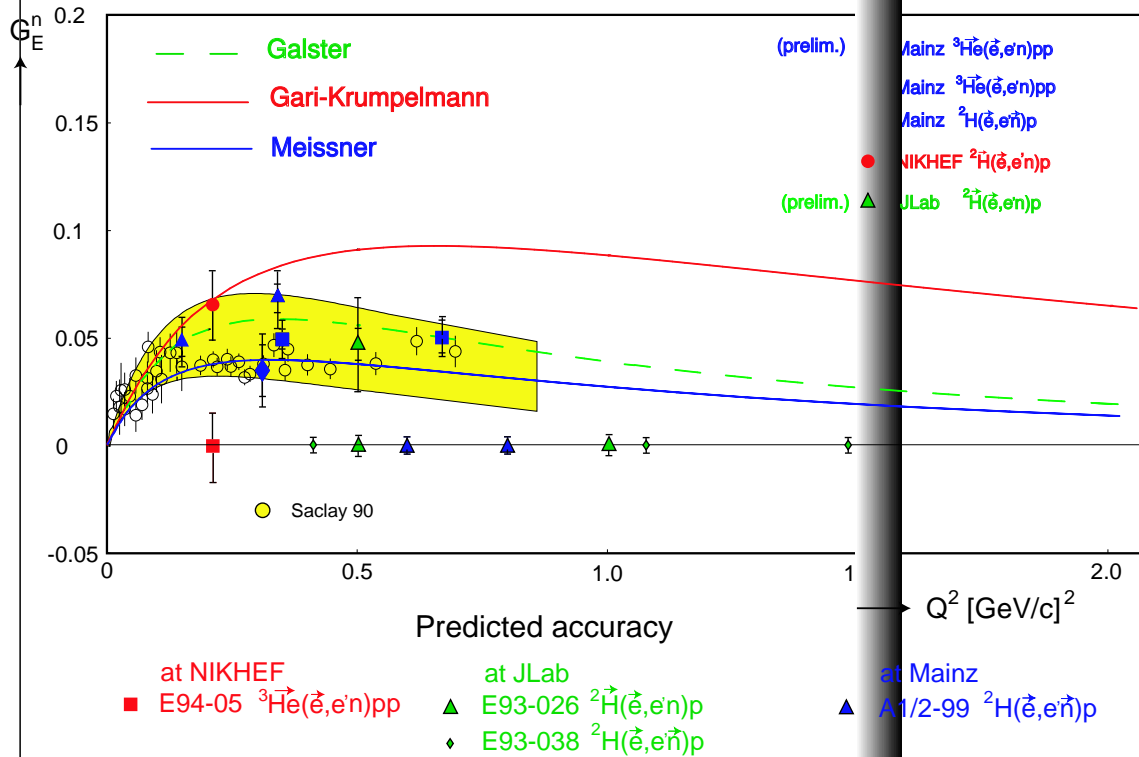
Figure 2.7: Recent data on G_E^n as a function of Q^2 expressed as solid circle[32], solid triangle[33, 34],solid square[35, 31] and solid diamond[36]. Expected precision of future results expressed as open square[37], open diamond[38], open triangle[39]. These are compared with three theoretical calculations (full[10], dashed[40], and dotted line[41])

Recent and planned experiments at JLab will further improve our knowledge of this form factor. G_E^n is currently being measured by Madey et $al.$[38] and Day et $al.$[39]. These results are expected to have an error of 8% and 8.9% respectively.

Theoretical models have yet to satisfactory describe the observed behavior of G_E^n. Currently, the empirical Galster-Dipole parameterization[41]:

$$G_E^n \cong \frac{-\mu_n \tau}{1 + 5.6\tau} G_D(Q^2) \qquad (2.15)$$

is commonly used to empirically describe the data.

2.2.4   QCD model of nucleons

The quark substructure of the nucleon was proposed by Gell-Mann in 1963. This developed further into a consistent field theory of quark and gluon interactions, known as Quantum Chromodynamics (QCD). Prior to the development of QCD, the constituent-quark model of the nucleon suggested the quark-gluon sea was 'inert', that is, that the sea quarks played little role in the properties of the proton such as its charge radius or magnetic moment. Details of the properties of antiquarks and gluons in the proton were not considered important.

As a fundamental theory, QCD is well accepted for describing the theory of the strong interactions of nucleon behavior. However, a complete description of nucleon structure in the non-perturbative regime, using quarks and gluons as the fundamental degrees of freedom in the QCD Lagrangian, has not yet been achieved.

Data from DIS on spin-structure functions in 1988[42, 43, 44] leading to the famous "spin crisis" changed this perception of the 'inertness' of the sea. Specifically, the data could be interpreted to mean that gluons, antiquarks and non-valence quarks all contribute to the spin of the nucleon and therefore represent relevant degrees of freedom for describing the proton at low energy. In other words, it is possible for the virtual photon in in any electromagnetic process to couple to one of the sea quarks, so these sea quarks should really be included in our description of the proton.

The question is: How much to include? How much, for example, do the sea quarks contribute to the charge radius of the proton? How much do the strange quarks contribute to the momentum of the proton? Since the nucleon has, by definition, no net strangeness, there can be no strange valence quarks. Strange quarks may only exist as sea quarks. Thus testing for strange-sea quarks will tell us something about sea quarks in general.

2.3   Strange Quarks

One model of the nucleon, the "Valence Quark Model" depicts the nucleon as consisting solely of u and d quarks[45]. This model predicts many of the low-energy properties of the nucleon. There is evidence, however, that some of the nucleon's low-energy energy properties cannot be accounted for without the presence of heavier sea quarks. For example, the $\pi N \sigma$ term from low-energy π-N scattering suggests that the $s\bar{s}$ pairs may contribute $\sim 36\%$ of the nucleon's mass. This is significant and suggests that the nucleon matrix elements of other strange-quark operators could differ non-negligibly from zero. In addition, deep inelastic scattering experiments such as E154 at SLAC[46, 47] and the spin muon collaboration (SMC) at CERN[48] have measured that $\sim 30\%$ of the proton's spin arises from all quarks. The remainder is largely attributed to gluons or orbital angular momentum of valence quarks.

Prior to 1994, no experimental constraints had been published for the strange quark charge or magnetic form factors, G_E^s and G_M^s. These are related to the nucleon form factors by 3.40 and 3.41. In predicting these form factors, one rigorous constraint is placed on G_E^s: It must vanish at $Q^2 = 0$; we require the nucleon to have no net strangeness.

Aside from this requirement, theoretical predictions differ (dramatically) on the size of the strange form factors, $G_{E,M}^s$. It is convenient to characterize the low-Q^2 behavior of G_E^s as a dimensionless mean-square "strangeness radius", ρ_s. This is defined as

$$\rho_s \equiv \left. \frac{dG_E^s}{d\tau} \right|_{\tau=0} = -\frac{2}{3}M^2 \left\langle r^2 \right\rangle^{(s)} - \mu_s, \quad \mu_s \equiv G_M^s(0). \tag{2.16}$$

where r^2 is the strange radial charge distribution.

Theoretical predictions for ρ_s are given in Table 2.1.

There is a great deal of theoretical interest in determining G_E^s and G_M^s at low Q^2 due to the role strange quark pairs may play in understanding non-perturbative QCD. Many models propose estimates on the impact strange quarks may have on the nucleon's properties. Measuring the strange quark content, then, will place limits on these models and guide refinements in QCD theory and the description of the standard model.

However, measuring the strange quark form factors is not easy. Separation of these form factors is difficult because all three, G_E^s, G_M^s and the strange axial form

Source	$r_s^2(fm^2)$	ρ_s	μ_s	Reference
Poles	0.16	-2.10	-0.31	Jaffe[49]
Poles (update)	0.21	-2.93	-0.24	Hammer[50]
Poles + $K\overline{K}$	-0.15 → +0.42	-6.0 → +2.65	-0.51 →-0.26	Hammer 2[51]
NJL model	-0.2	3.06	-0.05	Weigel[52]
SU(3) Skyrme model	-0.19	3.19	-0.33	Park[53]
SU(3) Skyrme, broken symm.	-0.10	1.64	-0.13	Park 2[54]
Lattice	-0.16 → -0.06	1.26 → 2.77	-0.56 →-0.16	Liu[55]
Quark Model	-0.04	0.57	0.035	Isgur[56]

Table 2.1: Various predictions of the leading moments of the strange quark form factors.

factor, G_A^s, contribute to the elastic scattering of electrons from the proton. This is further complicated by uncertainty in the knowledge of the form factors $G_{E,M}^{n,p}$ which are necessary to extract the values of $G_{E,M,A}^s$.

The study of parity violation of neutral weak matrix elements can be used to determine the strange quark form factors, G_E^s and G_M^s. This will be discussed in the next chapter.

Chapter 3

Parity-Violating Electron Scattering

3.1   Parity violation in electron scattering

The total cross-section for the elastic scattering of polarized electrons from protons
is described by the Feynman diagrams in Fig. 3.1.

$$\left| \begin{array}{c} e^{-\prime} \qquad P' \\ \\ \\ e^- \qquad\quad P \end{array} \right|^2 = \left[\begin{array}{c} e^{-\prime} \quad P' \quad e^{-\prime} \quad P' \quad e^{-\prime} \quad P' \\ \gamma \qquad\quad Z^0 \\ e^- \quad P \quad e^- \quad P \quad e^- \quad P \end{array} + \cdots \right]^2 \qquad (3.1)$$

Figure 3.1: Elastic ^{1}H$(\vec{e}, e')$ scattering amplitudes. The total amplitude of polarized elastic
scattering of electrons from protons is shown on the left. The blob is the combination of
processes which contribute to the overall cross-section. Shown on the right are a few of the
lowest order diagrams. The cross section in Eqn. 3.2 is calculated with only the first-order
amplitude terms.

The total scattering cross-section for elastic $e-p$ scattering is proportional
to the square of the sum of amplitudes for the scattering processes involved. Ignoring

higher order processes for the moment, this gives:

$$\sigma_{total} \propto |\mathcal{M}_\gamma + \mathcal{M}_{Z^0}|^2 = |\mathcal{M}_\gamma|^2 + 2\Re e(\mathcal{M}_\gamma \mathcal{M}_{Z^0}) + |\mathcal{M}_{Z^0}|^2 \tag{3.2}$$

The scattering cross-section will consist of a helicity-independent piece (dominated by the γ exchange amplitude) and a helicity-dependent part which will violate parity (due to quantum interference between the electromagnetic and neutral weak amplitudes). The total scattering cross-section will therefore violate parity[57]. We can define an asymmetry as the ratio of helicity-dependent to helicity-independent cross-sections. We do this by defining a parity-violating asymmetry

$$A^{\mathrm{PV}} = \frac{\sigma_R - \sigma_L}{\sigma_R + \sigma_L} \tag{3.3}$$

where $\sigma_{R(L)}$ is the cross-section for the right(left) handed helicity states of the electron.

Substituting Eqn. 3.2 into 3.3 and using $\mathcal{M}_\gamma^R = \mathcal{M}_\gamma^L = \mathcal{M}_\gamma$ and $\mathcal{M}_{Z^0} \ll \mathcal{M}_\gamma$ we see that

$$\begin{aligned} A^{\mathrm{PV}} &= \frac{|\mathcal{M}_\gamma^R + \mathcal{M}_{Z^0}^R|^2 - |\mathcal{M}_\gamma^L + \mathcal{M}_{Z^0}^L|^2}{|\mathcal{M}_\gamma^R + \mathcal{M}_{Z^0}^R|^2 + |\mathcal{M}_\gamma^L + \mathcal{M}_{Z^0}^L|^2} \\ &\simeq \frac{\Re e(\mathcal{M}_\gamma \mathcal{M}_{Z^0})_R - \Re e(\mathcal{M}_\gamma \mathcal{M}_{Z^0})_L}{2|\mathcal{M}_\gamma|^2} \simeq \frac{G_F Q^2}{4\sqrt{2}\pi\alpha} \end{aligned} \tag{3.4}$$

where G_F is the Fermi constant for muon decay and α is the electromagnetic coupling constant. A^{PV} then is on the order of 15 parts per million (ppm) for $Q^2 \sim 0.5\,(\mathrm{GeV}/c)^2$.

It has been only in this last decade that techniques and technologies have been developed to allow measurements of asymmetries to better than 1 ppm. In practice, the integrated yield (N_L, N_R) of the differential cross-section is measured, normalized by the beam current (I_L, I_R):

$$A_{\mathrm{raw}} = \frac{N_R/I_R - N_L/I_L}{N_R/I_R + N_L/I_L} \tag{3.5}$$

where *raw* denotes the value obtained from the raw data without corrections. With the high precision now attainable at electron accelerators and progress in formulating the contributions of radiative corrections to the electroweak processes, the study of weak neutral current interactions in elastic electron scattering provides access to a rich array of hadronic qualities.

3.1.1   History of Parity Violation in Electron Scattering

Measuring the parity-violating asymmetry, A^{PV} with polarized electron scattering was originally proposed by Zeldovich in 1957[58, 59]. Zeldovich predicted an asymmetry on the order of $10^{-4}Q^2$ assuming the effect was due to weak interactions. Investigations with this method were limited until progress in theory allowed calculation of radiative corrections and progress in experimental techniques and equipment allowed control of systematics. This combined progress enabled the measurement of the small asymmetry signal typical of low-Q^2 experiments.

3.1.1.1   Previous Experiments

SLAC

The first successful electron scattering asymmetry measurement was conducted at SLAC in 1978 where Prescott, *et al.*[60], using an unpolarized deuterium target and $Q^2 = 1.6(\mathrm{GeV}/c)^2$, convincingly demonstrated that the Z^0 violates parity, and that the Standard Model of electroweak unification was the correct theory from among a number of viable models at that time. In addition, this experiment determined the value for the electroweak mixing angle, $\sin^2\theta_W = 0.224 \pm 0.014$, a result which was competitive with the best measurements of $\sin^\theta_W$ then available. The SLAC E122 group pioneered the following experimental techniques for this measurement:

1. GaAs photo-cathode for the polarized electron source.

2. Rapid, random beam-helicity reversal.

3. Integration of electron flux rather than event by event counting.

4. Beam asymmetry sign reversals as a check on systematics.

Since this pioneering measurement, statistical and systematic precision achievable has greatly improved for low-Q^2 measurements. Two other experiments, described next, were planned and conducted as tests of the Standard Model.

Bates

To further investigate weak neutral currents, elastic scattering from carbon was used to measure the parity-violating asymmetry in the $^{12}\mathrm{C}(\vec{e}, e')$ reaction.[61, 62] This experiment measured the model-independent 'neutral current coupling' $\tilde{\gamma} = 0.14 \pm 0.03$

where $\tilde{\gamma} = \frac{2}{3}\frac{\sqrt{2}\pi\alpha}{G_F}\frac{A^{\mathrm{PV}}}{Q^2 P_e}$ and P_e is the percent polarization of the electron beam. This experiment also introduced additional techniques for limiting and controlling systematics: a high-current polarized beam reduced the statistical errors, a beam-current feed-back system reduced helicity-correlated intensity asymmetries and an on-line calibration of other systematic corrections provided reduction of false asymmetries from sources such as beam transport, detector drifts, target irregularities and so on.

Mainz

The parity violating asymmetry of neutral weak currents has contributions from vector and axial-vector components. In contrast to SLAC experiment E122, the Mainz experiment, Heil, *et al.*,[63], enhanced sensitivity to hadronic axial vector currents by measuring medium energy electrons scattered at backward angles.

In measuring 300 MeV electrons scattered from ^{9}Be at an average angle of $\vartheta = 130°$, the Mainz group calculated an asymmetry of

$$A_{ex}^{\mathrm{PV}} = (-9.4 \pm 1.8 \pm 0.5) \times 10^{-5}. \tag{3.6}$$

where the first error is statistical and the second error is systematic.

While similar to E122 in using integration to handle the high event rate, Heil, *et al.*, increased the A^{PV} sensitivity to 10^{-5}, a factor of 10 improvement from the SLAC experiment. This, in turn, led to increased sensitivity to systematic errors.

Heil, *et al.*, returned a model dependent interpretation of these data which yielded the Weinberg (electroweak mixing) angle of $\sin^2\theta_W = 0.221 \pm 0.014 \pm 0.004$.

SAMPLE

Conducted at the Bates Linear Accelerator, this experiment was the first to use parity violation to determine the weak neutral magnetic form factor of the proton [64, 65, 57]. The SAMPLE experiment uses the ^{1}H$(\vec{e}, e')$ reaction where 200 MeV electrons from a bulk GaAs photo-cathode, with typically 35% polarization, were scattered at backward angles into a Čerenkov detector. The SAMPLE asymmetry results were A$=-6.79 \pm 0.64 \pm 0.55$ ppm, where the first error is statistical and the second is systematic. The strange magnetic form factor derived from this asymmetry is[66]

$$G_M^s(Q^2 = 0.1(\mathrm{GeV/c})^2) = 0.14 \pm 0.29_{(\mathrm{stat})} \pm 0.31_{(\mathrm{sys})}. \tag{3.7}$$

The SAMPLE kinematics require determination of the axial vector form factor, $G_A^{(Z,p)}$, in order to reliably extract G_M^s. The SAMPLE experimental value for the axial vector form factor is

$$G_Z^e(T=1) = 0.22 \pm 0.45_{\text{(stat)}} \pm 0.39_{\text{(sys)}}. \tag{3.8}$$

There is yet considerable uncertainty in the calculation of the axial vector form factor[57]. A determination of $G_A^{(Z,p)}$ is difficult since this contribution is greatly suppressed and the radiative corrections associated with the nucleon axial vector coupling obscure the interpretation.

3.2   Electro-weak Interference
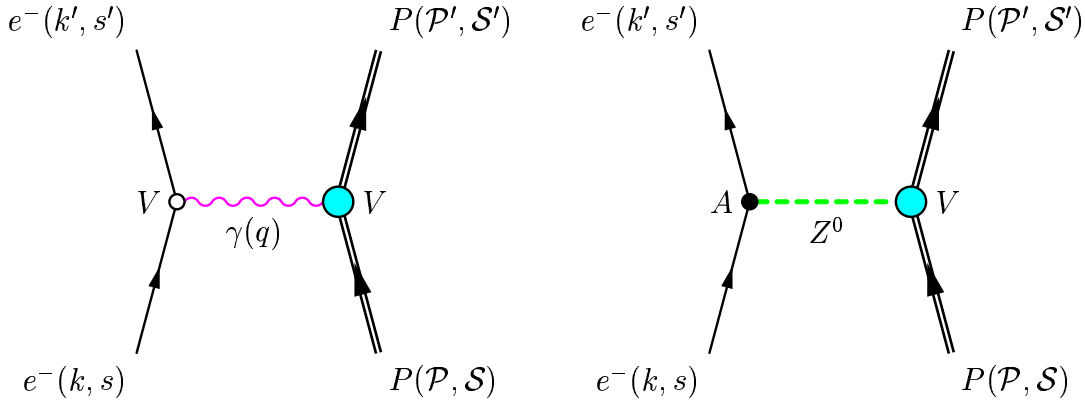
Figure 3.2: electromagnetic and Z^0 Bozon interaction

As discussed above, the theoretical parity-violating asymmetry can be derived from the electromagnetic and the weak neutral current scattering amplitudes; $\mathcal{M}_\gamma$ and $\mathcal{M}_{Z^0}$. The asymmetry is given in Eqn. 3.4 where we have neglected contributions from higher-order processes. The matrix elements can be derived by standard methods[67, 68].

The electromagnetic interaction is given by

$$\mathcal{M}_\gamma = (ie)^2 \langle e(k', s')| \hat{\jmath}^\mu_{EM} |e(k, s)\rangle \left(\frac{-ig_{\mu\nu}}{q^2}\right) \langle p(P', S')| \hat{\mathcal{J}}^\nu_{EM} |p(P, S)\rangle \qquad (3.9)$$

where $e(k', s')$, $e(k, s)$ - are the final and initial states of the electron,

$\quad\quad\quad$ $p(P', S')$, $p(P, S)$ - are the final and initial states of the proton,

$\quad\quad\quad$ $-ig_{\mu\nu}/q^2$ - is the photon propagator,

$\quad\quad\quad$ $\hat{\jmath}^\mu_{EM}$, $\hat{\mathcal{J}}^\nu_{EM}$ - are the electromagnetic current operators for the electron and proton, respectively; e is the charge of the electron,

$\quad\quad\quad$ k, (k'), P, (P') - refer to the electron's and proton's initial(final) momentum, respectively (see Fig. 3.2),

$\quad\quad\quad$ s, (s'), S, (S') - refer to the electron's and proton's initial(final) spin states, respectively.

Similarly, the matrix element for the Z^0 interaction is given by

$$\mathcal{M}_{Z^0} \simeq \left(\frac{-ig}{\cos\theta_W}\right)^2 \langle e(k', s')| \hat{\jmath}^\mu_Z |e(k, s)\rangle \left(\frac{-ig_{\mu\nu}}{M^2_Z + Q^2}\right) \langle p(P', S')| \hat{\mathcal{J}}^\nu_Z |p(P, S)\rangle, (3.10)$$

where g - is the electroweak coupling constant,

$\dfrac{-ig_{\mu\nu}}{M^2_Z + Q^2}$ - is the Z^0 propagator,

$\quad$ (The complete propagator, $\dfrac{-i(g_{\mu\nu} - \frac{q_\mu q_\nu}{M q^2})}{M^2_Z + Q^2}$ is $\simeq \dfrac{-ig_{\mu\nu}}{M^2_Z - q^2}$).

$\hat{\jmath}^\mu_Z$ - is the weak neutral current operator for the electron,

and $\hat{\mathcal{J}}^\nu_Z$ - is the weak neutral current operator for the proton.

The electroweak interaction term for the electron from Eqn. 3.10 can be expanded in terms of quark flavors and coupling constants as

$$\langle e(k', s')| \hat{\jmath}^\mu_Z |e(k, s)\rangle = \overline{u}(k', s') \frac{1}{2} \left(\gamma^\mu C^f_V - \gamma^\mu \gamma^5 C^f_A\right) u(k, s) \qquad (3.11)$$

where $\overline{u}(k', s')$, $u(k, s)$ - are the initial and final state spinors

$\quad\quad\quad$ C^f_V - is the weak vector coupling

$\quad\quad\quad$ C^f_A - is the weak axial vector coupling

$\quad\quad\quad$ and Q_f - is the fermion charge.

The couplings and charges are given in Table 3.1

Fermion flavor	Q_f	C_A^f	C_V^f
e	-1	$-\frac{1}{2}$	$-\frac{1}{2} + 2\sin^2\theta_W$
u, c, t	$\frac{2}{3}$	$\frac{1}{2}$	$\frac{1}{2} - \frac{4}{3}\sin^2\theta_W$
d, s, b	$-\frac{1}{3}$	$-\frac{1}{2}$	$-\frac{1}{2} + \frac{2}{3}\sin^2\theta_W$

Table 3.1: The $Z^0 \to f\bar{f}$ vertex factors for the electroweak quark couplings in the Standard Model[68].

Similarly the weak neutral current interaction for the proton can be expanded as

$$\langle p(P', S')|\, \hat{\mathcal{J}}_Z^\mu \,|p(P, S)\rangle = \overline{\mathcal{U}}(P', S')[\gamma^\mu F_1^{(Z,p)}(Q^2) + i\frac{\sigma^{\mu\nu}q_\nu}{2M_Z}F_2^{(Z,p)}(Q^2)$$
$$+\gamma^\mu\gamma^5 G_A^{(Z,p)}(Q^2) + \frac{q^\mu\gamma^5}{M_Z}G_P^{(Z,p)}(Q^2)]\,\mathcal{U}(P, S) \quad (3.12)$$

where $\mathcal{U}(P, S), \mathcal{U}(P', S')$ - are the proton spinors for the initial and final states.
$F_1^{(Z,p)}$, $F_2^{(Z,p)}$ - are the Dirac and Pauli Form factors, respectively.
$G_A^{(Z,p)}$ - is the axial-vector form factor.
and $G_p^{(Z,p)}$ - is the pseudoscalar form factor.

The pseudoscalar form factor, $G_p^{(Z,p)}$ vanishes when contracted on the electron tensor in the extreme relativistic limit (due to the electron's small mass) and will not be considered further [69]. Also, as all form factors are functions of Q^2, Q^2 dependence will be considered implicit and this notation will be dropped hence forward.

As in the case of the electromagnetic form factors, we prefer to use the Sachs form factors over the Dirac and Pauli form factors. These in turn will be related to the quark form factors $G_{E,M}^{(i)}$ (where $i = \{u, d, s, c, b, t\}$) from which we can extract $G_{E,M}^{(s)}$, or alternatively, for comparisons, calculate an asymmetry with a net zero strange contribution ($G_{E,M}^{(s)} = 0$).

3.2.1   Quark flavor currents

We will limit ourselves here to considering a basis consisting only of the light quark flavors (u,d,s), for the reasons discussed in section 2.1.

Writing the electromagnetic and Z^0 matrix elements for the proton interaction

in terms of the quark couplings we have

$$\langle p(P', S')|\hat{\mathcal{J}}^{\mu}_{EM}\, |p(P, S)\rangle = \langle p(P', S')|\sum_{i=u,d,s...} \bar{q}_i\, \gamma^{\mu} Q_i\, q_i\, |p(P, S)\rangle \tag{3.13}$$

$$\langle p(P', S')|\hat{\mathcal{J}}^{\mu}_{Z}\, |p(P, S)\rangle = \langle p(P', S')|\sum_{i=u,d,s...} \bar{q}_i\, \frac{1}{2}\left(\gamma^{\mu} C^i_V - \gamma^{\mu}\gamma^5 C^i_A\right) q_i\, |p(P, S)\rangle \tag{3.14}$$

where q, $\bar{q}$ are the quark initial and final states, respectively.

Eqn. 3.14 can be expanded into vector and axial-vector terms as

$$\langle p(P', S')|\hat{\mathcal{J}}^{\mu}_{Z}\, |p(P, S)\rangle = \langle p(P', S')|\sum_{i=u,d,s} \frac{1}{2}\bar{q}_i\gamma^{\mu} C^i_V q_i\, |p(P, S)\rangle$$
$$- \langle p(P', S')|\sum_{i=u,d,s} \frac{1}{2}\bar{q}_i\gamma^{\mu}\gamma^5 C^i_A q_i\, |p(P, S)\rangle\,. \tag{3.15}$$

Next we can define quark-vector and quark-axial-vector current operators as

$$\hat{j}^{\mu,i}_V = \bar{q}_i\, \gamma^{\mu} q_i\,, \quad \text{and} \quad \hat{j}^{\mu,i}_A = \bar{q}_i\, \gamma^{\mu}\gamma^5 q_i\,, \tag{3.16}$$

and rewrite Eqn 3.15 as

$$\langle p(P', S')|\hat{\mathcal{J}}^{\mu}_{Z}\, |p(P, S)\rangle =$$
$$\sum_{i=u,d,s} \frac{1}{2} C^i_V \langle p(P', S')|\hat{j}^{\mu,i}_V|p(P, S)\rangle - \sum_{i=u,d,s} \frac{1}{2} C^i_A \langle p(P', S')|\hat{j}^{\mu,i}_A|p(P, S)\rangle\,. \tag{3.17}$$

By separating Eqn. 3.12 into vector and axial-vector contributions and comparing this to Eqn. 3.17 we see that the Dirac, Pauli and axial form factors can be written in terms of the quark flavors and the proton spinors,

$$\langle p(P', S')|\hat{j}^{\mu,i}_V|p(P, S)\rangle = \overline{\mathcal{U}}(P', S')[\gamma^{\mu} F^{i(p)}_1 + i\frac{\sigma^{\mu\nu} q_\nu}{2M} F^{i(p)}_2]\mathcal{U}(P', S') \tag{3.18}$$

$$\text{and}$$

$$\langle p(P', S')|\hat{j}^{\mu,i}_A|p(P, S)\rangle = \overline{\mathcal{U}}(P', S')[\gamma^{\mu}\gamma^5 G^{i,(p)}_A]\mathcal{U}(P', S')\,. \tag{3.19}$$

Inserting 3.18 and 3.19 into 3.17 we arrive at the Z^0-proton matrix element in terms of the Dirac and Fermi form factors for the different quark flavors and the electroweak quark couplings from Table 3.1:

$$\langle p(P', S')|\hat{\mathcal{J}}^{\mu}_{Z}\, |p(P, S)\rangle = \sum_{i=u,d,s} \frac{1}{2} C^i_V \overline{\mathcal{U}}(P', S')[\gamma^{\mu} F^{i(p)}_1 + i\frac{\sigma^{\mu\nu} q_\nu}{2M} F^{i(p)}_2]\mathcal{U}(P', S')$$

$$- \sum_{i=u,d,s} \frac{1}{2} C^i_A \overline{\mathcal{U}}(P', S')[\gamma^{\mu}\gamma^5 G^{i(p)}_A]\mathcal{U}(P', S')\,. \tag{3.20}$$

The electromagnetic matrix element is similarly written in terms of the quark flavors.

$$\langle p(P', S') | \hat{\mathcal{J}}_{EM}^{\mu} | p(P, S) \rangle =$$
$$\sum_{i=u,d,s} \overline{\mathcal{U}}(P', S')[Q_i(\gamma^{\mu} F_1^{i(p)} + i\frac{\sigma^{\mu\nu} q_{\nu}}{2M} F_2^{i(p)})]\mathcal{U}(P', S') .$$

$$(3.21)$$

3.2.2   Neutral Weak Form Factors

It is useful to have the Sachs form factors for the γ-proton and Z^0-proton interactions in terms of the individual quark flavors. To do this we start with the Fermi and Dirac form factors for the γ-proton and Z^0-proton interactions written in term of the quark flavors

$$F_{1,2}^{(\gamma,p)} = \sum_{i=u,d,s} Q_i \, F_{1,2}^{i(p)} \tag{3.22}$$

$$F_{1,2}^{(Z,p)} = \sum_{i=u,d,s} \frac{1}{2} C_V^i \, F_{1,2}^{i(p)} \tag{3.23}$$

$$G_A^{(Z,p)} = \sum_{i=u,d,s} -\frac{1}{2} C_A^i \, G_{1,P}^{i(p)}. \tag{3.24}$$

These are converted to the Sachs form factors using 2.8;

$$G_E^{i(p)} = F_1^{i(p)} - \tau F_2^{i(p)} \tag{3.25}$$

$$G_M^{i(p)} = F_1^{i(p)} + F_2^{i(p)} , \tag{3.26}$$

which yields

$$G_{E,M}^{(\gamma,p)} = \sum_{i=u,d,s} Q_i \, G_{E,M}^{i(p)} \tag{3.27}$$

$$G_{E,M}^{(Z,p)} = \sum_{i=u,d,s} \frac{1}{2} C_V^i \, G_{E,M}^{i(p)}. \tag{3.28}$$

Similar steps yield the Sachs form factors for the neutron;

$$G_{E,M}^{(\gamma,n)} = \sum_{i=u,d,s} Q_i \, G_{E,M}^{i(n)} \tag{3.29}$$

$$G_{E,M}^{(Z,n)} = \sum_{i=u,d,s} \frac{1}{2} C_V^i \, G_{E,M}^{i(n)} \tag{3.30}$$

Expanding 3.28 we have

$$G_E^{(Z,p)} = \left(\frac{1}{4} - \frac{2}{3}\sin^2\Theta_W\right) G_E^u - \left(\frac{1}{4} - \frac{1}{3}\sin^2\Theta_W\right) \left(G_E^d + G_E^s\right) \qquad (3.31)$$

$$G_M^{(Z,p)} = \left(\frac{1}{4} - \frac{2}{3}\sin^2\Theta_W\right) G_M^u - \left(\frac{1}{4} - \frac{1}{3}\sin^2\Theta_W\right) \left(G_M^d + G_M^s\right) \qquad (3.32)$$

Invoking isospin symmetry, we replace the up quark in the proton with the down quark in the neutron and vice-versa, which allows us to eliminate the up and down quark contributions from the neutral weak form factors by using the proton and neutron electromagnetic form factors 3.28 and 3.30, and thus obtain

$$G_E^{(Z,p)} = \frac{1}{4}\left(G_E^{p\gamma} - G_E^{n\gamma}\right) - G_E^{p\gamma}\sin^2\Theta_W - \frac{1}{4}G_E^s \qquad (3.33)$$

$$G_M^{(Z,p)} = \frac{1}{4}\left(G_M^{p\gamma} - G_M^{n\gamma}\right) - G_M^{p\gamma}\sin^2\Theta_W - \frac{1}{4}G_M^s \qquad (3.34)$$

This is a key result. In shows how the neutral weak form factors are related to the electromagnetic form factors with a contribution from the strange (electric or magnetic) form factor[57].

Electroweak radiative corrections, which are due to the running of the coupling constants, are required in all the terms.

3.3   Asymmetry

Gathering all the terms back into Eqn.3.4 we arrive finally at the complete theoretical asymmetry[70]

$$A_{\text{th}} = \left[\frac{-G_F Q^2}{\pi\alpha\sqrt{2}}\right] \frac{\varepsilon G_E^{\gamma p} G_E^{(Z,p)} + \tau G_M^{\gamma p} G_M^{(Z,p)} - \frac{1}{2}(1 - 4\sin^2\theta_W)\varepsilon' G_M^{\gamma p} G_A^{(Z,p)}}{\varepsilon (G_E^{\gamma p})^2 + \tau (G_M^{\gamma p})^2}$$

$$(3.35)$$

where τ, ε, ε' are kinematic quantities

$$\left.\begin{array}{lll} \tau= & Q^2/4M_p^2 c^2 & \sim 0.136 \\ \varepsilon= & [1 + 2(1+\tau)\tan^2\theta/2]^{-1} & \sim 0.97 \\ \varepsilon'= & \sqrt{(1-\varepsilon^2)(\tau+\tau^2)} & \sim 0.109 \end{array}\right\} \begin{array}{l} \text{These values are only for the} \\ \text{HAPPEX kinematics.} \end{array} \qquad (3.36)$$

By substituting Eqns. 3.33 and 3.34 in the above, the theoretical asymmetry can be written as a linear combination of G_E^s and G_M^s where the first term is the value

of the asymmetry in the absence of strange quark contribution (i.e. $G^S_{E,M} = 0$):

$$\mathrm{A}^{\mathrm{PV}} = \mathrm{A}^{\mathrm{S}=0}_{\mathrm{th}} + kG^s_E + lG^s_M \left(+mG^s_A\right) \tag{3.37}$$

where k and l are calculable constants which depend on kinematics and the known electromagnetic form factors of the proton. The values of k and l are, respectively, 30 and 11.76. The strange axial-vector term, mG^s_A is expected to be small and goes to zero at forward scattering angles.

A difference between the experimentally measured asymmetry and theoretical asymmetry (in the absence of strange quarks) can be defined such that deviations from zero signal the presence of $s\bar{s}$ pairs, i.e.;

$$\delta\mathrm{A} \equiv \mathrm{A}_{\mathrm{exp}} - \mathrm{A}^{\mathrm{S}=0}_{\mathrm{th}} = kG^s_E + lG^s_M \tag{3.38}$$

A non-zero value of δA would signal that strange quarks contribute to the electromagnetic structure of the proton, and therefore that the "sea" has a significant role to play in the charge and current distributions of the nucleon.

3.3.1 G^0 Formalism

An convenient alternative set of form factors in which to cast the electroweak observables is

$$G^{\gamma p}_{E,M} = \frac{2}{3}G^u_{E,M} - \frac{1}{3}G^d_{E,M} - \frac{1}{3}G^s_{E,M}, \tag{3.39}$$

$$G^{\gamma n}_{E,M} = \frac{2}{3}G^d_{E,M} - \frac{1}{3}G^u_{E,M} - \frac{1}{3}G^s_{E,M}, \tag{3.40}$$

$$\text{and}$$

$$G^0_{E,M} = \frac{1}{3}(G^u_{E,M} + G^d_{E,M} + G^s_{E,M}). \tag{3.41}$$

where the first two equations assume isospin symmetry. $G^0_{E,M}$ are the flavor singlet electromagnetic form factors of the nucleon.

The theoretical asymmetry can then be written as [71, 72]

$$A_{\mathrm{th}} = -A_0 \tau \rho'_{eq} \left(2 - 4\hat{\kappa}'_{eq}\sin^2\theta_W - \frac{\varepsilon\eta_p}{\varepsilon\eta_p^2 + \tau\mu_p^2} \frac{G^0_E + \tau\mu_p G^0_M/(\varepsilon\eta_p)}{G^{\gamma p}_M/\mu_p} \right) - A_A \tag{3.42}$$

Where $\mu_p(\mu_n)$ $\simeq 2.79(-1.91)$ is the proton(neutron) magnetic moment in nuclear magnetons,

$\boldsymbol{\eta_p}$ is equal to $\frac{G_E^{\gamma p}(Q^2)}{G_M^{\gamma p}(Q^2)/\mu_p}$,

$A_{\rm A}$ is the contribution from the proton axial form factor [70], which is calculated to be small for our kinematics, (0.56 ± 0.23) ppm[71].

ρ'_{eq} and $\hat{\kappa}'_{eq}$ = 0.9879 and 1.0029 respectively and include the effects of electroweak radiative corrections, and

G^0 can not be accessed directly in electromagnetic scattering experiments and thus represents new information on nucleon dynamics that can be measured only by the weak neutral current amplitude[71]

If, in addition to $G_{E,M}^0$, the proton and neutron electromagnetic form factors $G_{E,M}^{\gamma p}$ and $G_{E,M}^{\gamma n}$ are known, the strange form factors may be determined from:

$$G_{E,M}^s = G_{E,M}^0 - G_{E,M}^{\gamma p} - G_{E,M}^{\gamma n} \tag{3.43}$$

It is also convenient to normalize the form factors to $G_M^{\gamma p}/\mu_p$ since they will then tend to vary less with τ. In this way, the quantities extracted are $G_E^s/(G_M^{\gamma p}/\mu_p) \to \tau\rho_s$ and $G_M^s/(G_M^{\gamma p}/\mu_p) \to \mu_s$ as $\tau \to 0$. Some models[49, 50, 52, 55] predict the radius parameter, ρ_s could be of the order of $\pm\,2$, and μ_s could be of the order -0.3.

If contributions from strange quarks are indeed on this scale, results from this experiment along with others in progress should be able to establish their presence as well as providing good discrimination between the different theories.

'Never worry about theory as long as the
machinery does what it's supposed to do.'

– R. A. Heinlein

Chapter 4

Experimental Setup

4.1 Overview

The design of the Hall A Proton Parity Experiment (HAPPEX) was motivated by
the need to measure an asymmetry of a few parts per million (ppm). The technique
used to measure the asymmetry is largely dominated by counting statistics but is also
sensitive to systematic errors. To make a 10 percent or better measurement requires
on the order of 10^{14} events, which can be accomplished with sufficient luminosity. In
addition, the small size of the asymmetry requires careful measurement and control
of systematic errors.

The criteria needed for accomplishing these goals will be discussed in detail later,
in summary they are enumerated here:

1. High-current polarized source

   A high-current beam of longitudinally-polarized electrons is needed. Beam
   position and beam-current asymmetries must be limited to specific levels. As
   the figure of merit for HAPPEX is proportional to $\vec{P}^2 I$, where P is longitudinal
   beam polarization and I is beam current, a large polarization therefore is
   critical for meeting the uncertainty limits required by the small asymmetry.

2. Electron Accelerator

   The accelerator system is required to provide the required beam energy and
   beam stability under helicity reversal. Stringent limits on systematic errors
   are required of the accelerator and related systems.

3. Beam Modulation System

   A means is needed of inducing and measuring small, controlled shifts in beam-position and beam-energy as a method of determining the beam-transport systematics for later corrections of the measured asymmetry.

4. Beam monitors

   Beam-current monitors and beam-position monitors are needed to measure the helicity-correlated systematics in current, position and energy.

5. Cryogenic target system

   A target of high proton density is needed. The target system must be able to maintain a stable target density while dissipating the heat-load deposited by the high-current and sometimes fluctuating electron beam.

6. Detector System

   The high current required for adequate statistics makes necessary a detector system which can spatially separate the signal (elastic scattering) from background (inelastic scattering) and measure the electron-flux by integration of event pairs of opposite helicity states while limiting contributions from background noise.

7. Data Acquisition System

   As the mechanisms involved in selecting the beam helicity can inherently induce position, energy and intensity difference between helicity states, the data acquisition system must be able to measure and record these values and provide a means of controlling the feedback used in minimizing these systematic effects which contribute to false asymmetries.

The HAPPEX experiment was conducted in experimental Hall A at the Thomas Jefferson National Accelerator Facility. This experimental facility, (a.k.a. Jefferson Lab) is comprised of a 5.5 GeV accelerator whose electron beam is directed into one of three complementary end-stations where the experiments are conducted.

HAPPEX ran in four periods. The first was a week-long 'dress rehearsal' run in December of 1997 to assess sensitivity and methods to control helicity-correlated systematic asymmetries. The dress rehearsal was conducted with kinematics chosen to limit the physics asymmetry while increasing the data rate. This increases

the weight of the instrumental asymmetries making systematic problems easier to determine. Success with the dress rehearsal was followed by three production runs. The first segment of data production running was conducted in the Spring 1998. Then, after a year of data analysis to look for systematic errors or other pathological experimental problems, two additional production runs were conducted in Spring 1999 and in Summer 1999. As discussed below, the beam polarization, energy, and current were different between the 1998 and 1999 runs making them largely different experiments which required new studies of systematic effects.

A total of $(86 + 81 + 12.6)$ Coulombs of beam were taken on target for each run period respectively, which in turn yielded 163 Coulombs (after cuts) of analyzable data.

4.2   Jefferson Lab

The Thomas Jefferson National Accelerator Facility is located in Newport News, VA. Jefferson Lab offers a complete infrastructure to explore a broad range of medium energy nuclear physics. Currently the Jefferson Lab accelerator supplies a very low noise, high-duty factor electron beam of up to 5.5 GeV. Future plans include energy upgrades to 12 GeV and eventually 24 GeV. Jefferson Lab also hosts a free electron laser facility and a center for applied research and technology.

4.3   Accelerator

At the heart of Jefferson lab operations is the re-circulating linear accelerator - see Fig. 4.1. The accelerator uses an oval racetrack scheme in which the acceleration system is located in the straight sections and the re-circulation systems are located at both ends of the racetrack. There is a focusing and steering system interspersed throughout the acceleration sections and the re-circulation arcs.

Electrons from the source (see section 4.3.1) are accelerated up to 45 MeV and injected into the first of the two linear acceleration sections. The linacs are built up as follows. The primary elements are the CEBAF-Cornell super-conducting radio-frequency cavities [73]. When the cavities are driven at 1497 MHz, each cavity provides an acceleration gradient in excess of 6 MeV/m. The cavities are assembled in groups of two, and inserted into a cryounit. The cryounits are combined 4 to a
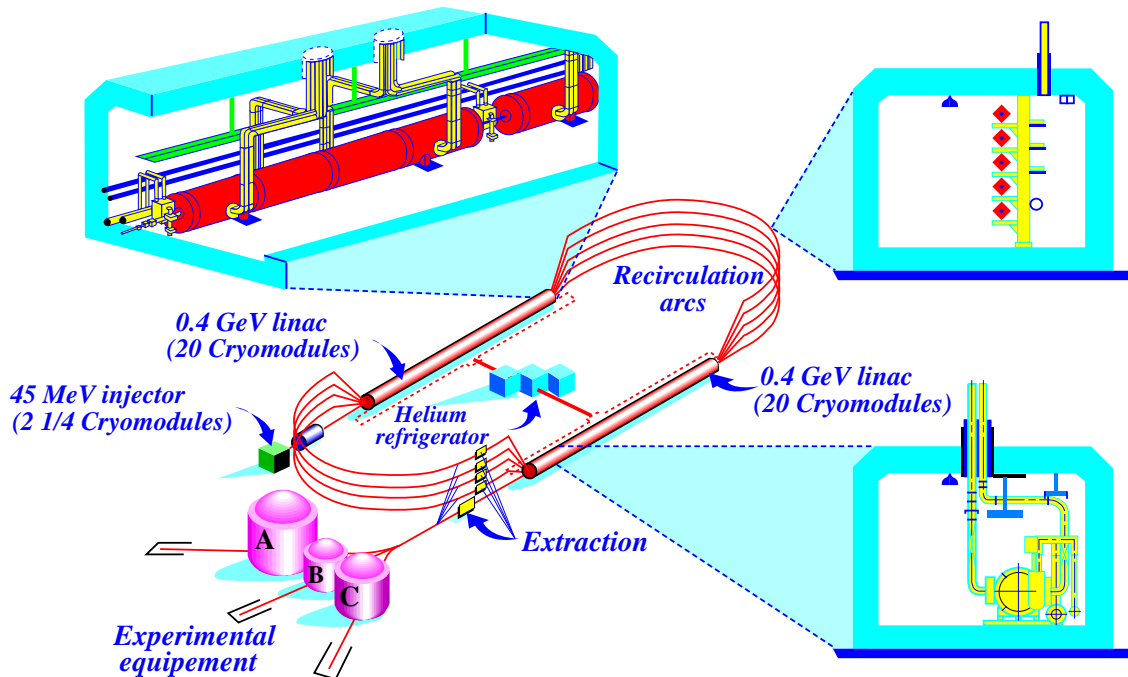
Figure 4.1: Jefferson Lab Configuration

cryomodule, with 20 cryomodules to a linac. Each linac can then provide in excess of 0.54 GeV beam energy. After bending 180° in the recirculation arcs, the beam is passed through the second linac for another boost. In total, the beam can make this trip 5 times, gaining over 1090 MeV per pass, plus the initial 45 MeV for a final delivered energy of 5500 MeV.

At the end of the second linac is the extraction point where all or part of the beam can be extracted to different halls via chromatic separation for different energies to each hall, or if two of the halls wish the same energy, an E-M 'kicker' running at 1497 MHz is used to nudge each pulse into a different trajectory for physical separation. By combining methods, different beam energies can be delivered to each hall to accommodate the different physics requirements of simultaneous experiments. In addition, the machine can be tuned to special energies less than 0.55 GeV per linac thus allowing a great range of delivered energies and a variety of beam polarization characteristics.

The power output of the accelerator can provide a total of 200 μA electron beam. In practice, the practical limits on the beam current provided come not from the accelerator but from the available cooling power delivered to the end-stations. The

Hall-A and Hall-C cryogenic targets can not be simultaneously cooled to match the equivalent beam heating of 200 μA. As circumstances require, one hall is scheduled to run at a slightly lowered current such that the combined total target heating will not exceed the limits of the cryogenic refrigerators. Work is in progress to increase the cooling power throughput to the end-stations thus increasing their current limits.

4.3.1   Polarized Source

The small asymmetry that HAPPEX endeavored to measure required that the polarized electron source meet two fundamental requirements. To provide high statistics, the source needed to provide a high current of highly polarized electrons. This intensity requirement created challenges for increasing the efficiency and lifetime of the source. In addition, HAPPEX required that the electron beam have little or no helicity-correlated differences in intensity, position or angle. The helicity correlation of these parameters are related, at some level, to the production technique of polarized electrons at the source. A growing number of different techniques exist for meeting these requirements[74][62].

The accelerator was designed to produced electron bunches at an initial frequency of 1497 MHz which, divided by three, allows each hall to receive a beam with a pulse train of 499 MHz. The system in use at Jefferson Lab to produce polarized electrons has the following components (see Fig. 4.2): the polarized light source for the control of the electron helicity, the photo-cathode for converting the polarized light into longitudinally-polarized electrons, a Wein filter for adjusting the electron's spin angle with respect to the precession angle of the accelerator, and the Mott Polarimeter for measuring the polarized electron ensembles of the beam. Creating polarized electrons for HAPPEX is essentially a five step process:

1. Left(right)-handed circularly polarized light is produced with laser and a Pockels cell and laser. This light is directed onto the surface of the GaAs crystal(see section 4.3.1.2).

2. A photon of this light is absorbed by a valence band electron which then is excited to the conduction band.

3. The electron diffuses to the crystal surface.

4. The electron escapes to the vacuum.
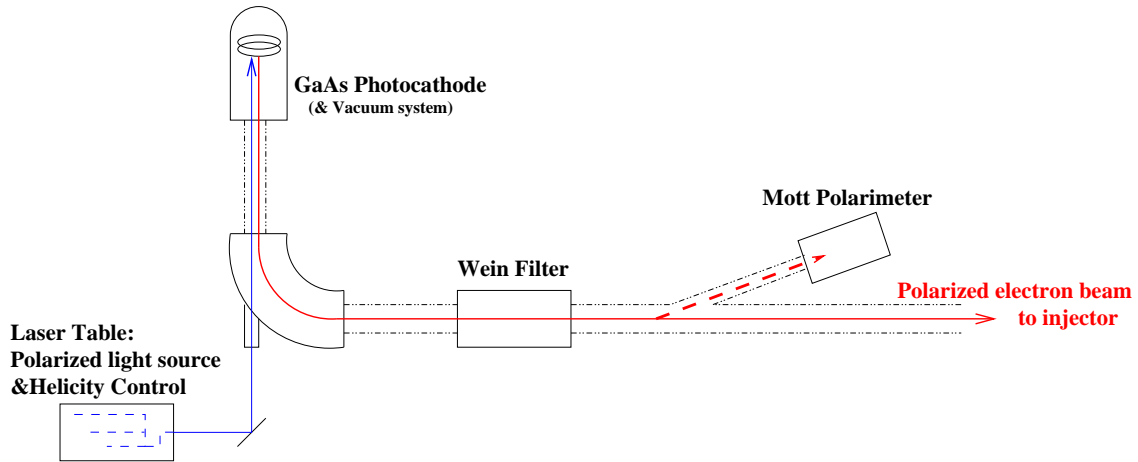
Figure 4.2: Schematic of polarized electron source.

5. The potential difference between the source and the injector draws the electron into the injector system, and from there into the accelerator.

4.3.1.1 Laser Subsystem

The laser system is composed of a gain-switched diode seed laser, a single pass diode optical amplifier, and a Pockels cell, along with various optical components mounted on an optical table, to deliver the laser beam to the photocathode [75]. The setup of the system is shown in Fig. 4.3.

Three lasers in the laser system (see Fig. 4.3), each running at 1497/3 MHz control the initial intensity of the electrons sent to the three end-stations. Light from the diode optical amplifier then passes through a shutter and an attenuator. The attenuator for each laser is a half-wave plate in combination with a linear polarizer and allows for the adjustment of light intensity on the photocathode. This provides the mechanism by which the polarized electron beam intensity to each experimental hall is controlled.

The lasers impinge upon the Gallium-Arsenide photocathode (GaAs) which emits polarized electrons. These are drawn away from the polarized source by a 120 keV potential and passed through a Wein filter, where their spin vector is rotated relative to their momentum vector. After additional acceleration to 5 MeV, the beam of electrons may be deflected into the Mott polarimeter or drawn into the injector for insertion into the accelerator.
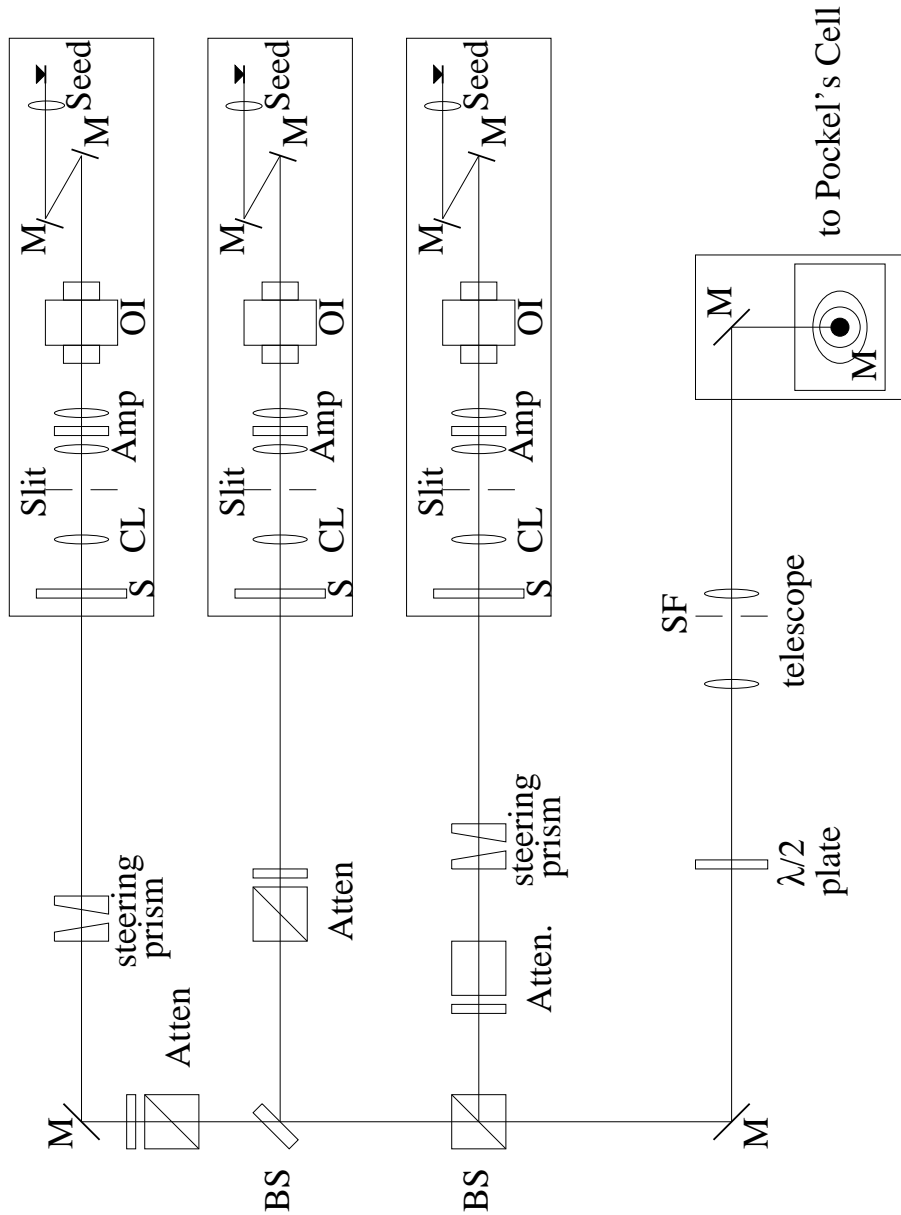
Figure 4.3: Laser table setup. The symbols in the figure are: Amp: laser amplifier, BS: Beam splitter, CL: Collimating lens, M: Mirror, OI: Optical isolator, S: Shutter.

An important test for the presence of false asymmetries is the insertion of a half-wave plate in the laser beam. This reverses the helicity of the laser light and hence the sign of the raw asymmetry while leaving many other possible systematic effects unchanged. This was performed remotely by inserting the plate between the attenuator and the Pockels cell. The half-wave plate rotates the incident linearly polarized laser light with respect to the Pockels cell's fast axis. The Pockels cell is the last optical component the polarized laser light encounters before passing into the vacuum chamber that houses the GaAs photocathode. The Pockels cell acts as a pulsed quarter wave retarder. Linearly polarized laser light incident on the Pockels cell emerges circularly polarized. For two signs of applied voltage, as determined by the helicity generator, we get two helicities of light and hence, the two helicities of the electron beam.

4.3.1.2   GaAs Crystal

GaAs is a direct band gap crystal. This means that the valence band maximum and the conduction band minimum occur at the Γ point in the Brillouin zone, where the momentum vector of the electron is zero. At the Γ point, the valence band has a P-like character and the conduction band has an S-like character. If the electrons are excited to the conduction band using circularly polarized light of positive(negative) helicity, the selection rule of $\delta m_j = +1(-1)$ applies. If the wavelength of the laser light is selected so that only transitions from the $P_{3/2}$ to the $S_{1/2}$ level are excited, one transition is three times more probable than the other. A schematic of the valence structure is shown in Fig. 4.3.1.2.

The polarization of an ensemble of electrons is defined as:

$$P = \frac{N_+ - N_-}{N_+ + N_-} \tag{4.1}$$

where $N_+(N_-)$ is the number of electrons with spin aligned parallel(anti-parallel) to the quantization axis. The polarization of the ensemble from the electrons arriving in the conduction band is then $P = (1-3)/(1+3) = -0.5$. Circularly polarized light of positive(negative) helicity results in a theoretical maximum of -50%(+50%) polarization of electrons in the conduction band. In practice, however, this maximum has not yet been attained. There are a number effects speculated to cause depolarization, such as electron-hole spin exchange in collisions as the electrons diffuse to the surface, and from spin exchange with the cesium atoms at the surface [76].
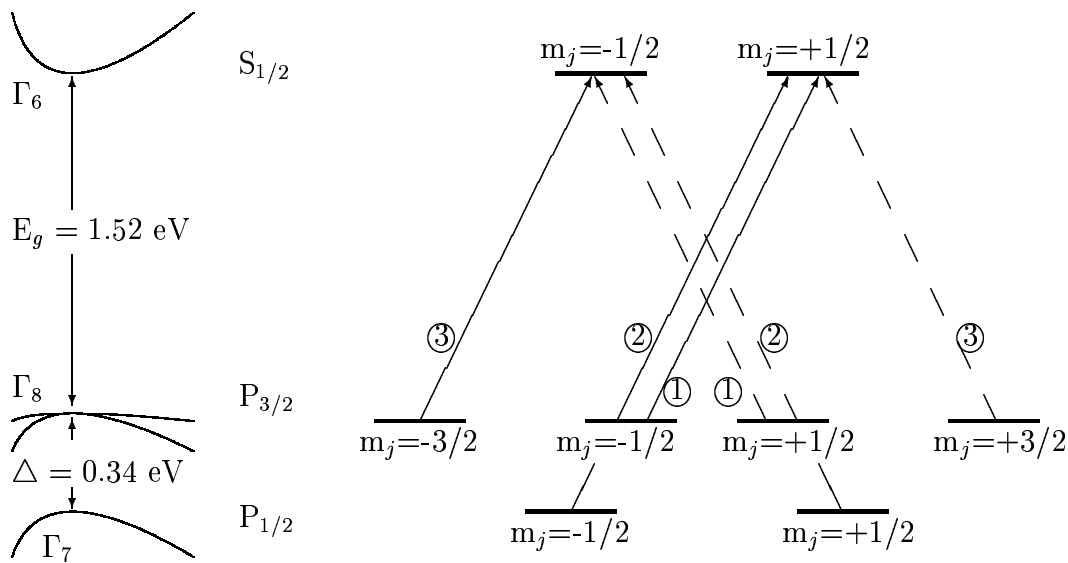
Figure 4.4: At left is shown the Gallium Arsenide bandgap structure in the vicinity of the Γ point. At right is a schematic of the magnetic substrates of the valence and conduction band with their relative transition probabilities. The allowed transitions for right(left) circularly polarized light are shown by the solid(dashed) lines.

The 1998 run used a 'bulk' crystal with the theoretical polarization described above. Its actual performance was $\simeq 37\%$. The 1999 runs used a 'strained' GaAs crystal which gives better control over the selection rules by separating slightly the $P_{3/2}$ levels. A laser wavelength is then selected to give 100% probability of a particular transition. In turn, this increases the theoretical polarization to 100% while the actual polarization reached was $\simeq 70\%$.

The needed currents on the order of 100 μAmps required both types of crystals to be coated with Cesium-Fluoride (CsF) by vapor-deposition. CsF increases the quantum efficiency of the cathode by reducing the work-function of the GaAs. The CsF however degrades over time and thus the GaAs crystal requires periodic re-cesiation. In addition, the vacuum around the GaAs crystal, while ultra-high, is not perfect. The resulting residual gases contaminate the crystal surface and lower the efficiency. These also are removed periodically by performing a 'bakeout' where the temperature in the GaAs housing is raised until the contaminating molecules are encouraged to evaporate. Afterwords the crystal is again re-cesiated.

4.3.1.3 Feedback system

Because the physics measurement is of the helicity-correlated cross section asymmetry, it is of critical importance to remove as many of the helicity-correlated sys-

tematic responses as possible. The sources for these helicity-correlated systematics can enter into the measurement electronics a number of ways depending upon the scheme used to choose the beam-helicity.

The helicity of the electron beam was set by passing the laser beam through the Pockels cell, and selecting with high voltage the left- or right-handed polarization of the cell. This in turn created left or right-handed polarized laser light which then transferred polarization to the electrons emitted from the GaAs crystal surface. A number of techniques were used to limit the polarization-induced systematic asymmetries. Collectively, these are called Polarization Induced Transport Asymmetry (PITA) effects. One of the largest systematic effects is due to beam current asymmetries. If the detectors and current monitors were truly linear devices we could normalize the detector signal before computing the physics asymmetry. We cannot, however, assume these devices are perfectly linear. To do so would introduce a false asymmetry at the ppm level. In order to reduce beam current asymmetries, a feedback system using the Pockels cell voltage was adopted. A schematic of the feedback system is shown in figure 4.5

One example of how these PITA effects can introduce false asymmetries into the physics measurement is based on the fact that the GaAs surface of the cathode varies in quantum efficiency (QE) across its surface. If the polarization selection by the Pockels cell deflects the laser beam slightly, the beam can illuminate areas of the cathode with differing QE. This in turn would yield a markedly different number of electrons for one polarization than for the other. This difference in number of electrons translates as a beam intensity difference, which is seen as a helicity-correlated event rate difference at the target which, in turn, appears as a helicity-correlated difference in the integrated signal at the detectors. To control the PITA effects, helicity pulse-pairs were measured by current and position monitors in the injector. Special measurements were done where the Pockels cell was driven from one helicity to another over a range of voltage offsets. The offset voltage was computer controlled with a Digital to Analog Converter (DAC). The settings of the DAC were chosen to have a linear relationship with the offset voltage. The dependence of the apparent asymmetry was measured and then plotted against the DAC value. A typical PITA slope is shown in Fig. 4.6.

The relationship between the PITA and the DAC setting was linear, and the slope attained from a fit to the data gives the DAC setting corresponding to a zero
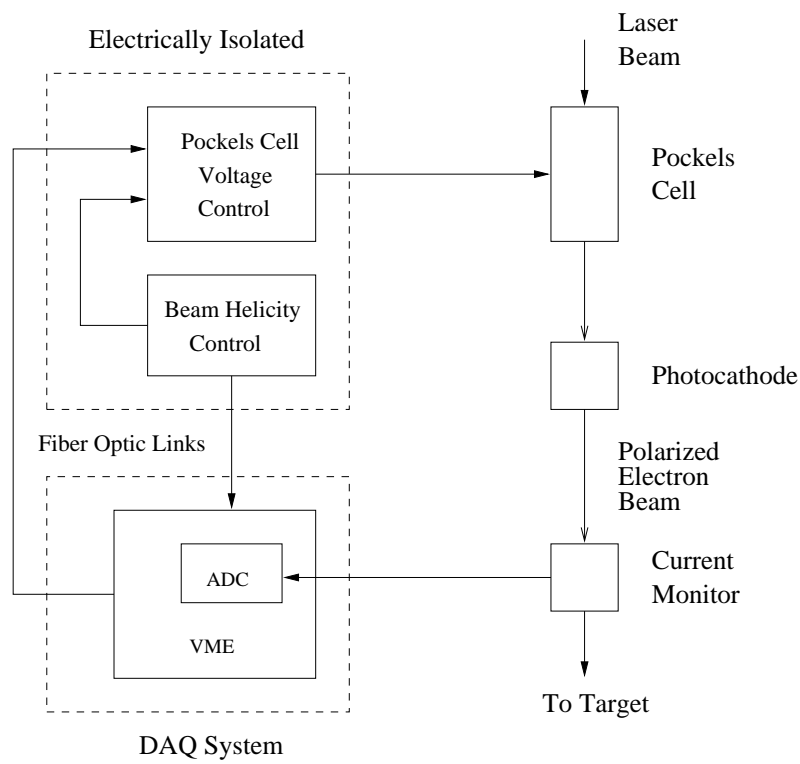
Figure 4.5: Beam current feedback system. The beam current is analyzed by the DAQ system and fed back into the Pockels cell control to minimize beam current asymmetries.

asymmetry. The DAC was then adjusted by the computer so as to minimize the asymmetry.

Measuring the PITA slope with respect to the DAC setting was routine and this was done periodically and following any change in the accelerator configuration, beam tune, or changes of the source. The PITA 'slope' was stable and, once computed, it was used by the HAPPEX Data Acquisition (HAPPEX DAQ) software to minimize the PITA during each mini-run (roughly every 10 minutes).
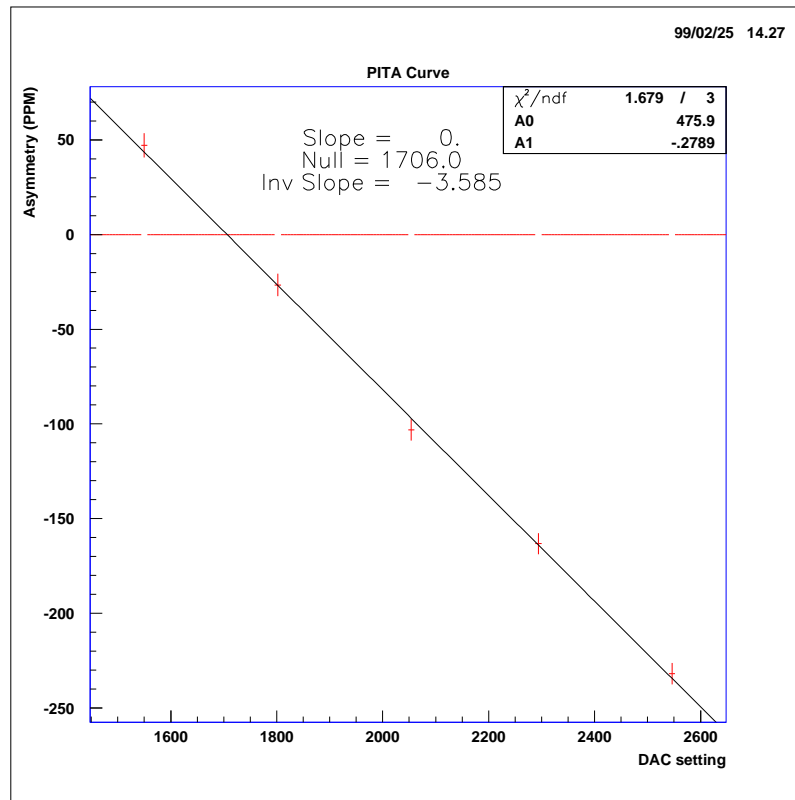
Figure 4.6: A typical PITA curve of beam current asymmetry plotted against the Pockels cell voltage DAC setting. A voltage offset was chosen to minimize the asymmetry.

4.3.1.4 Helicity Control

To avoid systematic problems associated with slowly varying calibration drifts in the electronics, the asymmetry measurements were conducted with back to back pulse-pairs. A helicity-flipping frequency for these pulse pairs was chosen to be of a much shorter time scale than any likely systematic-drift time.

Another consideration is the ubiquitous 60 Hz line noise picked up by the electronics which can induce systematic asymmetries. To avoid this, the helicity-flipping scheme and frequency must be chosen so there is no cyclic pattern of 60 Hz. To this end, sub-harmonic frequencies of 60 Hz, namely 15 Hz and 30 Hz were chosen as the structure for the helicity frequency.

The *helicity* pulse-pair signal (Fig. 4.8) is generated by the Helicity Request Generator, as shown in Fig. 4.7. First, a 30 Hz trigger is generated. This trigger is phase-locked to the 60 Hz power line. Second, a *15 Hz pair-sync* signal toggles at each rising edge of the 30 Hz trigger. This divides the 30 Hz windows into pairs. Third, a 24-bit shift register with feedback taps on bits 17,22,23 and 24 generates a pseudo-random number. This pseudo-random number repeats after 8^{24} cycles.

This *pseudo-random* number signal is taken as an 'exclusive-or' with the 15 Hz signal to create the *helicity* signal. This determines whether the pulse-pair has a (+,-) or (-,+) helicity sequence. The *helicity* signal is then sent only to the high voltage switcher for the Pockels cell because we want the real-time helicity of the beam known only at the source. At some point however, the helicity signal must be recorded into the data stream to correlate beam-helicity with cross-section asymmetry measurements. For this, the *helicity* signal is delayed by 8 bits or 4 pulse-pairs. Called the *delayed helicity data* signal, this ensures that the *delayed helicity data* signal entering the electronics of the DAQ is out of phase with the *helicity* signal sent to the Pockels cell. Further, the pseudo-random number and the delay ensures that the correlation is truly random for all practical purposes. The Helicity Request Generator is located in the injector. All signals brought to the HAPPEX DAQ in the counting house from the source are carried by fiber-optic cable to avoid ground-loop coupling of electronics with helicity signals. As yet another systematic control, a $\frac{1}{2}\lambda$ plate was periodically inserted and removed from the laser path. This introduced a non-electronic polarization reversal independent of any other device. Thus if the Pockels cell and all monitoring devices were working properly, the $\frac{1}{2}\lambda$ plate would effectively reverse the sign of the polarization and asymmetry with no possible change in other parts of the system.

30 Hz Trigger:

15 Hz Pair-Sync:

Random Bit:

Helicity:

Delayed Helicity:
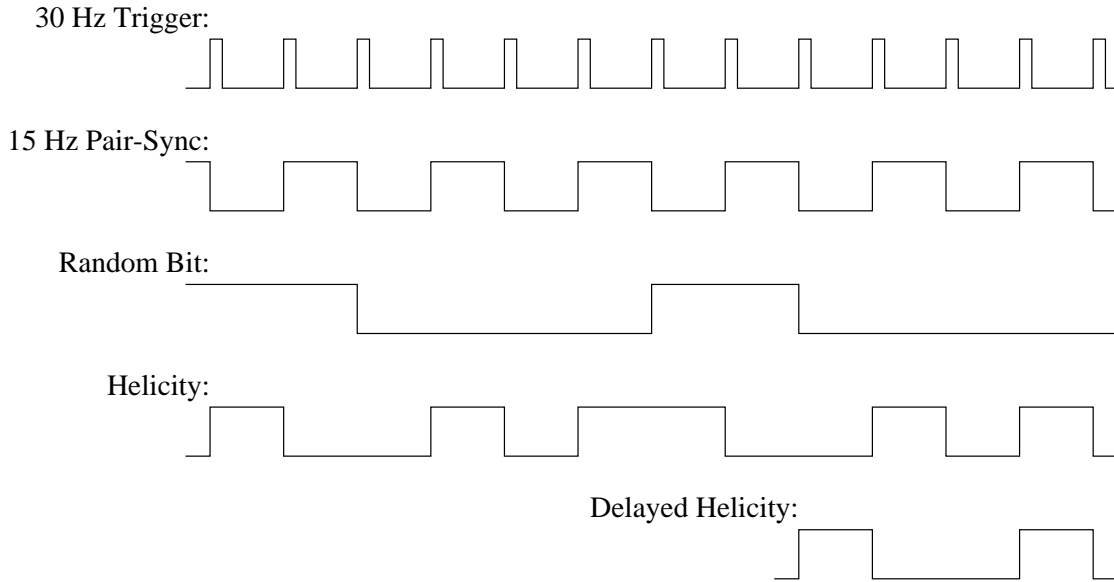
Figure 4.7: Timing diagram of Helicity Request Generator.

4.3.1.5 Spin Precession

The polarization of the electron ensemble from the source is either aligned or anti-aligned with the electron's momentum vector. While the polarized electron beam is transported through the accelerator arcs, the electron's spin precesses relative to its momentum vector due to Thomas precession. To have the electrons arrive on target with their spins properly aligned or anti-aligned with their momentum, it is required to adjust the electron's spin orientation at the source. This is done with a Wein filter.

The Wein filter maintains constant electric and magnetic fields mutually perpendicular to each other and the electron beam, as shown in Fig.4.9. The $\vec{E}$ and $\vec{B}$ field strengths are adjusted such that the electrons passing through the filter experience zero net force while rotating the polarization vector of the passing electrons.

4.4 Polarimetry

Beam polarization was measured by Mott polarimetry and by Møller polarimetry during the course of the 1998 HAPPEX runs. The results were compared with each other for consistency checks. In 1999 the Compton polarimeter was on line and used as a relative polarization measurement after first establishing the absolute
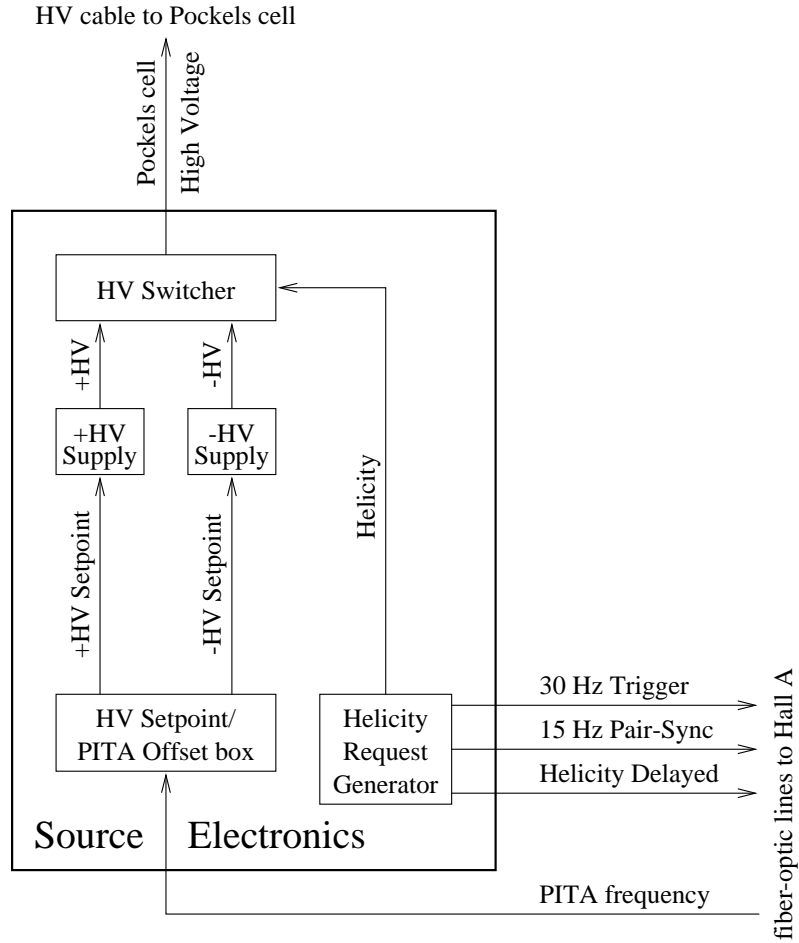
Figure 4.8: Schematic of Injector DAQ

polarization with the Mott or Møller polarimeter. Results from the Compton were compared against the Møller and Mott results.

4.4.1   Mott Polarimeter

The physical basis of Mott scattering can be understood by considering how high energy electrons are scattered by a bare nucleus of charge Ze. The motion of the electrons in the electric field $\mathbf{E}$ of the nucleus results in a magnetic field $\mathbf{B}$ in the electron's rest frame:

$$\mathbf{B} = -\frac{1}{c}\mathbf{v} \times \mathbf{E}. \tag{4.2}$$

The electric field due to the nucleus is $\mathbf{E} = (Ze/r^3)\mathbf{r}$, where $\mathbf{r}$ is the nucleus-electron separation. $\mathbf{B}$ can then be written as:
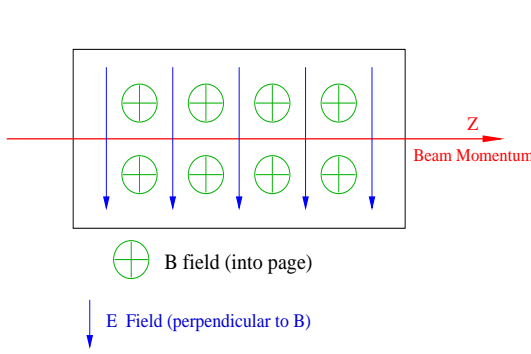
Figure 4.9: Wein Filter Schematic.
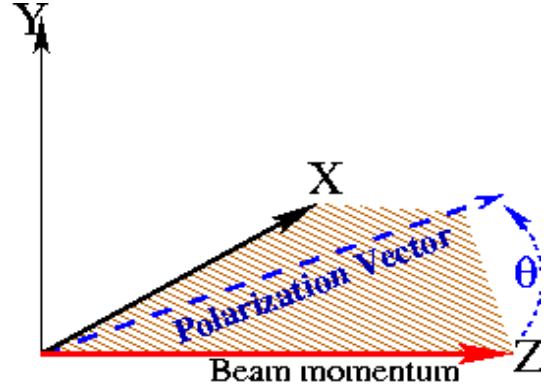
Figure 4.10: Beam line transport coordinates.

$$\mathbf{B} = \frac{Ze}{cr^3}\mathbf{r} \times \mathbf{v} = \frac{Ze}{mcr^3}\mathbf{L}. \tag{4.3}$$

where $\mathbf{L}$ is the orbital angular momentum of the electron and m is the electron's mass. The interaction of the magnetic field with the electron spin magnetic moment $\mu_{\mathbf{s}}$ introduces an interaction term $V_{so} = -\mu_{\mathbf{s}} \cdot \mathbf{B}$ in the scattering potential. The spin-orbit term can then be written as

$$V_{so} = \frac{Ze^2}{2m^2c^2r^3}\vec{\mathbf{L}} \cdot \vec{\mathbf{S}}. \tag{4.4}$$

The presence of the spin-orbit term in the scattering potential introduces a spin dependence in the scattering cross section $\sigma(\theta)$ which can be written as

$$\sigma(\theta,\phi) = I(\theta)\left[1 + S(\theta)\vec{P} \cdot \hat{n}\right] \tag{4.5}$$

where $S(\theta)$ is the asymmetry function, otherwise know as the Sherman function; this is the measure of the spin sensitivity of the polarimeter. $I(\theta)$ is the spin-averaged scattered intensity

$$I(\theta) = \frac{Z^2e^4}{4m^2\beta^4c^4\sin^4(\theta/2)}\left[1 - \beta^2\sin^2(\theta/2)\right](1 - \beta^2) \tag{4.6}$$

and $\vec{P}$ is the incident electron polarization. The unit vector $\hat{n}$ is normal to the scattering plane defined by

$$\hat{n} = \frac{\vec{k} \times \vec{k'}}{|\vec{k} \times \vec{k'}|} \tag{4.7}$$

where $(\vec{k})$ and $(\vec{k}')$ are the electron's momentum before and after scattering, respectively. The direction of $\hat{\mathbf{n}}$ is parallel to $\mathbf{L}$, and depends on whether scattering to the left or right is being considered.
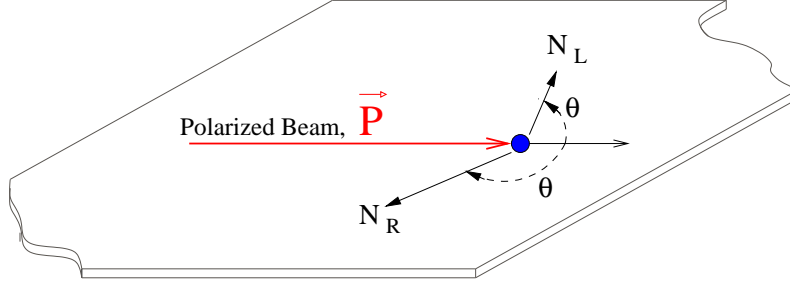
Figure 4.11: Mott scattering for electron polarimetry.

As shown in Fig. 4.11, a polarized ensemble of electrons interacts with the bare nucleus of the target foil. The ensemble will have a net polarization as given in Eqn. 4.1.

We can define a scattering asymmetry as:

$$A(\theta) = \frac{N_L - N_R}{N_L + N_R}. \tag{4.8}$$

Here, N_L and N_R are the number of electrons scattered to the left and right respectively through the angle θ. N_L is proportional to $N_+ \left[1 + S(\theta)\right] + N_- \left[1 - S(\theta)\right]$, and N_R is proportional to $N_+ \left[1 - S(\theta)\right] + N_- \left[1 + S(\theta)\right]$. Substituting this into Eqn.4.8 gives

$$\begin{aligned} A(\theta) &= \frac{N_L - N_R}{N_L + N_R} \\ &= \frac{N_+ \left[1 + S(\theta)\right] + N_- \left[1 - S(\theta)\right] - N_+ \left[1 - S(\theta)\right] + N_- \left[1 + S(\theta)\right]}{N_+ \left[1 + S(\theta)\right] + N_- \left[1 - S(\theta)\right] + N_+ \left[1 - S(\theta)\right] + N_- \left[1 + S(\theta)\right]} \\ &= \frac{(N_+ - N_-) \left[1 + S(\theta)\right] - (N_+ - N_-) \left[1 - S(\theta)\right]}{(N_+ + N_-) \left[1 + S(\theta)\right] + (N_+ + N_-) \left[1 - S(\theta)\right]} \\ &= \frac{(N_+ - N_-)}{(N_+ + N_-)} \frac{2S(\theta)}{2} \end{aligned} \tag{4.9}$$

$$\tag{4.10}$$

$$A(\theta) = \vec{P} S(\theta) \tag{4.11}$$

Knowledge of $S(\theta)$ and measuring the scattering asymmetry then allows a determination of the beam polarization:

$$\vec{P} = \frac{A(\theta)}{S(\theta)}. \tag{4.12}$$

$S(\theta)$ characterizes both the polarizing and analyzing power of Mott scattering. This function has been evaluated for many high Z materials including Au foils such as those used in the JLab Mott polarimeter.

A schematic of JLab's 5 MeV Mott polarimeter is shown in Figure 4.12. This instrument consists of several target foils on a target ladder, a linear feed-through to move the target ladder, 1 cm thick copper baffles, four detectors mounted symmetrically about the beam line, and an ion pump to control the local vacuum. A gold target foil of 0.1 μm was used for the Mott polarization measurements. Each copper plate has four holes to provide line of sight view to the target foil. These plates reduce inelastically scattered electrons and hence, background noise in the detectors. Four NE102a plastic scintillator detectors are placed at 173° to the beamline. This configuration allows simultaneous measurement of the two components of polarization transverse to the beam momentum direction. Not shown is a set of dipole magnets (called 'the dog-leg') which bend the electron beam in 'Z' path before the Mott polarimeter. This rotates the electrons spin from longitudinal to transverse polarization as required for the Mott interaction.

A series of polarization measurements were taken using this instrument during the Spring 1998 and Summer 1999 HAPPEX runs to determine the electron beam polarization near the source.

A number of systematic effects can arise in the Mott polarimeter including unequal detector responses, misalignment of the apparatus, corrections for finite target foil thickness, etc. A table of errors is given in Table 4.1.

Source of Error	$\frac{\Delta P_e}{P_e}(\%)$
Foil Thickness Extrapolation	5
Background Subtraction	3
Variation of P_e with Intensity	3
Theoretical Analyzing Power	1
Position of Beam	1
Statistics, Time Dependence	2
Misalignment of Spin Direction	1
Total Error	7

Table 4.1: Error budget for the Mott polarimeter.
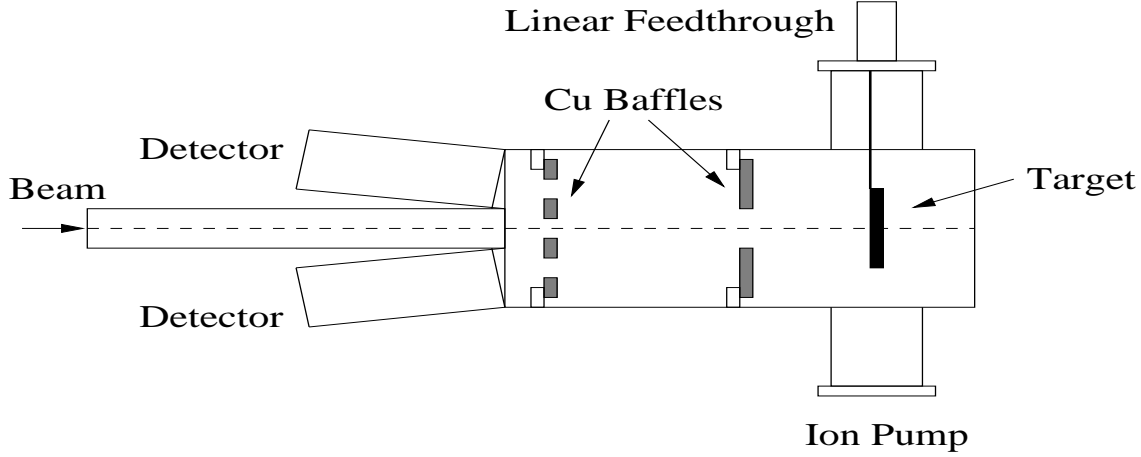
Figure 4.12: Schematic of Mott apparatus. Only two of the four detectors are shown in this figure. The other two detectors are mounted symmetrically to the beam on a plane extending out of the page.

4.4.2   Møller Polarimeter

In the extreme relativistic limit, the cross section for polarized e^-e^- scattering in the center-of-mass frame is given by[77]:

$$\frac{d\sigma}{d\Omega} = \frac{\alpha^2}{s} \frac{(3 + \cos^2\theta)^2}{\sin^4\theta} \{1 + P_z^B P_z^T A_{zz}(\theta)\} \tag{4.13}$$

for a longitudinally-polarized beam and target. A_{zz} is given by

$$A_{zz} = -\frac{(7 + \cos^2\theta)\sin^2\theta}{(2 + \cos^2\theta)^2} \tag{4.14}$$

and S is the CM energy squared, θ is the scattering angle in the CM frame, P_z^B and P_z^T are the beam and target foil longitudinal polarizations, respectively. An asymmetry for the cross section difference between right- and left-handed incident electrons can be calculated as

$$A_{M\text{øller}} = \frac{\left(\frac{d\sigma}{d\Omega}\right)_{\uparrow\uparrow} - \left(\frac{d\sigma}{d\Omega}\right)_{\uparrow\downarrow}}{\left(\frac{d\sigma}{d\Omega}\right)_{\uparrow\uparrow} + \left(\frac{d\sigma}{d\Omega}\right)_{\uparrow\downarrow}} = P_z^B P_z^T A_{zz}(\theta). \tag{4.15}$$

Independent knowledge of the target foil polarization P_z^T then allows a determination of the beam polarization [78]. This is the principle used by the Hall A Møller polarimeter[79].

A schematic of the Møller polarimeter is shown in Fig. 4.13. It consists of a target
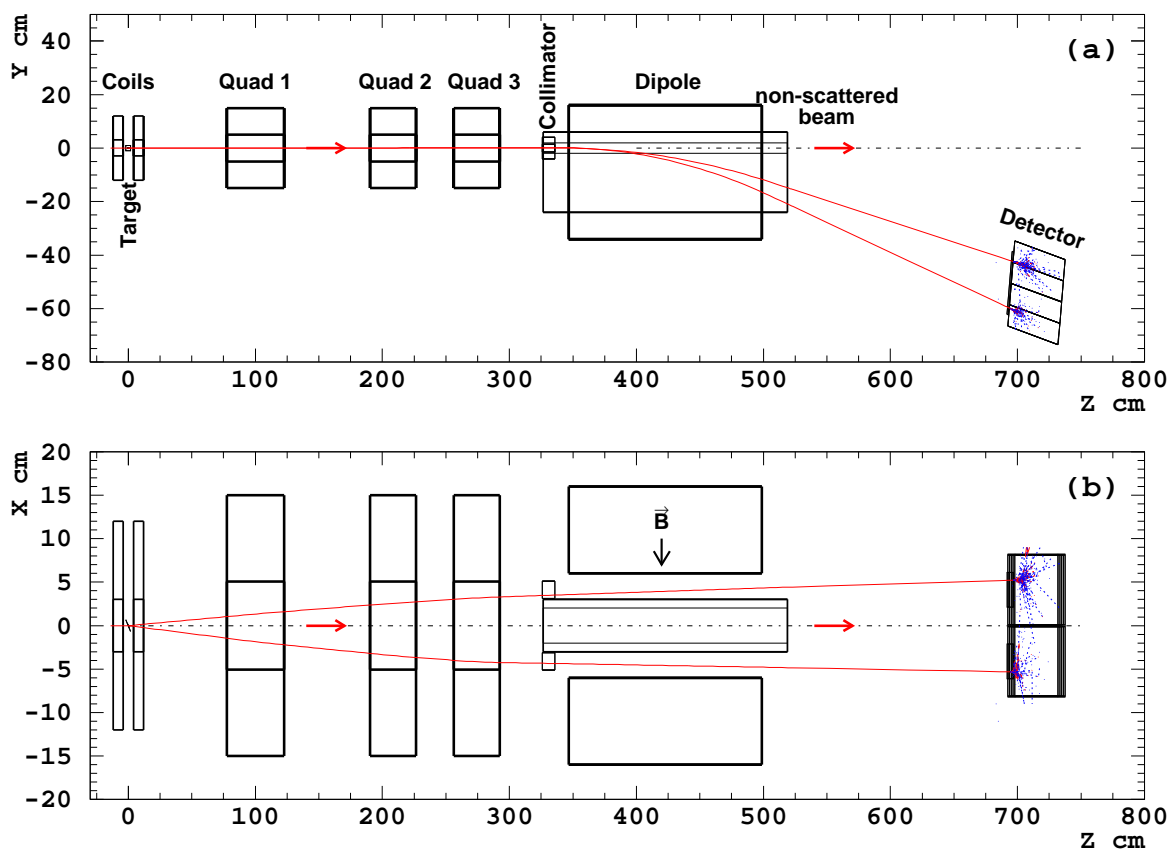
Figure 4.13: Schematic of Møller apparatus.

chamber, three quadrupole magnets, a dipole magnet, and a pair of detectors. The target chamber houses a drive mechanism containing a Supermendur[1] foil target[80] whose angle can be rotated with respect to the beam. A pair of Helmholtz coils on either side of the target chamber induce a magnetic field parallel or anti-parallel to the incident beam momentum.

When the Supermendur foil is placed in a magnetic field, a known fraction of the atomic electrons in the foil will have their spins aligned with the field at saturation. Boundary conditions constrain the field near the foil to be along the plane of the foil. The electron spins then align themselves parallel to the plane of the foil. With the foil oriented at approximately 20° with respect to the incident beam, the scattering angle, θ_{CM} is $\approx$ 90° where the Møller's longitudinal analyzing power is at its maximum; $A_{zzmax} = 7/9$. Transverse beam polarization also leads to an asymmetry, though the analyzing power is lower, about $\frac{1}{7}$ that of the longitudinal.

With information about the target polarization and the analyzing power one can extract the beam polarization by measuring the asymmetry

$$P_z^B = \frac{P_z^T A_{zz}(\theta_{CM})}{A_{M\o ller}} \tag{4.16}$$

As with any physical measurement, the Møller suffers from statistical and systematic errors. A list of these errors is given in Table 4.2.

Source of Error	$\frac{\Delta P_e}{P_e}(\%)$
P_{Target}	3.0%
Target Angle	0.5%
Analyzing power	0.3%
Transverse polarization	0.3%
Non-polarized backgrounds	<1.0%
Dead Time	1.0%
Observed fluctuations	1.0%
Total Error	3.4%

Table 4.2: Error budget of Møller polarimeter

---

[1]The Supermendur target is a Fe-Co alloy composed of 49% Fe, 49% Co, and 2% Va by mass. It can be magnetized to saturation in a relatively small magnetic field of $\sim$ 100g or so.

4.4.3   Compton Polarimeter

The down side to the polarization measurements of the Mott or Møller techniques is that these require a solid target placed in the beam path. After interacting with these targets, the beam is misdefined in terms of polarization, momentum and position. The beam is, therefore, unusable for production data of the physics experiment. The Mott is further limited because of its location near the injector and thus can not empirically measure effects of spin precession. The Møller technique is limited to a beam current of less than 10μAmps. Ideally, polarization measurements should be done in a way which is non-invasive, near the physics experiment, over a broad range of beam currents. Also it should achieve high statistical accuracy in a short period. This can be accomplished using with Compton polarimetry.

The Compton technique exploits the QED interaction where the cross section of the polarized electrons scattering off polarized photons is a function of their energies and scattering angle. The counting rate asymmetry is then directly proportional to the cross section asymmetry and the laser and electron beam polarizations. Both the scattered photons and the scattered electrons are measured and characterized per their energy and polarization. The beam polarization is extracted from Eqn. 4.17 by measuring the current normalized rates for the beam helicity states.

$$A_{exp}^{\text{Compton}} = \frac{N^+ - N^-}{N^+ + N^-} = P_e P_\gamma A_l. \tag{4.17}$$

Where P_e is the electron polarization, P_γ is the photon polarization, and A_l is the calculated cross section asymmetry. A schematic of this process is shown in Fig. 4.14 The error budget for the Compton polarimeter is given in table 4.3.

Source of Error	Systematic	Statistical
P_γ	1.1%	
A_{exp}	1.4%	1.4%
$\langle A_l \rangle$	2.4%	
Total Syst./stat.	3.0%	1.4%
Combined Error	3.3%	

Table 4.3: Error budget for the Compton polarimeter[81].

The compton technique is non-invasive in that the electrons sampled from the polarization ensemble are removed from the beam leaving the unperturbed electrons
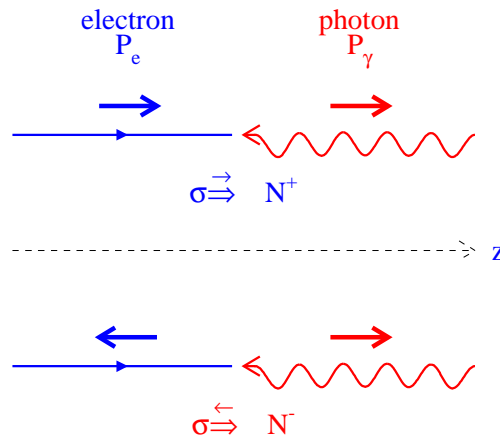
Figure 4.14: Compton asymmetry

to continue to the physics experiment.

The kinematics of compton scattering produce very small angles: For the $E_o = 4$ GeV JLab beam, the angles are typically less than $150\,\mu$rad and $10\,\mu$rad for the photon and electron, respectively. A kinematic depiction is shown in Fig. 4.15 To
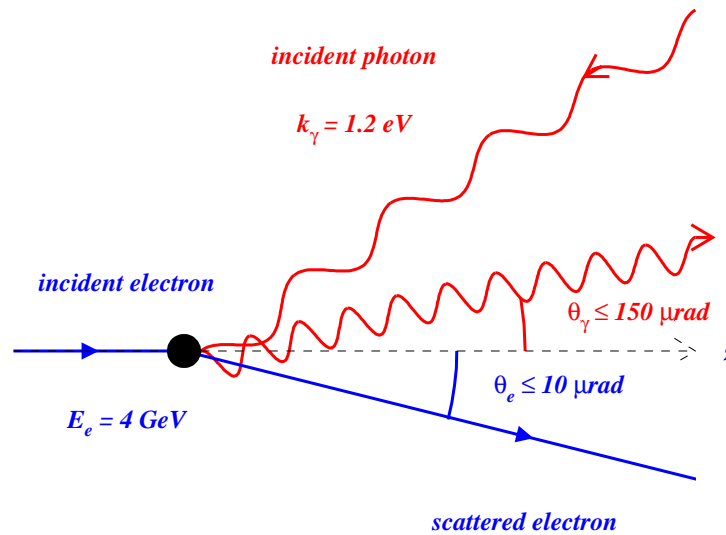
Figure 4.15: Kinematics of the Compton effect. A 4 Gev incident electron interacts with a 1.2 eV photon.

extract the scattered photons and electrons from the Compton polarimeter, the small angles involved require the beam be displaced by a magnetic chicane to facilitate removal and measurement of the particles (Fig. 4.16).
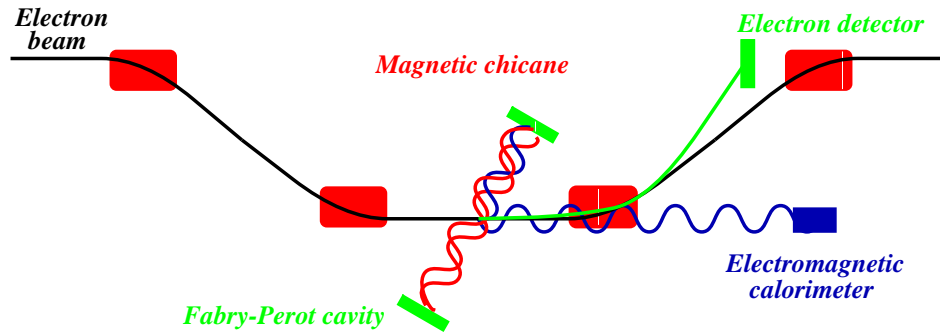
Figure 4.16: Schematic of Compton polarimeter. The scattered electrons have a slightly lower energy than the ensemble and thus are extracted from the beam as it is returned to its original path. In order to get sufficient statistics in a short time, the laser photon flux must be very high: this is done with a Fabry-Perot cavity.

4.5 Beam-line

The accelerator beam line is over 2 kilometers long and fitted with 2200 steering and focusing magnets to control the beam. The beam line is instrumented throughout its length with beam-position monitors. The combination of these instruments and control systems allows reliable manipulation of the beam in transit and fine tuning of the beam parameters. Instrumentation in the extraction arc to Hall A was crucial to the success of monitoring and correcting for helicity-correlated systematics. Small air-core steering magnets or 'modulation coils' fitted in this section (see Fig. 4.18) were used for modulating the beam so direct measurement of beam-line matrix elements could be done. The modulation and measurement of the transport matrix elements allowed the monitoring of and correction for helicity-correlated systematics of the beam.

4.5.1 Beam Current Monitors

Beam current to Hall A was measured by two beam current monitors (BCMs), located upstream of the target by 24.5 meters. The BCMs are stainless-steel cylindrical resonance cavities. They are roughly 15.5 cm in diameter and 15.25 cm in length. When the resonant frequency of a cavity is tuned to the beam frequency of 499 MHz they will output a voltage proportional to the beam current. This is accomplished by a loop antenna inside each, coaxial with the cavity. The loop radius of this antenna is chosen to couple to one of the resonance modes of the cavity. This

antenna, placed where the magnetic intensity $\vec{H}$ is largest, couples the beam signal out of the cavity. A smaller loop antenna, also coaxial with the cavity and the large antenna, is used to test the response of the larger pick-up antenna by sending it a 499 MHz calibration signal.

The BCMs make relative measurements of beam current and are linear over a broad range of currents. They are unable however, to measure absolute current. An Unser monitor[82, 83], placed between the BCMs, is used to provide an absolute calibration.   The Unser is a direct current transformer consisting of two identical toroidal cores driven in opposite ways by an external source. A DC-current passing through the cores produces a flux imbalance, which in turn, produces an output signal from the transformer windings. In the absence of beam current, the Unser's output is identically zero. The Unser is calibrated with a high-precision DC-current source sending current along a wire that is placed through the Unser to simulate the beam current. While accurate over short periods of time, the Unser monitor is subject to long term calibration drifts. Once the Unser is calibrated to absolute reference, it is used to calibrate the BCMs. The practice was to ramp the beam current from zero to a high current 5 or 6 times over a 10 minute period[2,3]. It was convenient to calibrate the BCMs once a day although tests have shown the BCMs need calibrating only every 3 or 4 days.

4.5.2   Beam Position Monitors

The position of the electron beam in the accelerator was measured in a number of locations at the injector, along the Hall A arc and in the Hall by Beam Position Monitors(BPMs). As shown in Fig.4.18, two BPMs were used in the injector and five between extraction and the target. The last two BPMs were upstream of the target by 1 and 6 meters respectively. These gave information about the beam angle through the target as well as its x-y position. The coordinate system for the hall and BPMs are shown in Fig. 4.17. The BPMs are simple devices consisting of 4 wire antennae in a cavity. The antennae are arranged in a square rotated $\pm45°$ from the horizontal-vertical (see Fig.4.17). The antennae pick up the fundamental frequency of the beam and the signal is inversely proportional to the distance between the

---

[2]$70 - 100\mu A$

[3]The Unser has an overall uncertainty of $\approx$ 250nAmps. Hence the relative error decreases at high currents.
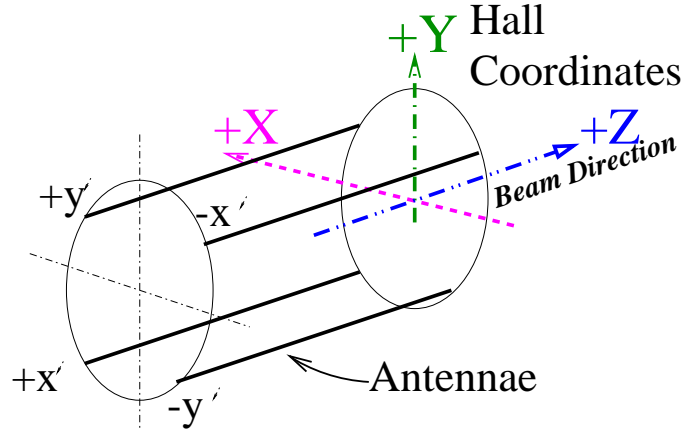
Figure 4.17: Schematic of beam position monitor showing the location of the four antennae in the BPM, indicated with lower case x', y'; are rotated 45° with respect to the Hall coordinate system. The coordinate system is right handed with Z defined parallel with the beam direction, Y vertical, and X horizontal.

beam and the antennae. The position is calculated as the difference-over-sum of the normalized signal from opposing antennae. The BPMs provide a position sensitivity of less than 20 μm and an angular sensitivity on the order of 8μrad.

Beam transport optics were provided by beam-line magnets in the Hall A arc. Analysis of the optics, along with controlled modulation of the beam position, allowed for in-depth studies of beam transport systematics. These studies were used to build transport matrix elements which, when used with the modulation analysis, gave information with which to correct for helicity-related transport asymmetries.

One of the BPMs was located in a high-dispersion point between two bending elements in the Hall A beam line (see Fig. 4.18). The beam position in this dispersion region is very sensitive to beam energy. This BPM information was used to test for beam-energy effects related to beam-helicity.

4.5.3   Beam Modulation

To measure the physics asymmetry we needed to understand how helicity-correlated variations in beam parameters contributed to the measured asymmetry. The detector signal, which is related to the scattering rate, can be expressed as: $D_{R(L)} = \sigma(E, X, Y, \theta, \phi)$, where E, X, Y, θ, and ϕ are the beam parameters of energy (E), beam position in X and Y, and beam angle on target in X and Y, respectively. As changes in beam parameters affect changes in the measured cross-section, helicity-

correlated fluctuations in these parameters would cause helicity-correlated system-
atic fluctuations in the measured asymmetry. Understanding how the beam-energy,
beam-position, and beam-angle on target are affected by helicity then, allows us to
subtract these effects from the measured asymmetry.

The technique used was to periodically modulate these beam parameters and
measure the cross-section sensitivity to fluctuations. Having then a relation between
fluctuations and cross-section, cross-section asymmetries can then be correlated with
measured beam fluctuations and corrected.

To implement this scheme, a selection of beam-steering coils were used to perturb
the beam slightly; then changes in these beam parameters were measured with BPMs
and the results were calibrated against fluctuations in scattering rates measured with
the detectors. Having obtained a scattering-rate sensitivity to fluctuations in the
beam parameters, we use this to calculate an asymmetry correction which we then
use to extract the physics asymmetry:

$$A_{exp} = A_{raw} - A_{corr} \qquad (4.18)$$

The steering coils were located in the Hall A beam line, upstream from the target;
see Fig. 4.18. The coil functions are designated in Table 4.4. We used a total of 7
modulation coils to modulate beam position in X and Y plus an energy vernier on
an accelerator cavity to modulate the energy.

Modulation Coil	HAPPEX Identifier	Deflection
MAT1C01H	Coil 0	Horizontal
MAT1C03H	Coil 1	Horizontal
MAT1C04H	Coil 3	Horizontal
MAT1C05H	Coil 4	Horizontal
MAT1C02V	Coil 2	Vertical
MAT1C06V	Coil 5	Vertical
MAT1C07V	Coil 6	Vertical
Energy Vernier	"Coil" 7	Energy

Table 4.4: Modulation Devices and Direction of Deflection. Note that although the Energy
Vernier is not a modulation coil, it is identified as a coil in the HAPPEX analysis software
and hence is listed as a coil in this table.

The steering coils are modulated one at a time according to a fixed step pattern as
shown in Fig. 4.19. The coils were driven by software controlled trim-cards capable
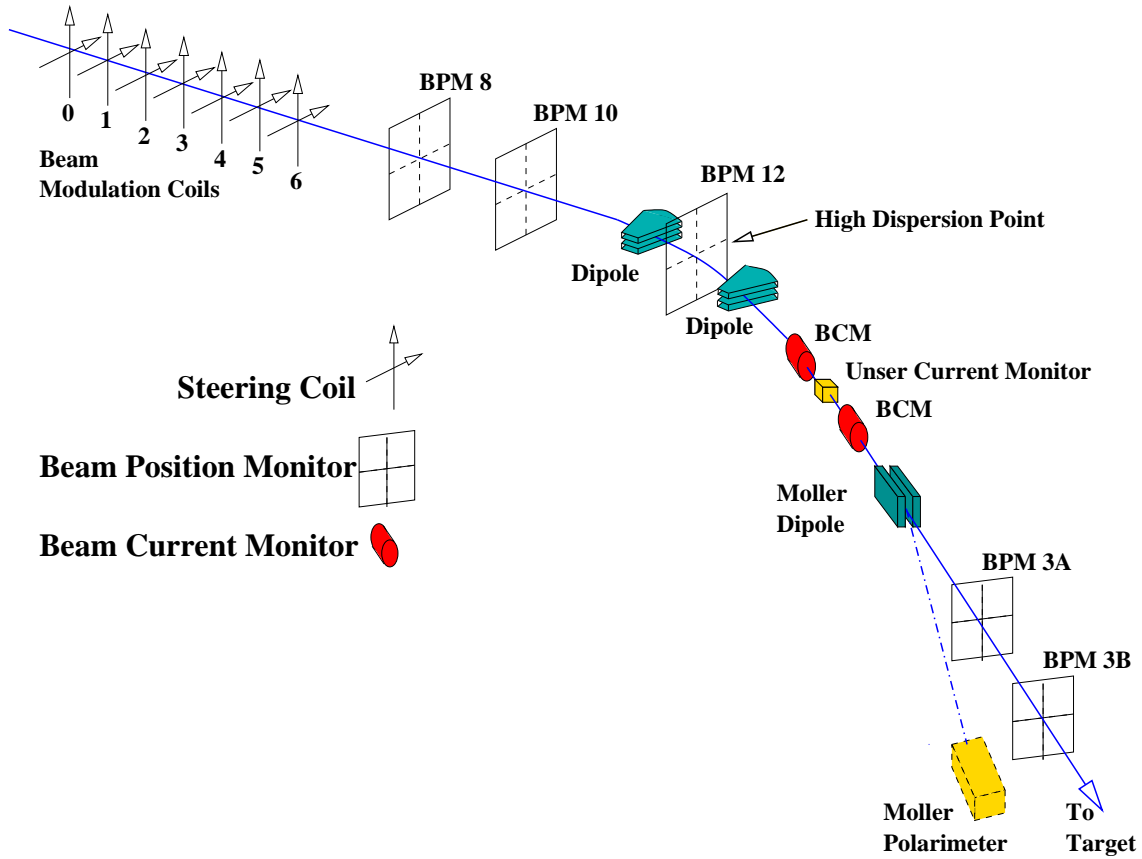
Figure 4.18: Hall A beam line instrumentation.

of delivering ±300mA maximum current which can deflect the beam as much as ±0.1mm. The amplitude, frequency, length and number of steps was controlled via the software.

Beam energy was modulated by ±500 KeV by an 'energy vernier' on an rf cavity near the end of the south linac. This resulted in a ΔE on the order of 100 ppm. Since modulation of the beam takes place in the accelerator, it necessarily affects the other experimental halls. The amplitude of this modulation however, is smaller than the energy noise in the unmodulated beam. The effects can only be noticed when integrating with the HAPPEX data acquisition over millisecond time scales. In this way, the energy modulation employed by HAPPEX was not noticeable by other experiments.

The modulation pattern result of all combined steering coils and the energy vernier is shown in the upper left graph of Fig. 4.20. Shown in units of 30Hz
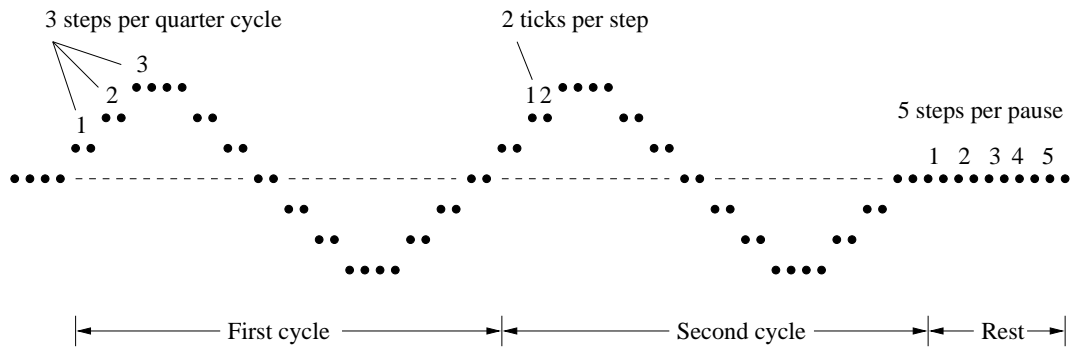
Figure 4.19: Modulation pattern. Each tick is 1 pulse pair (66.667 msec). The modulation pattern is 4.4 seconds long .

helicity-windows, the stepped pattern is color coded to show which flavor of coil was modulated. Red indicates that coil steering in X was modulated which is indicated by beam motion in X in the upper right graph. Green indicates steering in Y and is shown as beam motion in Y in the middle left graph. Energy modulation indicated by blue is shown as beam motion in the dispersive region between two dipole magnets. The last panel in the lower left shows the normalized detector rate signal versus pulse pair. The lack of a pattern here indicates that the magnitudes of the modulation is on the order of the detector noise and the response in the detectors can only be seen after averaging over many modulation runs. Beam modulation was conducted at the beginning of each mini-run (i.e. every $\simeq$ 10 minutes).
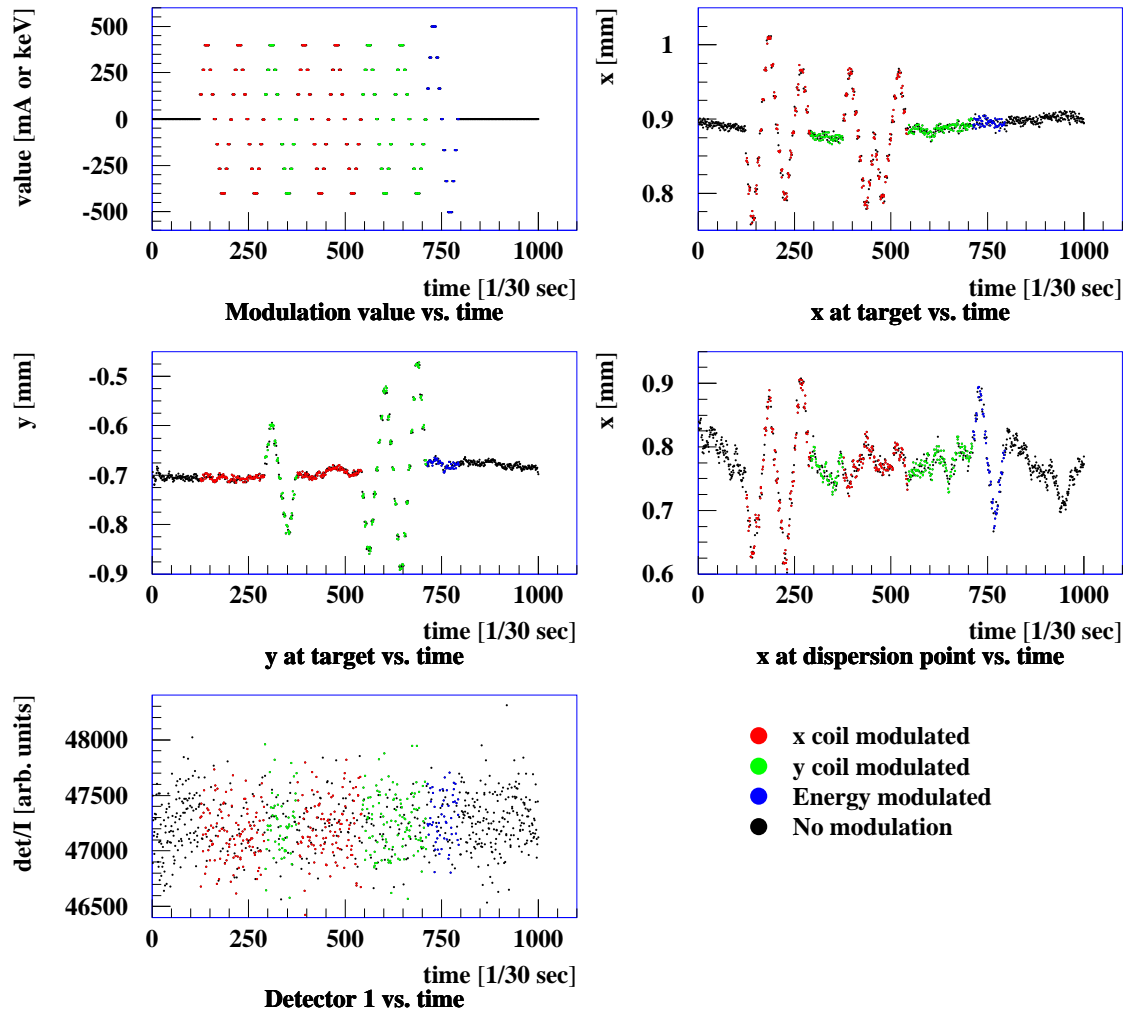
Figure 4.20: Beam Modulation.

4.6   Hall A Setup

Hall A is instrumented by two high-resolution spectrometers (see Fig. 4.21). The main spectrometer characteristics are given in Table 4.5. They are identical in the sense that either can be used to detect electrons or hadrons. The configuration for HAPPEX was to have both the Electron and Hadron spectrometers set to detect electrons. This served to double the acceptance which doubled the data rate. Electrons extracted from the accelerator enter the hall through the beam-line (hidden by the framework at the bottom of the figure) and are steered to the scattering chamber in the center of the Hall. Within the scattering chamber the electrons may interact with a variety of hadrons depending upon the target system desired. The target used for HAPPEX was liquid hydrogen. After interaction, the scattered electrons are detected by the spectrometers which measure their scattered angle, momentum and energy.
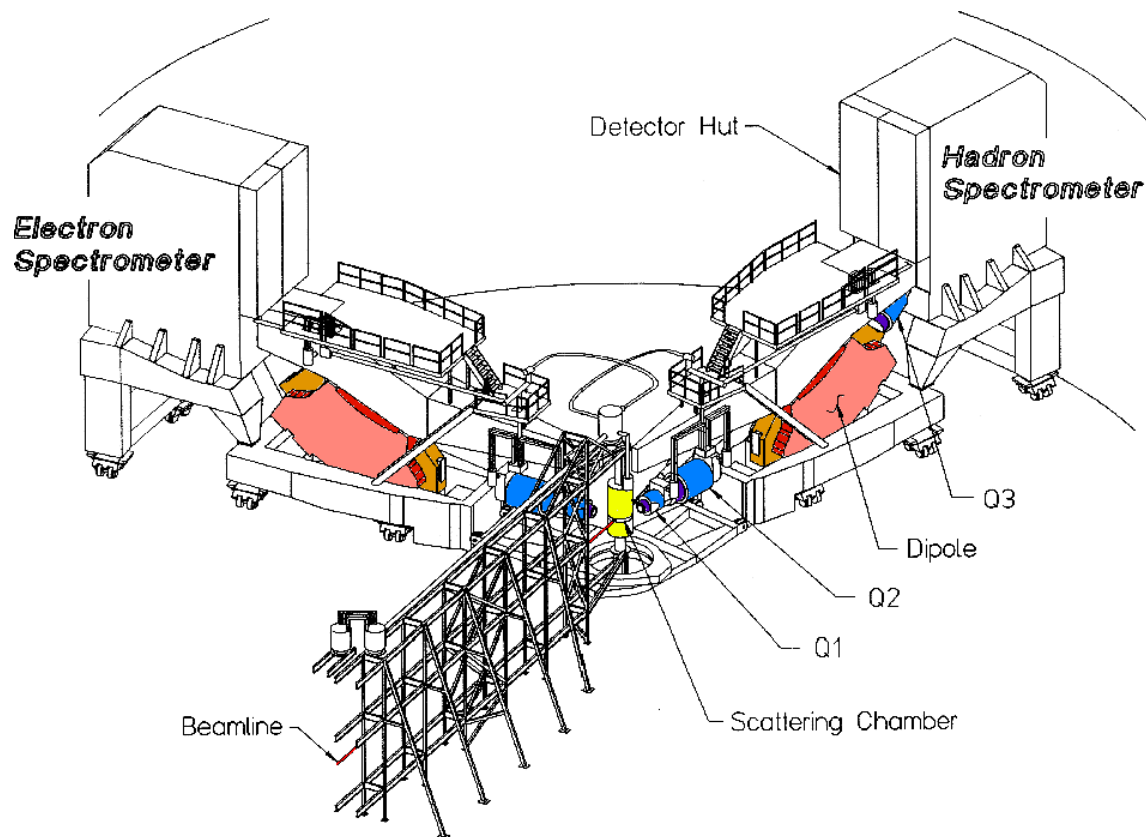
Figure 4.21: Hall A Layout.

4.7 High Resolution Spectrometer

The two identical spectrometers provide good particle identification, and precise measurements of angle, position and momentum. Because of the high rate necessary, the majority of the HAPPEX data would be integrated instead of reconstructed. For this to be possible, the spectrometers needed to spatially resolve the elastic events from the π threshold and other inelastic background events. The spectrometer optics to accomplish this are point-to-point in the dispersive direction, with the final focus in a plane located between a pair of Vertical Drift Chambers. The optical components are three $\cos2\theta$ quadrupoles (Q_1, Q_2, Q_3) and one radial indexed Dipole (D)[73]. They are ordered as $Q_1 Q_2 D\, Q_3$, as shown in Fig. 4.22. All of the magnets are super-conducting; the dipole is iron-cored with $\vec{B} \propto$ Radius providing natural focusing in the dispersive direction.

Bending angle	45°
Horizontal angular acceptance	±25 mr
Horizontal FWHM angular resolution	1.0 mr
Momentum dispersion	11.76 cm/%
Momentum range	0.3 to 4 GeV/c
Momentum acceptance	±4.5%
Momentum resolution	$2.5 - 4.0 \times 10^{-4}$ FWHM
Optical length	23.4 m

Table 4.5: Characteristics of High Resolution Spectrometers.

4.8 Detector Packages

Each HRS spectrometer has a pair of Vertical Drift Chambers (VDCs) used to precisely determine the position and angular coordinates of the particle tracks (see Section 4.8.2). Also, each spectrometer has at least two layers of scintillators for event triggering and time-of-flight information. Each also has a gas Čerenkov chamber for particle identification. In addition to the scintillators and drift chambers the HRSE (Electron Arm) also has Pb-glass pre-shower and shower calorimeters for the measurement of the total energy of electrons.
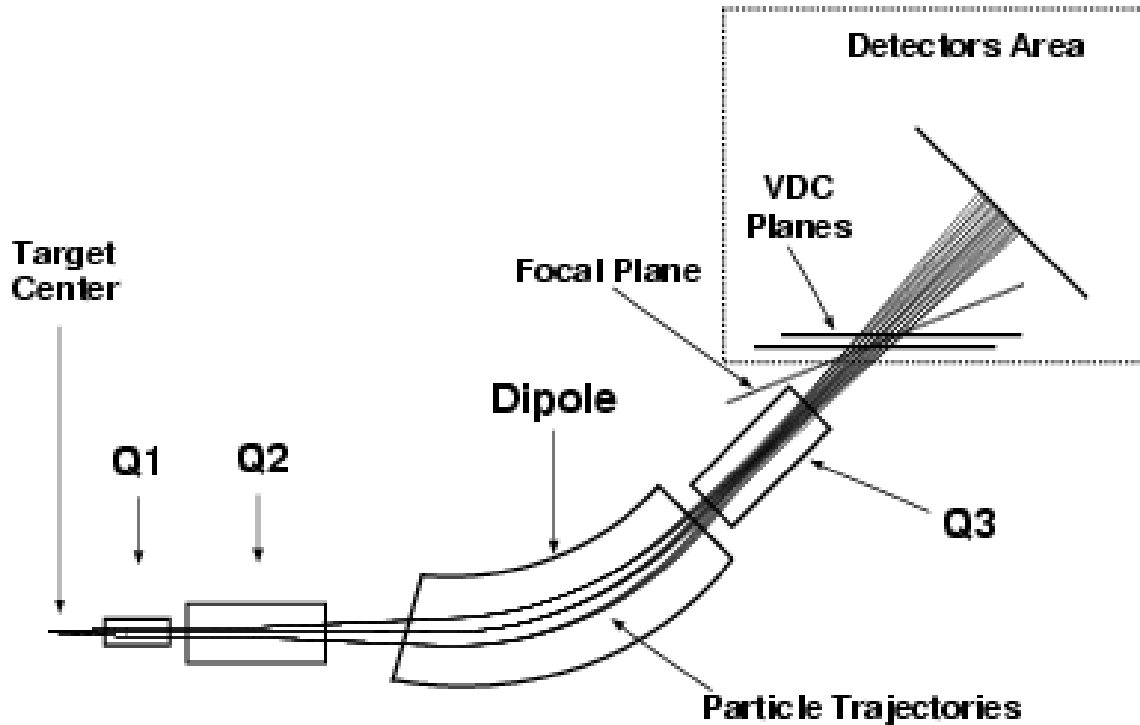
Figure 4.22: Hall A Spectrometer Optics Schematic.

The additional detectors in the HRSH (Hadron Arm) are an Aerogel Čerenkov detector, two pairs of straw wire chambers with a carbon analyzer between the pairs, and a third plane of scintillator paddles.

The HAPPEX detectors (discussed below) were placed above the VDCs in each spectrometer as shown in Figures 4.23 and 4.24. The detectors used for HAPPEX were the VDCs, HAPPEX detector and scintillator plane S2 (for triggers). Aerogel, gas Čerenkov and shower counters were not necessary and were not used.

4.8.1   Scintillators

Each spectrometer has two planes of scintillators, S1 and S2, spaced 2 meters apart and placed normal to the central ray. Each scintillator plane is segmented into 6 sections with 0.5 cm overlap on each section (Fig. 4.25). The long axis of each segment is perpendicular to the dispersive direction of the spectrometer. A 2" PMT is mounted on each end of each segment. The PMT signals are sent to ADCs and TDCs in the trigger electronics.

Installation of the HAPPEX integrating detectors above the VDCs required par-
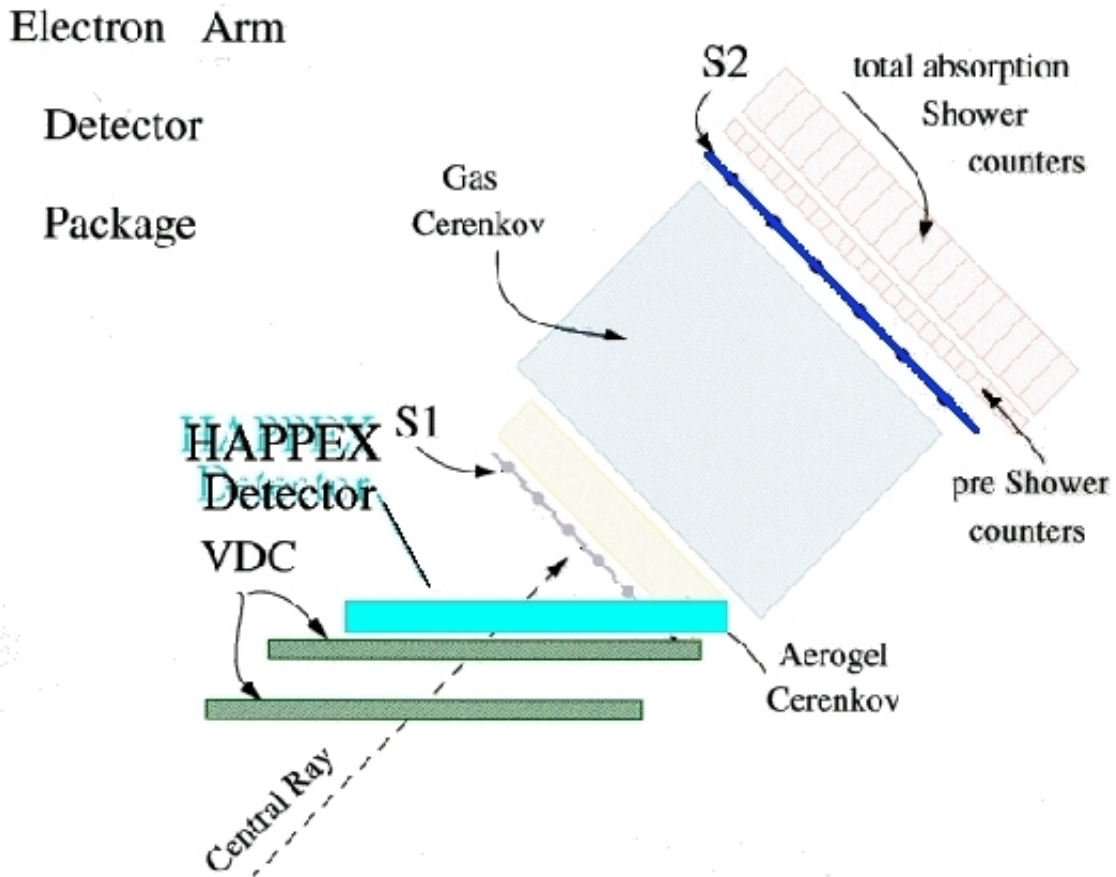
Figure 4.23: HRS-Electron detector stack.

tial dismantling of plane S1 (see Fig. 4.23). The S2 plane and the HAPPEX detectors themselves therefore, were used exclusively as the event triggering devices.

4.8.2   Vertical Drift Chambers

Particle position and angle are determined by the Vertical Drift Chambers[84]. Each spectrometer has a pair of VDCs, an upper chamber and a lower chamber as shown in Fig. 4.28. Each chamber has 368 sense wires set in two planes perpendicular to each other. These are set at 45° to the dispersive direction of the spectrometer (Fig. 4.27). The sense wires are gold-plated tungsten, 20 μm in diameter. Each plane of wires is sandwiched between high-voltage sheets of thin copper window held at -4.0kV. Each chamber is filled with an Argon-Ethane mixture (1:1 by volume).

As a charged particle traverses a VDC plane, ions and electrons are produced
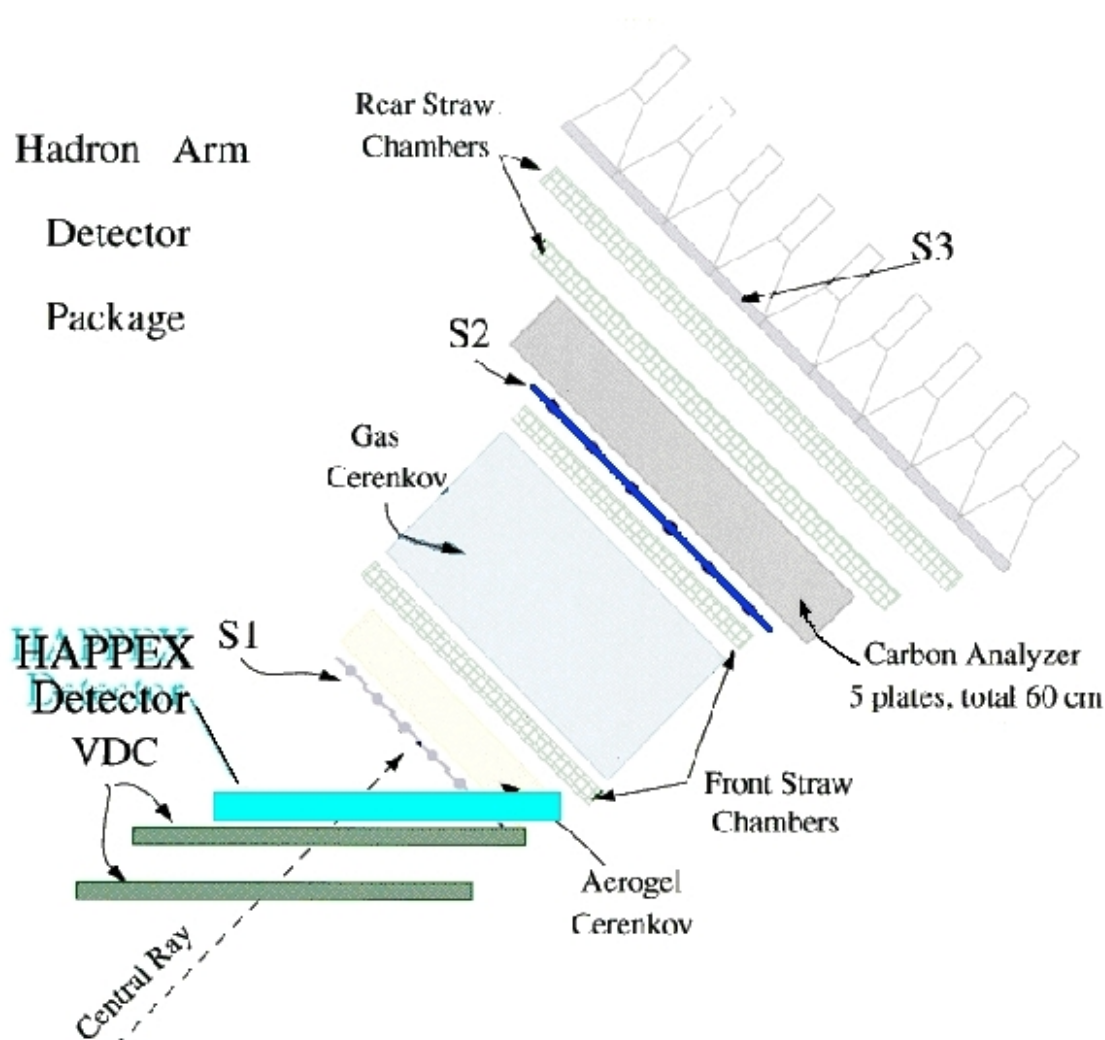
Figure 4.24: HRS-Hadron detector stack.

from the gas. The voltage differential between the wires and the -4.0kV planes cause the ions to drift towards the copper planes while the electrons drift towards the sense wires (Fig. 4.26). As the electrons near the sense wire, they enter a region where the electric field is sufficiently large to give them enough energy to cause additional ionizations of the gas atoms. As this avalanche continues, sufficient numbers of positive ions drift away from the wire, which induces a detectable negative signal on the wire.

The VDC electronics register this negative signal on the sense-wires. Knowledge of the drift velocity of the electron in the gas mixture allows the perpendicular distance (Fig. 4.26) to be determined. From these distances and wire positions, the
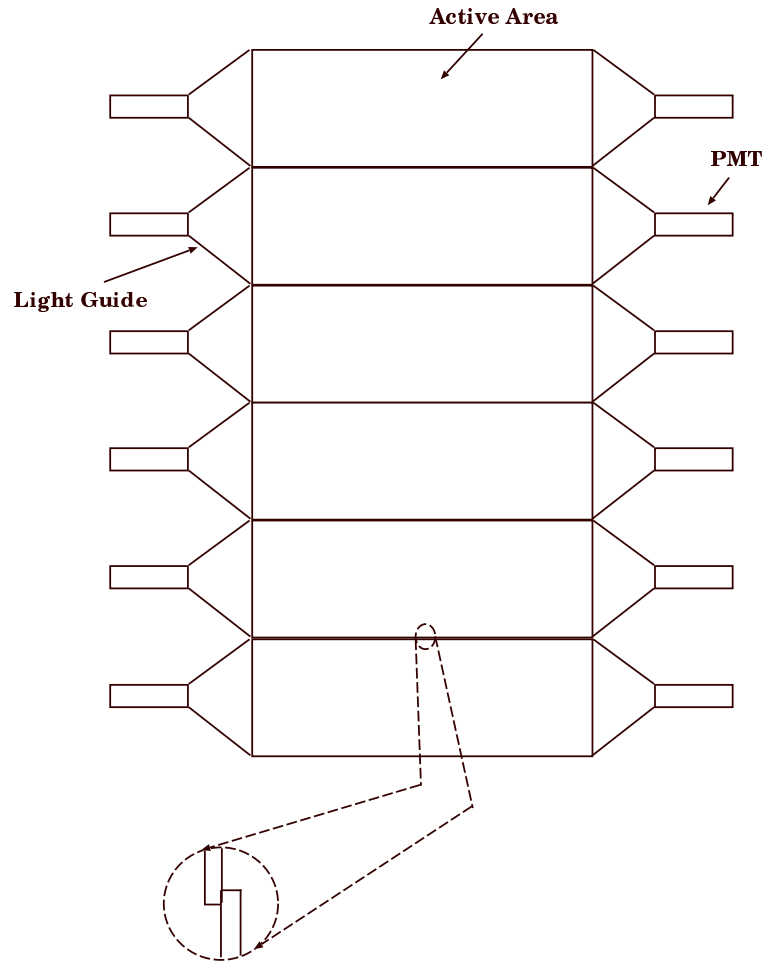
Figure 4.25: S1 and S2 scintillator plane schematic.

particle trajectory and crossing point is calculated. Two crossed sets of wires yield an (X,Y) position for the particle. The position resolution of each plane of wires is 225 μm (FWHM). Two chambers yield (x,y) and (x$'$,y$'$). Coupled with the spectrometer optics, information on the wire chamber position and trajectories allows translation of (x,y) and (x$'$,y$'$) into momentum. Individual particle trajectories can be reconstructed back to the interaction point in the target.
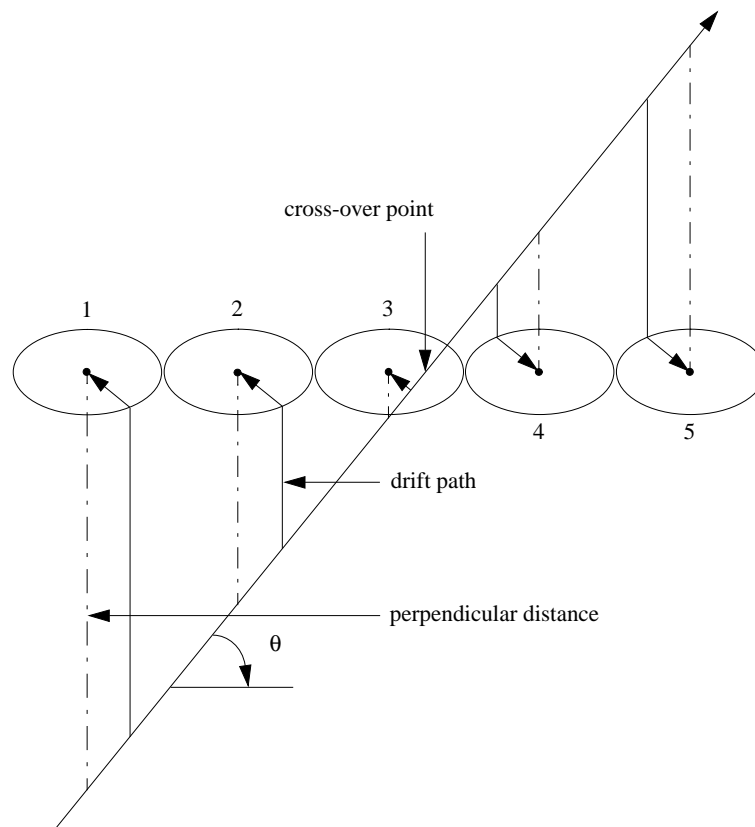
Figure 4.26: VDC Cascade. The drift path is the path of shortest drift time. The drift path is used to fit the distance perpendicular to the wire plane (dashed lines).
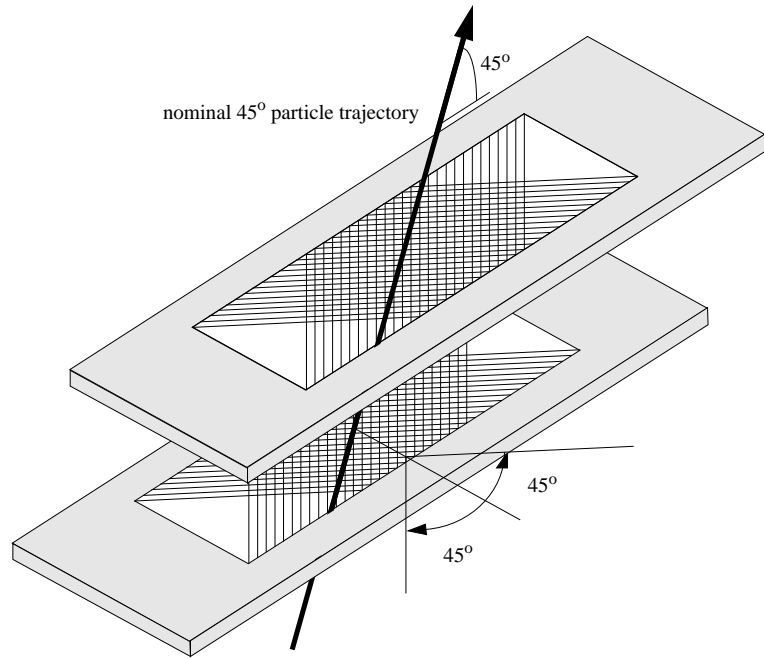
Figure 4.27: Schematic of VDC Pair.
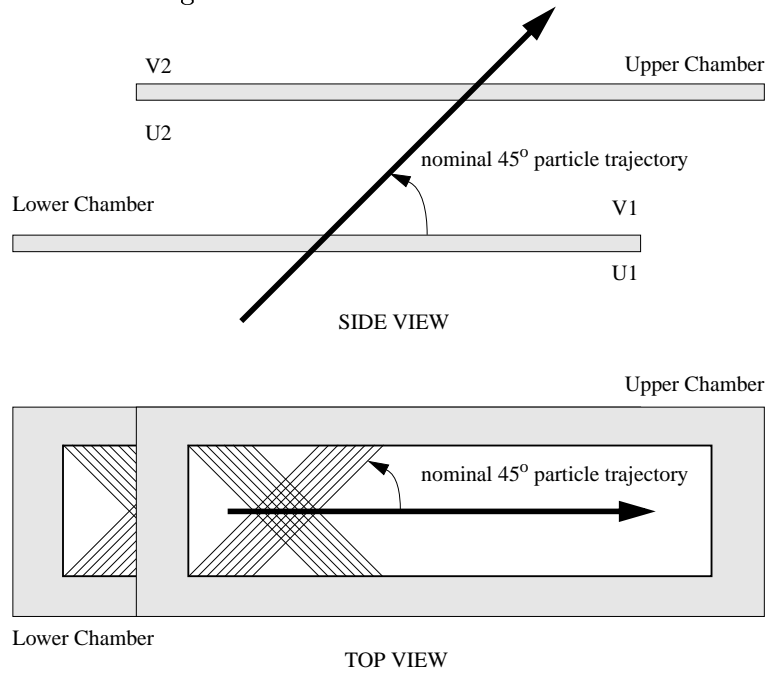
Figure 4.28: Side and Top Schematic of VDC pair. There are two wire planes (U1,V1) and (U2,V2) for each VDC Chamber.

4.8.3   Pb-Lucite Čerenkov Detectors

High data rates, on the order of 2 MHz per spectrometer, in addition to the aforementioned systematic concerns, placed stringent requirements on the HAPPEX detector system. Much of the HRS detector packages were designed for precise event-by-event reconstruction of data. The high data rates expected with HAPPEX precluded using the standard detector package. Thus an integrating detector scheme was adopted for HAPPEX.

The requirements for the HAPPEX detector were:

1. Energy Resolution. The statistical error in a counting experiment is inversely proportional to the number of events counted. For HAPPEX this is $\delta A^{\mathrm{PV}} \sim \frac{1}{\sqrt{N}}$. For integrated signals, i.e. HAPPEX, the counting statistics are modified by the energy resolution of the detectors as

$$\delta A_{(stat)} \sim \frac{1}{\sqrt{N}} \sqrt{1 + \left(\frac{\Delta E}{\langle E \rangle}\right)^2} \tag{4.19}$$

   where   N   is the number of events,$\approx 10^{14}$

   ΔE is the energy resolution of the detector, and

   $\langle E \rangle$ is the average detected energy.

   To not significantly affect the statistical uncertainty, we require an energy resolution of $< 15\%$.

2. Small Background Response. We would like the detectors to detect only elastically scattered electrons. This is not possible, however, as the detector will be sensitive to other particles that are scattered into the spectrometers. As no particle identification measures are used while integrating, all signals from such background particles are counted with the elastic electrons. Because of this inherent 'openness' to all particles, we require that the number of background particles incident on the detector remain small.

3. Radiation Damage Resistance. As HAPPEX is an integration experiment, it would suffice to measure total charge accumulation in the detectors. Lead glass calorimeters, a standard for total absorbers, would be ideal for this type of detector. Lead glass however, is susceptible to radiation damage. The high rate expected during HAPPEX, would deposit roughly 19.2 Gy of radiation

in the detectors. The resulting damage to a Pb-glass detector then would change its operational characteristics during the course of the run. As this is unacceptable, we require the HAPPEX detectors to be either insensitive or resistant to such radiation damage.

Čerenkov style calorimeters were chosen for the detector design as the total number of photons generated in such a detector is proportional to total energy deposited, which at the HAPPEX kinematics is proportional to the total number of electrons. To avoid the opacity of radiation damage which can accumulate in Pb-glass, Lucite^{TM4} was chosen as the optical medium. The long radiation length of Lucite however, required building the detector as a lead/Lucite layered configuration as shown in Fig.4.30. A detector of this style may operate as a total absorption calorimeter, where integrating over the signal gives a measure of the total number of scattered electrons. Design parameters are discussed below in section 4.8.3.1.

Limiting background response was largely a function of the spatial resolution of the spectrometers. Electrons were brought to the focal-plane of the spectrometers in a narrow strip well away from lower-energy pion-threshold events as is illustrated in Fig.4.29. This clean spatial separation allowed us to design detectors which would only be sensitive to elastically scattered electrons.

4.8.3.1 Simulations & Testing

GEANT

Simulations using GEANT were conducted to optimize the energy resolution of the lead/Lucite layers. The goal was to maximize the detector efficiency by maximizing the energy deposited in the detector by electrons. The varied parameters were: thickness of the lead, thickness of the Lucite, number of lead/Lucite layers, thickness and number of pre-radiators, and width of layers (to test edge effects).

GEANT simulations show the position of the electron/gamma shower[5] that occur in the detector. The simulation used one lead layer as a pre-radiator and was then adjusted to position the major body of the shower such that the maximum light output occurred in the center of the detector stack which is aligned with the

---

[4]Lucite^{TM} is a trade name for a clear acrylic made by Bicron.

[5]Electrons lose their energy almost exclusively by bremsstrahlung and photons by electron-positron pair production. This continues until the particle energy falls below E_c where the energy loss proceeds by ionization and Compton scattering, respectively.
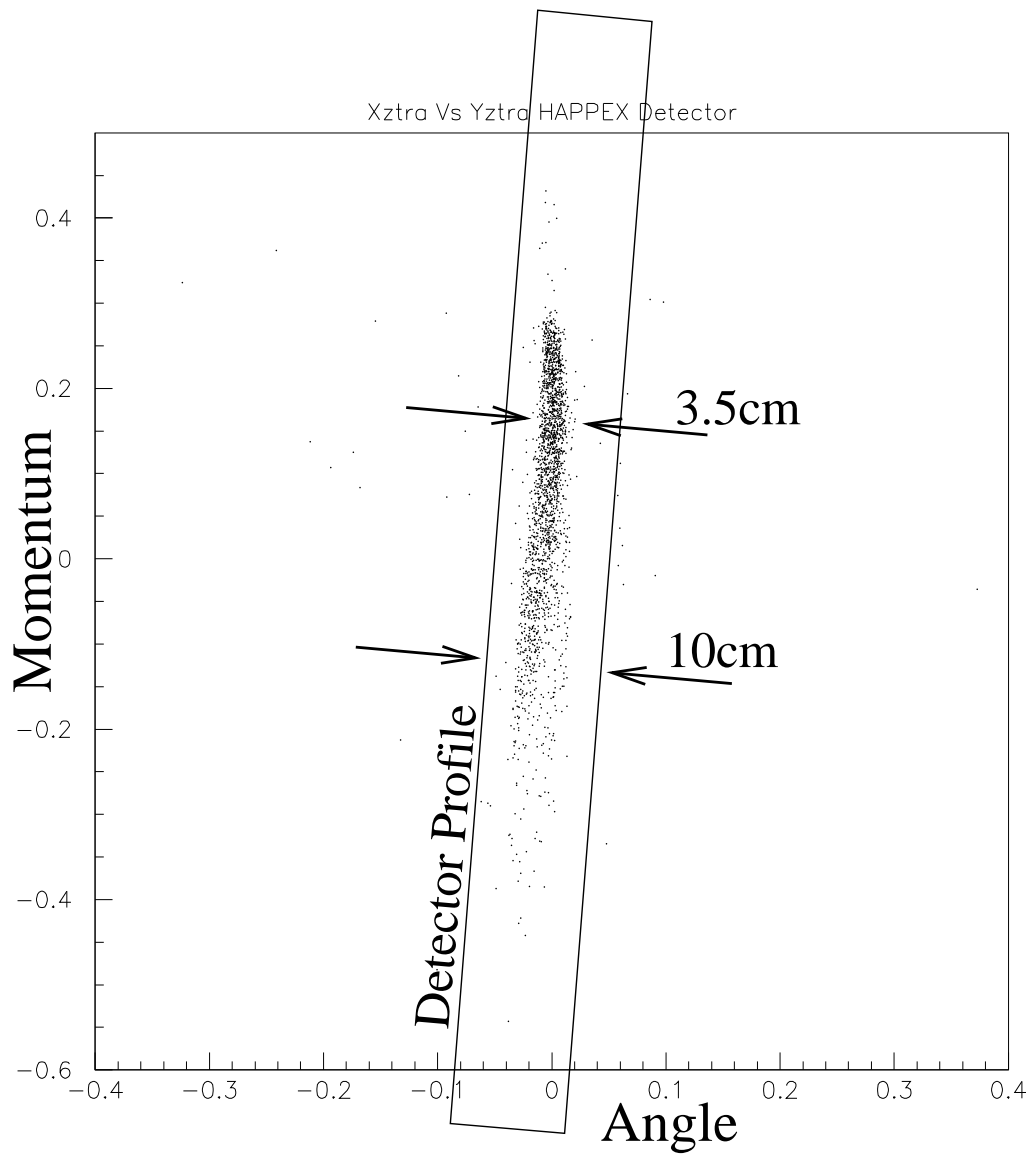
Figure 4.29: Elastic-electron stripe and detector profile. Data from an alignment run shows the stripe of elastic events on the focal plane. The box outlines the active lead/Lucite region of the detector. All of the elastic events and most of the events from the radiative-tail, entered the detector well within the active boundary.
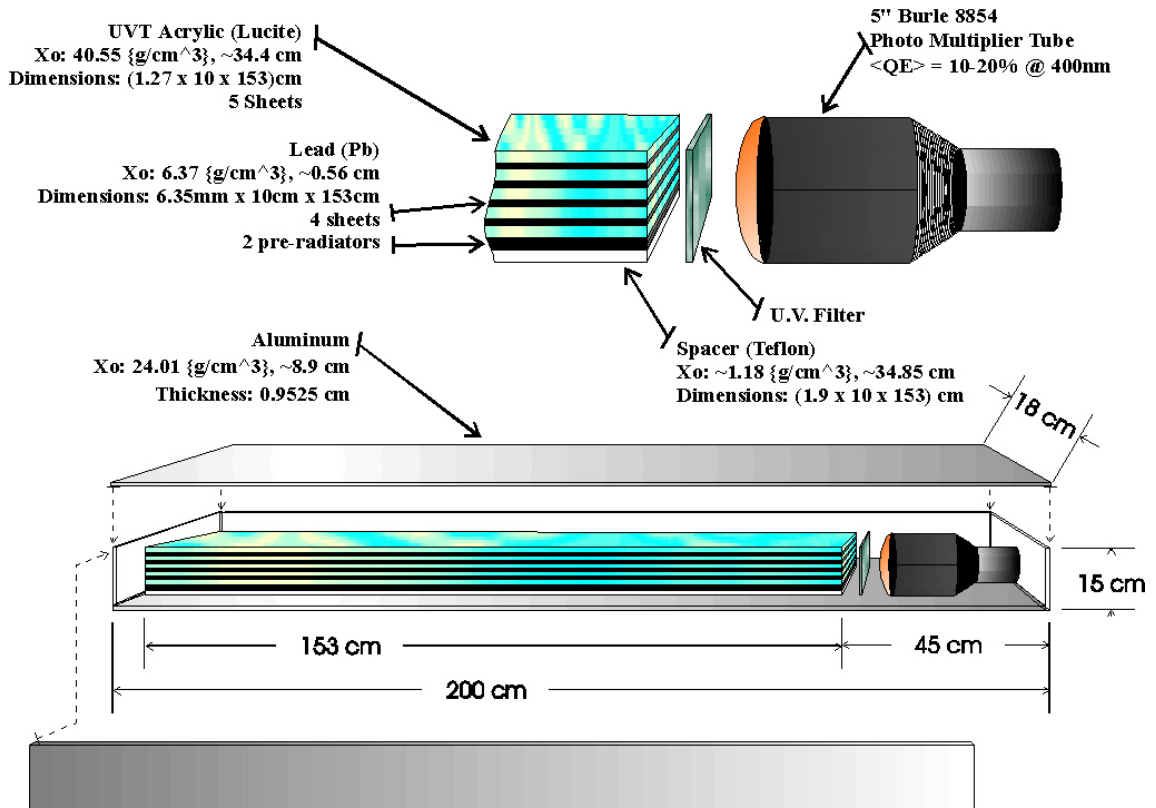
Figure 4.30: HAPPEX detector detail.
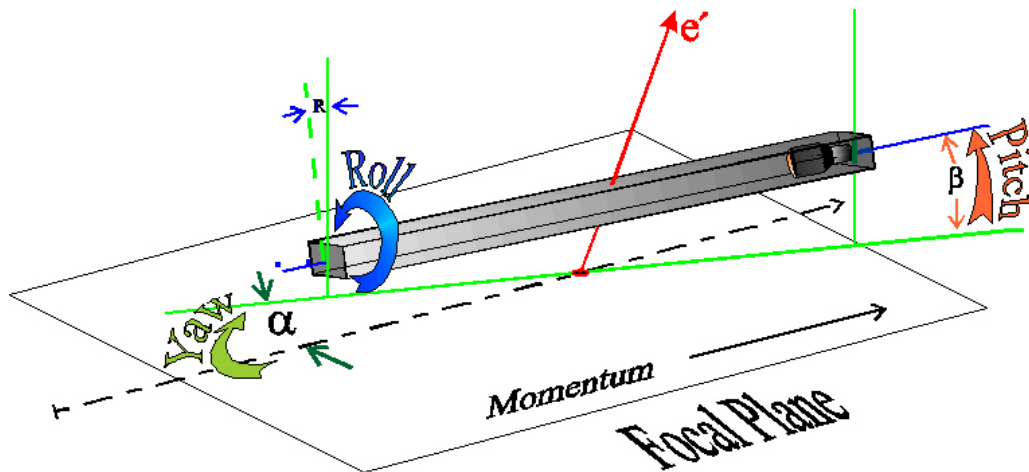
Figure 4.31: Detector positioning on focal plane.

center of the PMT. Once the pre-radiator thickness was chosen, a second simulation determined the number of lead/Lucite layers. Empirically, the energy resolution of such a detector is inversely proportional to the square root of the number of layers. Thus to optimize the detector's resolution, one needs only to increase the number of layers. A maximum energy resolution of 14% was decided to have negligible effects on counting statistics. It was determined that five lead/Lucite layers were sufficient to meet this requirement.

Once the general parameters were determined, the dimensions of the layers were rounded up to accommodate standard available stock from suppliers. These increases in dimension would increase the overall efficiency of the detector and were not simulated. The detector resolution therefore was slightly better than 14%.

The industry available stock dimensions were 1/4 inch thick lead sheets and 1/2 inch thick Lucite sheets. The width and length of lead and Lucite were cut to 10 cm by 150 cm. The 10 cm width of the active region was ample to negate edge effects as the width of the electron event-plane was less than 2 cm and the resulting shower would not exceed ±4 cm. A 1.9 cm Teflon spacer was used to raise and align the optical center of the detector layers with the optical center of the PMT. This spacer had negligible radiation length.

The final design for the HAPPEX detectors was a lead/Lucite layered construction shown in Figure 4.30. A scattered electron will encounter a 0.5 inch lead radiator followed by five layers of 0.5 inch Bicron BC-800 UVT Acrylic Plastic interspersed with four layers of 0.25 inch lead layers. Each layer of Lucite was wrapped with Teflon™. Teflon does not 'whet' the polished surface of the Lucite and so preserves total internal reflection. The entire stack including the PMT assembly was then made light-tight by wrapping with black Tedlar paper. In addition, the frame box of 3/8 inch aluminum was sealed with black RTV silicone.

All components used in the construction of the detectors near their active region were made of non-ferric materials to reduce the possibility of polarized Møller-scattered electrons from depositing energy in the detectors and causing false asymmetries.

This aluminum box was then suspended over the VDCs by a frame designed specifically for HAPPEX which allowed six degrees of freedom enabling precise alignment of the detector's active region with the electron event-plane (Fig. 4.31).

Detector Response

There were three aspects of detector performance that were of concern with regards to systematics. While the lead/Lucite construction guaranteed a strong response to incident electrons, we needed to ensure the linearity of the PMT signal, a low signal to noise ratio, and measure the light absorption characteristics of the Lucite layers.

A number of bench tests were conducted to calibrate the detector properties and verify there would be no major problems with the application. Simulations suggested the detectors would be very sensitive to the angle of the particle path due to the optics of their geometry. Also a concern, the Lucite construction of the optical elements had an attenuation per unit length that needed to be calibrated and corrected for if possible. In addition, the linearity of the photo-tubes and bases in low-light, high-gain situations needed to be calibrated.

Light Attenuation

The detectors used Bicron BC-800 UVT Acrylic Plastic for their optical medium. It must be noted that the rating of Ultra-Violet Transparency(UVT) for acrylics is a relative term. Bicron BC-800 UVT is transparent to frequencies much higher than standard acrylic however, in all, its UV response is similar to that of plate glass. The result is the Bicron BC-800 Acrylic has a strong attenuation per unit length for wavelengths shorter than 330 nm. As much of the Čerenkov light produced by the calorimeters is in the UV region, the amount of light entering the PMT, and hence PMT signal response, is inversely exponential to the distance between the PMT and the Čerenkov event.

Longer wavelength light was transmitted with less loss. The goal then was to limit the response of the PMTs to the length-attenuated UV while not hampering the light collection efficiency of the longer wavelengths. This was accomplished with a simple UV Filter consisting of a single sheet of Plexiglas with strong UV attenuation qualities (Fig. 4.30). What UV was not attenuated by the acrylic would be filtered out by this Plexiglas plate such that no UV entered the PMT. This greatly reduced the sensitivity of the detector to event location.

Photo-Multiplier Tubes

Five-inch Burle 8854 Photo-Multiplier Tubes were used for signal detection. These tubes, operated at a nominal voltage of 1200 to 2400 volts, have a gain of $\approx 5.1 \times 10^7$ at ~ 2000 V. Table 4.6 lists typical operation characteristics of the Burle 8854. To calibrate the linearity of the PMTs and bases, we used an arrangement of two high-intensity, blue LEDs mounted in the far end the central Lucite layer, facing towards the PMT. The LEDs were driven by a square-wave pulse generator. The linearity tests were a comparison of PMT signal of both LEDs together with the addition of both LEDs separately. In principle, if the tube-base combination was linear, the output for LED A + LED B would be equal to the sum of the LED A output plus LED B output.

Quantum Efficiency at 385 nm	22.5%
Maximum Anode to Cathode Voltage	3000 V
Maximum Average Anode Current	200 μA
Linear Pulse Current	0.13 A
Typical Current Gain @ 2kV	5.1×10^7
Typical Rise Time	4 ns
Typical Transit Time	78 ns

Table 4.6: Manufacturer's Data[85] on the BURLE 8854 PMT.

In order to test the PMT/base response as it would be applied in HAPPEX, the LEDs were driven in a timing regime close to that of the expected Čerenkov light:$\approx$10ns or so. The results showed a non-linear correlation from the tail of the light pulse signal. Investigation showed the non-linearity originated in the LEDs not the PMT/bases. To counter this problem, the LED pulse width was increased to $\approx$100ns. This increased the consistency of amount of light per pulse by allowing the diodes to turn on more fully. The resulting increase in light required increasing the width of the ADC gate and adding some delay. After increasing the ADC gate width to the maximum for our equipment, subsequent testing, while better, still showed a non-linear effect due to the transient vagaries of the LEDs. We were able, however, to set an upper limit of 0.14% based on these tests. LED linearity is discussed in Appendix D.

4.9   Target System - Overview

To meet the physics requirement of Hall A experiments, Jefferson Lab undertook the construction of a versatile, high-power cryogenic target system.

The cryogenic target system used for the first five of seven Hall A experiments was a milestone in control technology for sensitive measurements. Much of its functional robustness has evolved from many labs over many years. One of the striking features of this target system was its stability and adaptability to changing target requirements. This was accomplished under the constraint of maintaining very small temperature and density fluctuations while accommodating beam fluctuations of over one hundred μA. The need to maintain a constant cross-section for the physics target drove the need to maintain a constant density of the cryogenic target. Under these conditions, maintaining constant temperatures under the sudden and extreme changes of heat-power deposited by the beam was no small feat. The Hall-A cryogenic target system, however, did accomplish this with an operational simplicity and robustness which exceeded the expectations of the designers and experimenters.

The essentials of the cryogenic target (a.k.a. Cryotarget) were to provide target volumes of liquid Hydrogen, liquid Deuterium, and gaseous Helium. In addition each of these volumes needed to operate stably at as high a beam current as could be achieved. In the case of the Liquid Hydrogen target, a world record of beam power over 700 Watts was achieved in 1997. This is equivalent to a luminosity of $5 \times 10^{38} \text{cm}^{-2}\text{sec}^{-1}$.

The Cryotarget has four primary systems. These are 1) the cryogenic system, comprised of target fluids, cooling system and associated plumbing 2) the electronics, for control and operation 3) the software, for control and data processing and 4) Telemetry, for feedback and monitoring of cryogen and performance parameters.

4.9.1   Cryogenic Loops

The Cryogenic system can be thought of as being comprised of two parts. Part one is the plumbing and flow path of the cryogenic target fluid. Part two is the coolant and heat exchanger plumbing which supplies the coolant power to the cryogen fluid. The Cryotarget system provided 3 cyrogenically-cooled target blocks, each block having two available target cells of length 15 cm and 4 cm, respectively. Each block was connected to its own heat-exchanger and expansion tank. Each of these block-
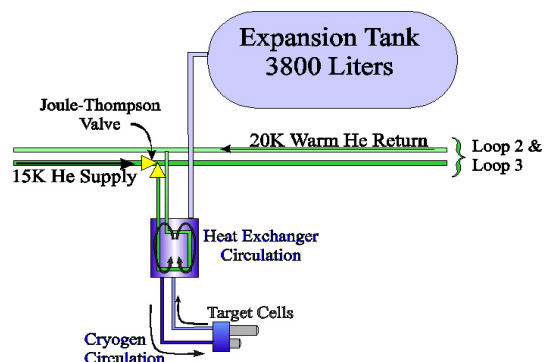
Figure 4.32: Schematic of Cryogenic Loop.

Figure 4.33: Photo of Cell Block and Target Cells. Cell block and target cell cans before assembly.

target combinations, including its heat-exchanger, was called a 'loop' or 'target loop'. In service these loops were named after the gas with which they were filled with. Thus one had the 'Helium Loop', 'Hydrogen Loop', and 'Deuterium Loop'[6]. Alternatively they were referred to as loops "1, 2, or 3". In addition, each of the block-target combinations were modular and could be changed with other cell designs, exchanged with each other, or removed independently of the other loops thus adding adaptability and redundancy to the system.

The target cells were cylindrical volumes containing the cryogenic target fluid of choice. The target-cells served only to hold the fluid in the beam path and allow for the beam to interact with the target material. Ideally, the target interaction would be only that of the electron beam and the target material. In practice there will be some interaction with the beam and the target-cell container. To both minimize this interaction and make it consistent so its contributions can be calculated, the target-cell material was chosen to be a very thin aluminum alloy. The thinest, most consistent aluminum material available comes from beverage industries who have had much practice in stamping thin-walled aluminum cylinders. By the sheer volume of cans produced, the quality of aluminum and consistency of construction is guaranteed.

The Cryotarget cells, were constructed from pre-fill blanks of Coors Beer™ can stock. The cells are about 15 cm and 4 cm in length, 6.48 cm in diameter with

---

[6]HAPPEX used only the hydrogen loop as deuterium or helium targets were not needed.

a sidewall thickness of 0.18 mm. To minimize the contribution of events from the aluminum the downstream window (bottom of the can) was acid-etched down to 0.09 mm; see Fig. 4.33.
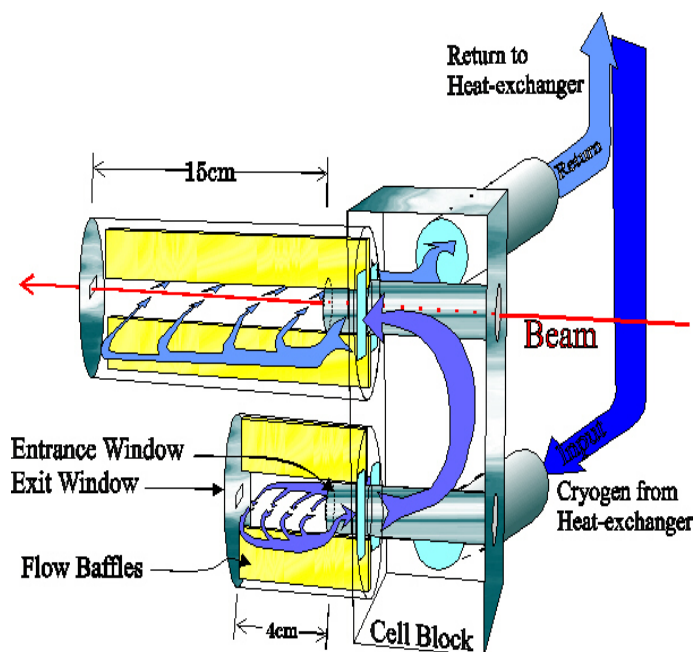
Figure 4.34: Target Cell Block. The Cryogen flows from the heat exchanger into the side of the cell block. It is ported into the bottom of the 4 cm cell first. Flow-diverters (yellow) maximize the flow through the beam reaction region and against the entry and exit windows, thus keeping them from melting from beam-induced heat. The Cryogen is ported from the 4 cm cell into the bottom of the 15 cm cell, through the beam reaction region, back to the cell block and returned to the heat-exchanger for cooling.

Cryogen temperature and density is maintained by continuous replenishment from the heat exchanger (see Fig. 4.36). The function of the heat exchanger is to remove the beam heat deposited in the target cryogen. This must be done rapidly to maintain a stable cryogen temperature. For liquid hydrogen the temperature was maintained at 19 K. The subsystems of the heat-exchanger are the fan or pump, the exchanger itself, the high and low power heaters, and thermometry. Thermometry will be addressed in section 4.9.2.3.

The beam-warmed cryogen needs to be constantly cycled out of the cell-block through the cooling fins of the exchanger. A dual-impeller pump (shown in blue in Fig. 4.36) in the center of the exchanger pumps the cryogen out of the cell-block and into the top of the exchanger. The flow speed of the cryogen through the cell and cell-block was determined by cooling requirements and beam heating. By

Figure 4.35: Photo of Target Cells. The down-stream 'exit' window can be seen. The cross-hairs on the ends were used in process of measuring the window thickness. The target cells and cell-blocks are wrapped in layers of reflective mylar to reduce thermal radiation and improve cooling efficiency. The Solid target ladder is below the edge of photo.
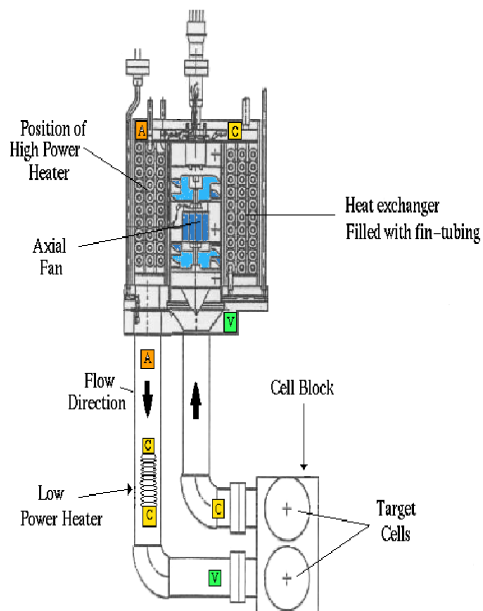
Figure 4.36: Heat-Exchanger Loop
Cernox temperature sensors: 'C' (Yellow)
Allen-Bradley sensors: 'A' (Gold)
VPTs: 'V' (Green)
Pump: Blue

changing the speed of the pump, the refresh speed of the cryogen through the cells can be increased or decreased. The mass flow of the cryogen can be determined from its change in temperature across a known power source. The mass flow was measured between the two Cernox thermometers before and after the Low-power heater (see below) and again before and after the Cell Block. The mass flow can then be used to calculate the flow rate through the target cell. Under the broad range of beam parameters, a flow speed of 20 cm/s was optimal for maintaining constant temperature of the hydrogen loop.

The exchanger was cooled by 15 K gaseous ^{4}He supplied from the End Station Refrigerator (ESR). The amount of coolant supplied to each loop could be adjusted by a Joule-Thompson valve system to limit the draw from the ESR. The nominal flow rate from the ESR was between 9 to 12 grams/s, however up to 25 grams/s coolant was available under special conditions. Usually this 25 grams/s coolant was shared between the Hall A and Hall C cryotargets.

Heaters were required for maintaining the system at a constant temperature. Each loop had two heaters; a 'high-power' (HP) heater capable of 700 Watts and a 'low-power' (LP) heater which provided 45 Watts of heat. Control of the LP heater was fed back directly from Cernox resistors to the heater's power-supply. The response parameters of the low-power heater was set remotely, and this heater was allowed to operate independently of other controls. The set point temperature for this heater was slightly lower than the running temperature, so this heater would normally output no heat to the system. It was used predominantly to compensate for long term, slow temperature fluctuations of the target's 'idle-state' when the HP heater and beam were off. The HP heaters, on the other hand, were designed to mimic the heat load of the beam. As the beam could cut on or off instantly with no warning, the HP heater needed to respond in kind. There was a few millisecond delay between a beam change and response in the beam-heat loading of the target. During this time, the HP heater would start and the change over from beam-heat load to HP heat-load was so smooth that temperature fluctuations were less than 1 K.

Operation of the Cryotarget required balancing coolant power with heating. The ESR's mass-flow and cooling power was limited in its response time to changing heat-load needs of the Cryotarget as the target responded to temperature changes from changing beam conditions. Any changes in coolant mass-flow needed time to flow into the heat exchanger, change and regulate its temperature, then this temperature needed to change and regulate the temperature of the Cryogen fluid then to be pumped to the target cell where the actual heat-load was in flux. These events required tens of seconds while the events causing the changes in heat flux occur on the order of milliseconds. To account for this, the system operated by estimating the amount of beam heat-load expected, supplying slightly more than this equivalent of cooling power from the ESR, and making up the difference with the HP heater.

4.9.2 Specifications

4.9.2.1 Luminosity and Heat Deposition

Table 4.7 shows the power in Watts for heat deposited at 100μA of beam. In practice the beam-heat deposition was somewhat less. This was due to differences

in the actual beam emittance and cryogen pressure and density which caused the actual heat deposited to be lower. Beam rastering also was not accounted for. This increased the apparent cooling efficiency and allowed, overall, a higher beam current on target.

	Hydrogen	Deuterium
Density (g/cm^3)	0.07230	0.1670
Length (cm)	15.0	15.0
$\frac{1}{\rho}\frac{dE}{dx}$ (MeV cm^2 g^{-1})	5.4	2.7
Power (W)	586	676
Luminosity (cm^{-2} s^{-1})	4.1 $\times 10^{38}$	4.7 $\times 10^{38}$
X$_\circ$ (g/cm^2)	61.28	122.4

Table 4.7: Luminosity and heat deposition in the target at 100 μA beam current. This does not include cell-window heating effects (caused by the beam heating the aluminum cell windows).

4.9.2.2   Cryogen Characteristics

The target density is primarily dependent upon temperature. Cryogen density is a largely a function of state, pressure and temperature with the primary dependence being on temperature. The typical operating conditions are given in Table 4.8.   The cryogens H_2 and D_2 can exist in different molecular states which arise

Target Liquid	Temperature K	Pressure psia	Density g cm^{-1}
Hydrogen	19.00	26.0	0.0723±0.00007
Deuterium	22.00	22.0	0.1670±0.0005

Table 4.8: Typical target operating parameters.

from the different relative orientations of the two nuclear spins in these diatomic molecules. These different states, ortho and para, have different densities based on the intermolecular spacing in the two states. The equilibrium ortho-para composition is temperature dependent. Room temperature H_2, for example, is composed of 75% ortho-hydrogen (nuclear spins in the same direction) and 25% para-hydrogen

(nuclear spins in opposite directions). The density differences of different mixtures of ortho-para mixtures is very small and the difference between normal, room temperature hydrogen and pure para-hydrogen is about 0.5-0.7%[86]. At the operating temperature of 19 K the combination is almost 100% para-hydrogen. The hydrogen has some impurities which act as catalysts for ortho-para conversion. After a few days, this conversion will reach equilibrium. The uncertainty in the density due to the uncertainty in the knowledge of the molecular state mixture is negligible.

The density (ρ) dependence on pressure (P) is $\frac{1}{\rho}\frac{d\rho}{dP} = 0.01\%$/psia. The measurement of the cryogen pressure using the pressure transducers has an uncertainty of about ± 0.3 psia. Together this leads to an error of less than 0.01% in the density due to the pressure measurement.

4.9.2.3 Thermometry

Temperature was monitored in each of the three loops by three different temperature sensors. The operating ranges of these sensors overlapped providing redundancy. Agreement between the sensors was so reliable that anomalous differences were regarded rather as curios than alarming. Anomalies did occur over the period of the Cryotarget operation as various sensors failed from radiation damage.

Each target loop used three types of temperature sensors; Cernox, Allen -Bradley, and Vapor Pressure Transducers(VPTs). See Figure 4.36 for their placement. The primary and most accurate temperature sensors were Cernox Resistors, CX-1070-SD. Each loop used two on the cell-block inlet side, before and after the LP heater, one on the outlet side, and one in the heat exchanger. The Cernox in the heat exchanger was calibrated from 4 K to 300 K while the three in or near the cell block were calibrated from 4 K to 80 K. Calibration was provided by the manufacturer, LakeShore. The calibration data was programmed into the monitoring units, Oxford Temperature Controllers, Models ITC 501, ITC 502.

The Cernox sensors were tested in JLab's Vertical Test Area prior to installation. This facility consists of large, vertical dewars for testing the radio-frequency response of the accelerator's super-conducting cavities. Here the Cernox sensors were absolutely calibrated to within ± 50 mK in the operating temperature region (see Fig. 4.37). The Cernox resistive sensors were used predominately to monitor heat-load feedback for the operation of the heaters. Should one of the Cernox sensors fail, the
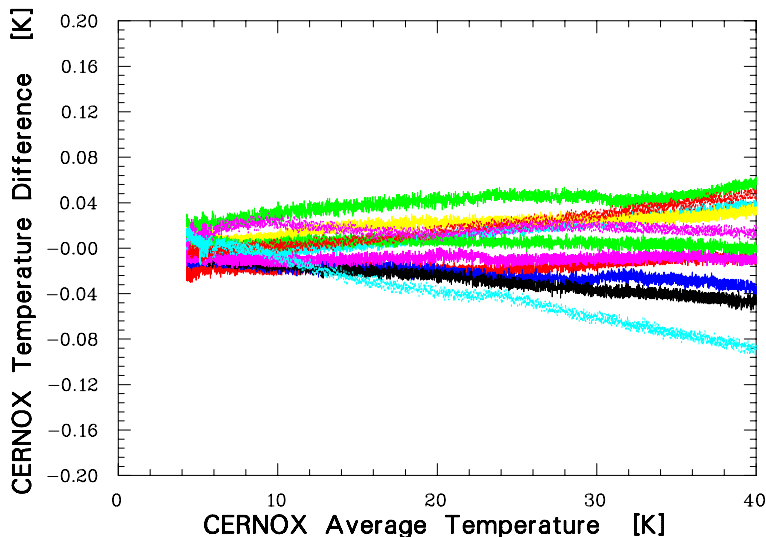
Figure 4.37: Typical Cernox calibration graph. Shown on vertical axis is the Cernox deviation from average: $\delta t_i / \langle t \rangle$ where i is one of ten Cernox resistors. Although this figure shows temperatures up to 40 K, the calibration range of the Cernox resistors is from 4 K to 80 K.

feedback could be changed in controls to another thermometer. The Allen-Bradley temperature sensors (also resistive) were less accurate than the Cernox but were calibrated up to 300 K. These were used mainly as a back up to the Cernox and for the cool-down and warm-up operations of the target system. There were two Allen-Bradley sensors per loop, one at the cryogen-gas inlet to the heat exchanger and one in the target-cell inlet.

The VPTs were the third system to monitor temperature of the cryogen loop. These operated on a principle different from the Cernox and Allen-Bradley resistors and were intrinsically radiation hard.

Each VPT consisted of a small bulb-like stainless steel tube, 4.74 mm diameter × 20.5 mm in length. The bulbs were located in the inlet port of the cell-block and at the bottom of the heat exchanger (see Fig. 4.36). The bulbs were connected by 22 meters of stainless capillary tube to Sensotec Pressure Transducers. The VPTs and capillary tubes were plumbed into a pressure manifold that allowed each VPT or bulb to be isolated from any other part of the system. This allowed each bulb to be filled and purged individually or any combination, including the entire group. Similarly, the VPTs could be isolated, removed, individually calibrated, or group calibrated. The VPT system relies on the vapor pressure curve of H_2 which has

a sensitivity of $\frac{dP}{dT} = 5$ psia/K at 21 K[86]. The Sensotec pressure transducers are current devices which have a response of 0.075 mA/psia and are read out by Sensotec SC200 current monitors with a sensitivity of a few μA. With the pressure-temperature function this gives a temperature sensitivity of δT ≈ 50 mK. Calibration was straightforward and done by isolating the VPT(s) of interest, pumping the pressure down to vacuum, setting the SC200s to this transducer current (≈ 4 mA) corresponding to zero pressure. Next, the manifold and VPTs are pressurized to 200 psia as read from a Walice & Tiernan absolute pressure gauge. The SC200s are then set to this new transducer current (≈ 20 mA) corresponding to 200 psia.

Charging the VPTs was accomplished by alternatively pumping down to vacuum then flushing the capillary and tubes with hydrogen. Next, the respective tube was filled with H_2 or D_2 as required. The tubes and capillaries were charged to about 40 psia. As the target loops are cooled, the gas in the capillaries and tubes condenses to liquid, filling the VP-bulbs to about 1/2 volume at 14.6 psia.

The VPTs while radiation-hard were reliable but slow. Their response time was moderated by thermal conduction of the stainless steel tube and the weld-point region of the tube in the cryogen passage. While the VPTs respond quickly, the thermal lag in response time is not ideal. The Cernox, with less mass, responded faster, thus were more suitable as feedback for the heater controls.

The largest target-density error came from the temperature (T) dependence which is $\frac{1}{\rho}\frac{d\rho}{dT} = -1.5\%$/K. The ± 50mK uncertainty of the Cernox resistive thermometers then leads to a density error of less than 0.1% due to temperature uncertainty.

4.9.2.4   Target Windows

The down-stream or exit-window of the target cell (see Fig. 4.35) is the bottom of the beer can. The aluminum in this region of the beer can was thinned by acid etching. The up-stream or entry-window was aluminum foil soldered onto the cell entrance tube (see Fig. 4.34). The thicknesses are specified in Table 4.10, and the interaction parameters are specified in Table 4.9.

The nominal target lengths are 15 cm and 4 cm. The cell length, corrected for thermal contraction of the aluminum at the operating temperature (0.5% @ 20 K.) is specified Table 4.10.

	Upstream Window	Downstream Window
Al Alloy	5052	3004
Density (g/cm^3)	2.68	2.71
Thickness (μm)	71.12	101.6
$X_\circ$ (g/cm^2)	23.85	24.12

Table 4.9: Upstream and Downstream Target Windows Material. The average thickness of the downstream window is used in this table.

Target Loop	Cell	Cold Length (cm)	Upstream Window (cm)	Downstream Window (cm)
1	15 cm	14.91±0.02	0.0071±0.0003	0.0107±0.0005
	4 cm	3.91±0.01	0.0071±0.0003	0.0117±0.0005
2	15 cm	14.95±0.02	0.0071±0.0003	0.0094±0.0005
	4 cm	3.78±0.01	0.0071±0.0003	0.0089±0.0005
3	15 cm	14.94±0.02	0.0071±0.0003	0.0097±0.0005
	4 cm	3.93±0.01	0.0071±0.0003	0.0091±0.0005

Table 4.10: Cryotarget Cell Dimensions. HAPPEX used the 15 cm, loop 2 (hydrogen) cell.

4.9.2.5   Target Ladder and Dummy Cells

Solid targets were provided on a target ladder suspended below the cell-blocks. Shown in Fig. 4.38, is a pictorial from the graphic user interface of the target positioning controls. The target assembly was mounted on a motorized elevator system. When a particular target was selected from a menu, the elevator would raise or lower the structure as needed to place the selected target in front of the beam. The solid targets (see table 4.11) included (but were not restricted to) a BeO target for visual position verification with the scattering chamber camera, a carbon target, and number of aluminum targets ('dummy cells') arranged such that their aluminum elements would mimic cryogenic target cell ends. These were used for estimation of background contribution from the aluminum end-caps of the cryogenic cells. Specifications for the Dummy-cell material are given in Table 4.12 and their positions in Table 4.13.
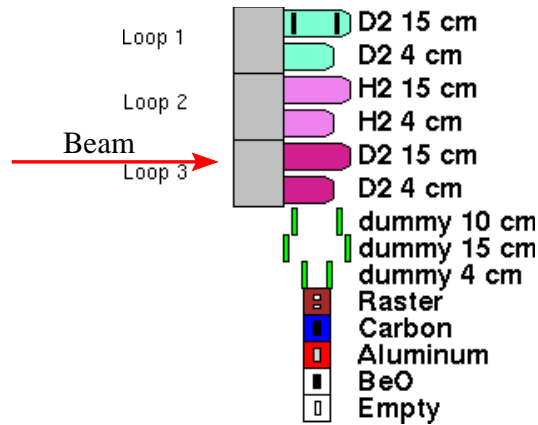
Figure 4.38: Target Position Graphic. This schematic shows the position of the target with respect to beam path and position of solid ladder targets with respect to cryogen cells.

Target	C	Al	BeO
Thickness (mm)	1.016±0.003	1.016±0.1	0.508±0.01
Dimensions (mm)	25.4×19.05	25.4×19.05	25.4×19.05
Density	223.20±0.14 mg/cm^2	2.71 g/cm^3	—

Table 4.11: Solid target thicknesses and materials.

Target	10 cm Dummy		15 cm Dummy		4 cm Dummy	
	upst	dnst	upst	dnst	upst	dnst
Al Alloy	6061	6061	6061	6061	6061	6061
Density (g/cm^3)	2.71	2.71	2.71	2.71	2.71	2.71
Thickness (mm)	0.9385	0.9144	0.9868	0.9868	0.32	0.3112
X$_\circ$ (g/cm^2)	24.12	24.12	24.12	24.12	24.12	24.12

Table 4.12: Dummy cell target thicknesses and materials.(upst=up-stream, dnst=down-stream.)

Dummy Target cm	z position of upstream foil mm	z position of downstream foil mm	Cold distance between center of foils cm
10	-47.77±0.2	+51.86±0.2	9.96±0.03
15	-73.15±0.2	+76.31±0.2	14.95±0.04
4	-17.79±0.2	+22.47±0.2	4.03±0.01

Table 4.13: Dummy Cell Target z Positions and Lengths.

4.9.2.6   Scattering Chamber

The Cryotarget assembly was housed in the scattering chamber. This was a large cylinder, 104 cm in diameter, centered on the spectrometer pivot. This was maintained under a 10^{-6} torr vacuum to minimize multiple scattering from air as well as to provide additional insulation to the cryotarget. The chamber was connected directly to the Hall A beam pipe on the upstream side and to the beam-dump pipe on the downstream side. After leaving the cryotarget the scattered particles would pass through the chamber exit windows, 0.4064 mm thick aluminum foil.

The beam dump pipe was maintained at 10^{-4} torr vacuum to reduce background radiation in the Hall. At the end of this pipe is the beam dump proper, a tank of water-cooled aluminum plates where the beam energy is deposited.

4.9.3   Control System

The Cryotarget control system is a combination of software known as EPICS (Experimental Physics and Industrial Control System; see below) running on various workstations and hardware (sensors, motors, valves) monitored and accessed by a finite state machine. The physical and logical architecture are compared in Fig. 4.39.

4.9.3.1   IOC

The target control systems involve 13 serial devices, two relay boards and five I/O boards that are queried and controlled, on time scales of 0.1 to 10 seconds[87, 88]. The finite state machine and database is loaded into the Input/Output Controller (IOC) which then communicates with the hardware devices and sensors.

The IOC for the cryotarget is a Motorola MV162-532 chip on a circuit board which sits in a VME crate. The communication with the hardware is through the IOC. In the right half of Fig. 4.39 is a schematic of the actual software tools which make the hardware communication possible. For the cryotarget, programs such as MEDM and TCL were used to develop GUIs (Graphical User Interfaces) for each piece of hardware to be controlled. When the status of a hardware device is queried or changed, the GUI communicates with the IOC via a network protocol known as channel access.
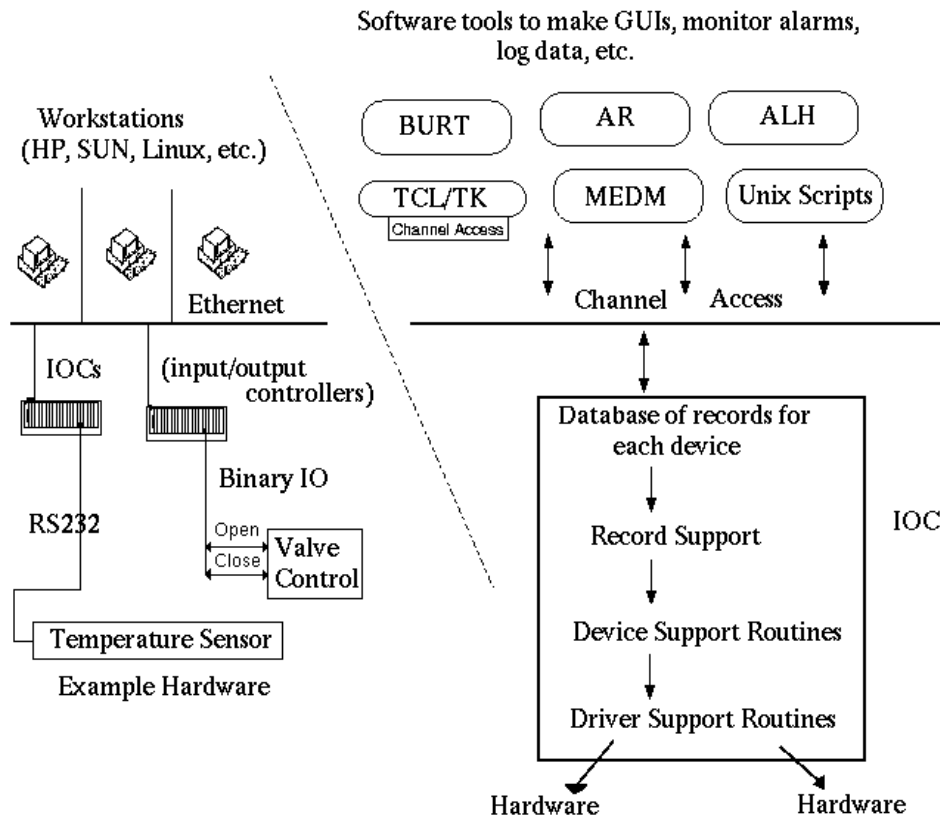
Figure 4.39: Architecture of Cryotarget Control System. Physical (Left) and Logical (Right) Architecture of a Control System developed in the EPICS environment.

Explicitly, the GUI communicates with a database which resides on the IOC. This database contains multiple records for each device to be controlled. Each of these records refers to a specific function a device is to perform, such as reading the output of a temperature sensor or setting the position of a valve. The database is watched by the record support. When a change or update of a hardware device is requested, the record support calls the device support routines necessary to query the hardware. Depending upon the complexity of the hardware, the device support may communicate directly with it or it may call a specialized drive support to do the communicating. This cycle continues over and over, for each change or update of a device's status.

4.9.3.2   EPICS

The control system development environment known as EPICS was used to develop the interfaces needed for remote control of the cryotarget hardware. EPICS is a collection of C codes and MOTIF programs that can be used to develop control systems. EPICS was originally developed by Los Alamos National Laboratory and Argonne National Laboratory, but now it is in use in more than 90 independent projects, including particle and nuclear physics, astronomy and industrial applications[89, 87].

4.9.3.3   Electronics

Much of the target's telemetry and controls evolved from experience with the Hall C target system. The Hall A cryotarget telemetry benefited from designed redundancy allowing the same parameter to be monitored by multiple sensors. This redundancy of sensor elements contributed to the overall reliability of the cryotarget performance.

A method to control the cryogens from the cryogen gas-panel was designed such that it could be done locally (at the panel) or remotely by computer. This flexibility was new and helpful when conducting major status changes in the target. Most of the electronics for the binary valve controls of the cryogen gas-panel and the J-T valve control and feedback was designed by the author. In addition, the author worked on the digital and serial communications between the IOC and a large number of the devices.

4.9.4 Cryotarget Operation and Performance

The HAPPEX noticeable parameters of the Cryotarget by which its performance was evaluated were the following; 1) Boiling, "Did boiling cause lower the density which increased pulse-pair fluctuations?", 2) Mechanical failures, "Did it break often?", "Was it easy to fix?", and 3) Ease of operation, "How much user/operator abuse could it withstand?" that is, "Was it 'touchy' to operate?".

Beam rastering is germane to the discussion on boiling and is addressed next.

4.9.4.1 Beam Rastering

The electron beam must be rastered to prevent damage to or boiling of the targets. The emittance of the electron beam is typically 2×10^{-9}m·rad. For a beam this small, at almost any luminosity, it will cut through most materials. This is prevented by reducing the beam-heat deposited in a given area. By rastering the beam, the heat-energy is spread over a larger area allowing for faster heat dissipation.

The beam is rastered by two sets of steering magnets 23 m upstream of the target. The steering magnets deflect the beam up to ± 500 mrad in X and Y. This translates to ± 2mm in X and Y on the target. For the first run of HAPPEX in 1998, the ratio of driving frequencies to the steering magnets was chosen for the raster to sweep out a rectangular pattern on the target, as shown in Fig. 4.40. The 1998 raster pattern resulted in edge-dwell-time where the beam lingered at the edges of the raster pattern. This resulted in a proportionally larger amount of heat deposition in the aluminum of the target windows of the shape of the edge of the raster pattern. At sufficiently high currents, cryogen boiling first appears at these edges.

To correct for this in the 1999 runs, the raster frequencies were chosen such that the raster swept out a circle, whose radius varied per unit time and whose center orbited on an epicycle. The resulting beam profile is shown in Fig. 4.41. The "hot spots" from this raster pattern were much less than those of the rectangular raster and eliminated boiling with the available beam current.

4.9.4.2 Boiling-Studies

Cryogen boiling can induce uncertainty in effective target thickness by fluctuations in cryogen density. Local cryogen boiling is largely a function of beam current per
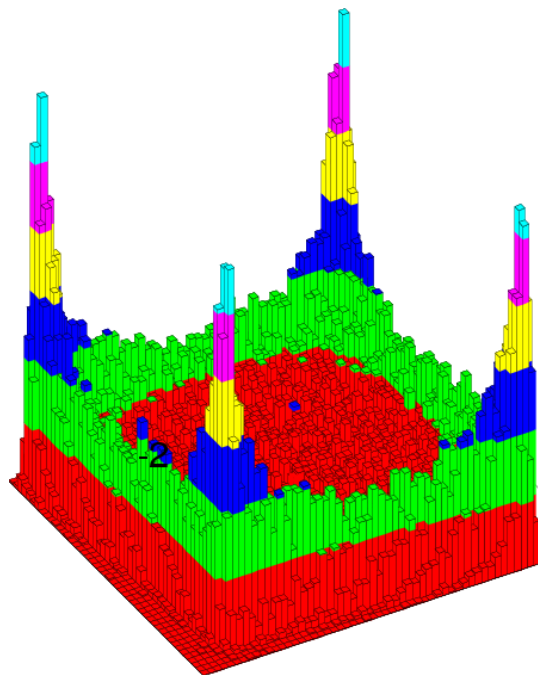
Figure 4.40: Beam Profile with Square Rastering. Dwell-time (vertical axis) is seen on the edges and corners of the pattern (1998 data).
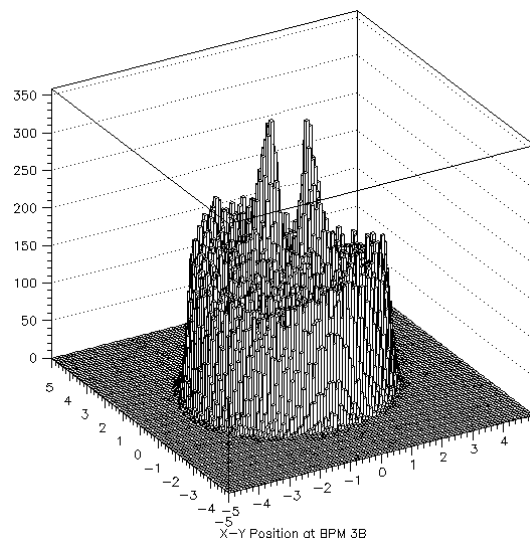

Figure 4.41: Beam Profile with Circular Raster. X and Y axes in mm and Dwelltime in arbitrary units on the vertical axis (1999 data).

unit area. Boiling studies were conducted to measure this dependence[90] [87]. For these tests, only the square raster was available and the raster size was maintained at ± 1.7mm by $\pm$ 1.4mm. The results are shown in Fig. 4.42. Most boiling occurs on the target-cell entry and exit windows due to raster dwell. Event drop-off at higher currents was largely eliminated with the circular raster.

The HAPPEX asymmetry is sensitive to fluctuations in target density, particularly if these fluctuations are correlated to beam-helicity. If not correlated, then target boiling merely reduces the cryogen density and hence, scattering-rate. This increases the statistical fluctuations in the measured pulse-pair asymmetries. Target boiling not correlated to helicity offers no complications other than the increase in statistical error.

Separate tests (at lower beam energy and thus higher cross section) carried out prior to the HAPPEX runs demonstrated that boiling of the liquid target did not significantly increase the noise in the asymmetry measurements. The study looked at fluctuations in the pulse-pair asymmetries versus beam current and raster size. High current (≈ 100 μAmps) and small raster size increased density-related fluctu-
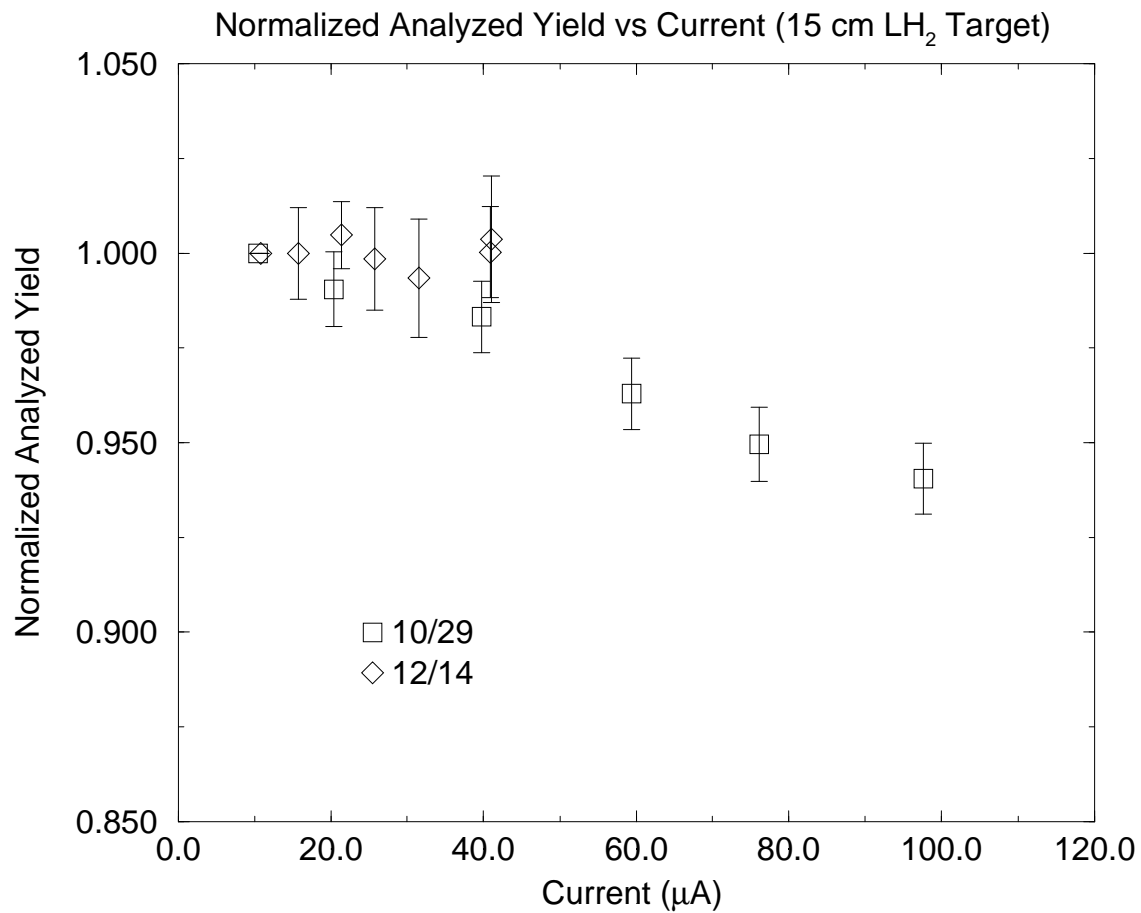
Figure 4.42: Number of Events (normalized to beam current) vs. beam current for the 15 cm lH$_2$ target. The event-rate drop off occurring above 40 μA shows a density drop in the H$_2$ which implies bubble formation. The data were taken on separate days in October and December 1997.
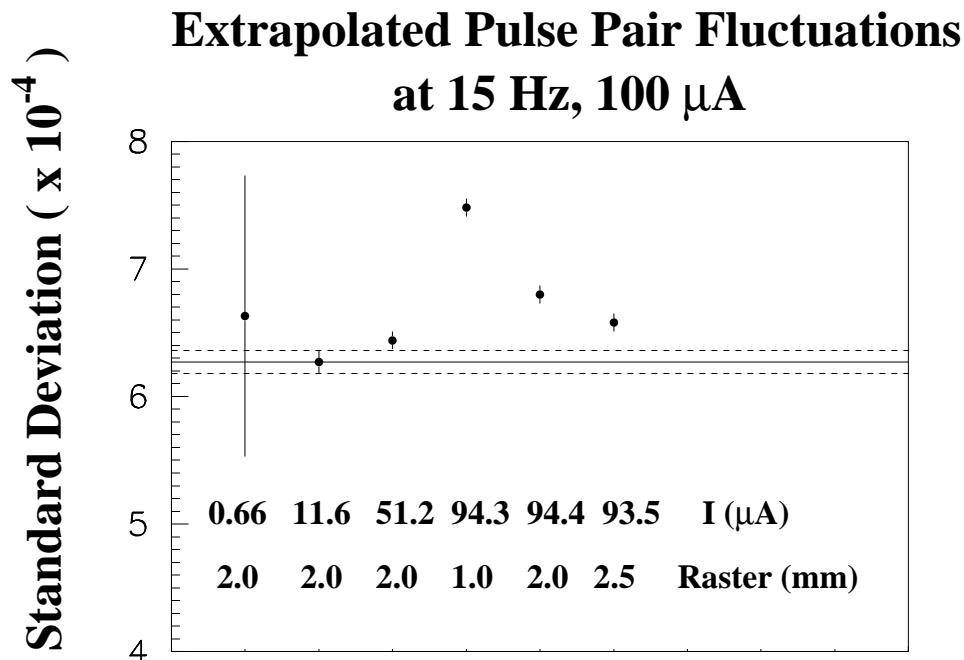
Figure 4.43: Pulse-Pair fluctuations vs. beam current and raster diameter. This data was take with the square raster.

ations from target boiling. High current and large raster size showed no significant fluctuations and thus no increase in pulse-pair asymmetry noise, as shown in Fig. 4.43. The typical raster sized maintained for HAPPEX runs was about ± 1.7mm by $\pm$ 1.4mm.

Another factor of cryotarget performance was its ease of use and stability. While the target system was composed of several complex systems, the control of these systems was well integrated in the EPICS software. The primary target operation consisted of raising or lowering the target position as the experiment required, matching the amount of coolant to the expected beam load, and dealing with the occasional emergency. With experience, matching coolant to beam-load became second hand. In the early stages of use and shakedown, the target system suffered lock-ups later determined were caused by firmware in the IOC. During these lock-ups, essentially there was no feedback to the finite state machine so temperature and heater corrections would not occur. During these periods, the practice was to

remotely reboot the IOC and while it rebooted, switch the heater controls over to manual which could then be adjusted from the counting house. Recall that the HP heaters were only needed when the beam dropped out suddenly, to prevent the target from over-cooling and freezing. As coolant from the ESR was 2 K warmer than the 13.8 K freezing point of lH_2, this was never a problem. Further it was noticed there was little temperature drift from the set point, provided the beam remained constant. Practice then evolved to simply rebooting the IOC when necessary. Upon recovery, the refreshed temperature readings would show a degree or so drift from the set-point of 19 K. The heater control would take over and the cryogen was soon at set point again. Elapsed time was roughly 2 minutes and this was the extent of the impact on most experiments.

Cool down was a simple procedure. The hydrogen and deuterium loops each had a 3800 liter expansion or 'blow-off' tank attached to the loop. The gas would be introduced into the loop and tank until a pressure of $\approx$48 psi was reached. The coolant valves would be opened to the corresponding loop and 15 K helium would be passed through the heat exchanger for that loop. The loop pressure would drop to $\approx$26 psi as the gas condensed into liquid and filled the target-cells, cell-block, and heat-exchanger. Cool down from room-temperature (300 K) to 19 K required less than 4 hours.

One feature designed into the system by way of the digital valve controls was remote 'boil-out' or 'blow-off' recovery. From time to time the coolant from the ESR would drop or cease due to ESR failures or power-failures. With no coolant, beam or no beam, the temperatures of the lH_2 and lD_2 would rise above the boiling point and the liquid in the cells would revert to gas. The expansion tanks absorb sudden pressure fluctuations if the liquid would boil suddenly or the system lost cooling power. In these circumstances the gas flows back through the gas-control-panel and fills the tank. This limited the pressure fluctuations well below the limits set on the safety-release valves. The system pressure would increase to $\approx$48 psia while the vent valves were set at 60 psia. In this fashion the gas, hydrogen or the more expensive deuterium, would not be lost.

When coolant was again available, it would be valved into the heat exchangers and the cryogen would be condensed back into liquid in the target cells. For cool down starting partially cooled, as with an area-wide power-failure, recovery would usually take less than 1/2 hour. Charging or changing cryogen gas in the system or

loops was similar. The cryogen loop of choice would be warmed up, the gas vented outside, new gas charged into the system and liquefied. This allowed further system adaptability as primary warm-up and cool-down and blow-off or boil recovery could be done entirely remotely. This allowed target system recovery from minor events while Hall A remained in Beam Permit, thus shortening the down time.

The only hard limitation on target performance was the ESR cooling power. The ESR could provide at best, 28 g/s mass flow of 15 K helium coolant. A fault protection was set to limit this flow rate to 25 g/s. The coolant temperature would also vary between 13 K and 20 K. The cooling ability of the helium gas was not linear with its temperature. Depending upon ESR temperature, 25 g/s mass flow could provide up to $\approx$ 625 W of cooling to the target cell. As mentioned in sec. 4.9.1, this would equal 125 μA of beam current. In principle, with only one target system running, that target could take all of the ESR's mass flow and thus handle upwards of 125 μA of beam. In practice, however, the ESR mass flow was shared between the Hall A cryotarget and the Hall C cryotarget which effectively limited the combined target beam currents to 125 μA.

4.10 Data Acquisition

HAPPEX used two data acquisition systems (DAQ). The data necessary for computing kinematics such as detector position and Q^2 were gathered with the CODA (CEBAF Online Data Acquisition) system. The asymmetry data were taken with a DAQ system custom designed and built for HAPPEX to minimize electronic noise, cross-talk and helicity-correlated systematics.

4.10.0.3 CODA

CODA[91](CEBAF Online Data Acquisition) system, is a toolkit developed by the Data Acquisition Group at Jefferson Lab. CODA is a layered and expandable software and control system which can be configured on-the-fly to accommodate new combinations of electronic devices. Data acquired by CODA was written to a local computer disk and copied at specified times to the Mass Storage System (MSS) in the JLab Computer Center where it is archived on data tapes. The Standard DAQ used for HAPPEX is displayed in Figure 4.44.
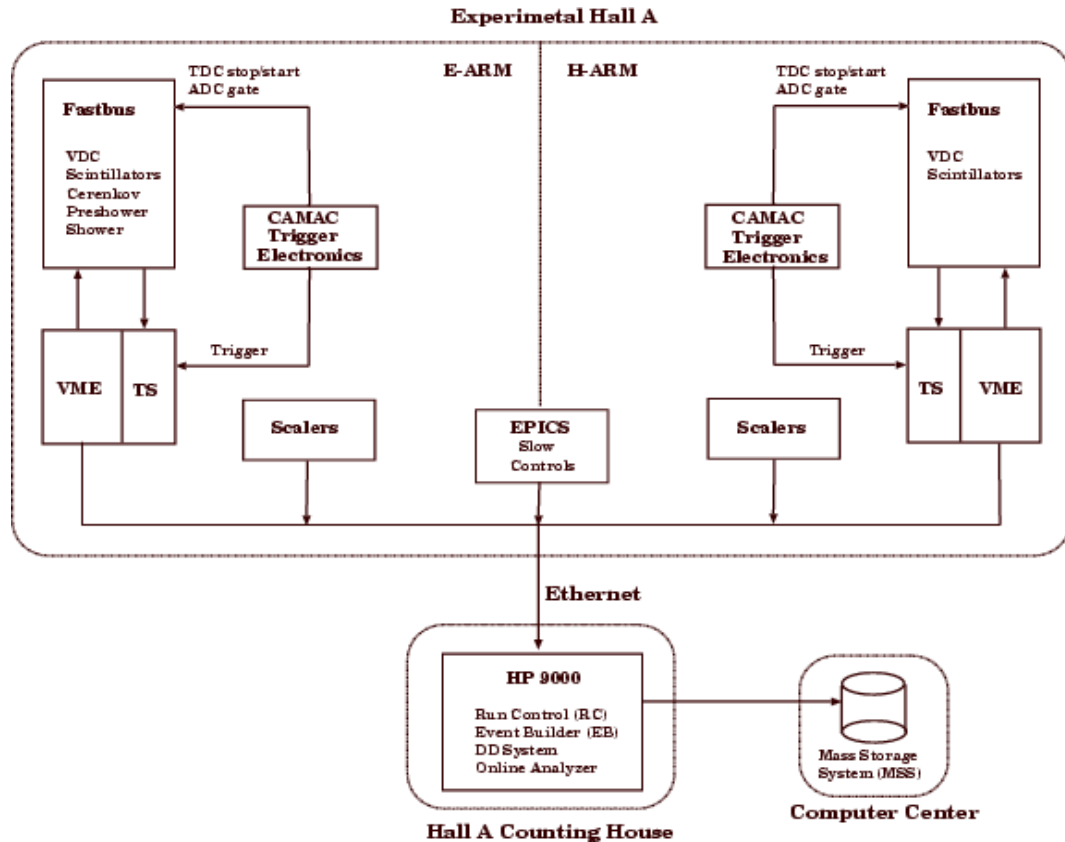
Figure 4.44: Schematic of standard Hall A data acquisition system.

4.10.1 Standard DAQ

4.10.1.1 Hardware

For each spectrometer, there was one VME crate, one Fastbus crate and one Trigger Supervisor (TS) located inside the spectrometer shielding house. Fastbus electronics provide higher data acquisition rates than CAMAC systems. The Fastbus crate housed all Time to Digital Converters (TDC), which were LeCroy model 1877 TDCs operating in common-stop mode with 0.5 ns resolution, for the VDCs. Also housed were LeCroy model 1875 TDCs operating in common-start mode with 0.1 ns resolution, for the scintillators and trigger diagnostics. Included in the Fastbus crate were the Analogue to Digital Converters(ADC), specifically LeCroy model 1881M ADCs for analog signals from the scintillators and HAPPEX detectors.

The Fastbus and VME crates (which were located in the counting-house) also housed single board computers called the Read Out Controllers (ROC). The ROCs

interfaced the detector system electronics with the DAQ computer running CODA. CODA uses commercially available VxWorks software to communicate with the ROC.

4.10.1.2   Operation

When particles passed through the detector package in either the Electron or Hadron spectrometer, they generated signals in the scintillators or the HAPPEX detectors. If the pattern of detector signal was recognized by the trigger electronics as an allowed type, the Trigger Supervisor (TS) caused the event to be recorded by the data acquisition. The allowed types of triggers for HAPPEX were those signals which qualified above a 40mV threshold setting. First the ROCs were read out. The fragments of information from the ROCs were collected by the Event Builder (EB) process and assembled by CODA into the CODA event format including header and identifying information. After the event was built and assembled, CODA handled the writing of the event file to disk. Once on disk, the data file was available for writing to tape or for preliminary reduction with ESPACE (Event Scanning Program for Hall A Collaboration Experiments, see section 5.1.1).

4.10.2   HAPPEX DAQ

To control systematics caused by electronic cross-talk and ground loops, a custom designed DAQ system was constructed for HAPPEX[75, 92].

The HAPPEX DAQ system has two parts. The first part, known as the HAPPEX DAQ (Fig.4.45) is located in the Hall A counting-house where all connections and controls could be monitored.

The second part of the DAQ (Fig. 4.8) is located in the injector-building and houses the Injector DAQ. All communications between the HAPPEX and Injector DAQs were carried on fiber-optic lines to avoid electronic cross-talk.

When asymmetry data was being taken, a control switch in the counting house would remotely switch the PMT signal from the Standard DAQ system to the HAPPEX system. This was the normal running condition. The elements of the HAPPEX DAQ are described in the following sections.
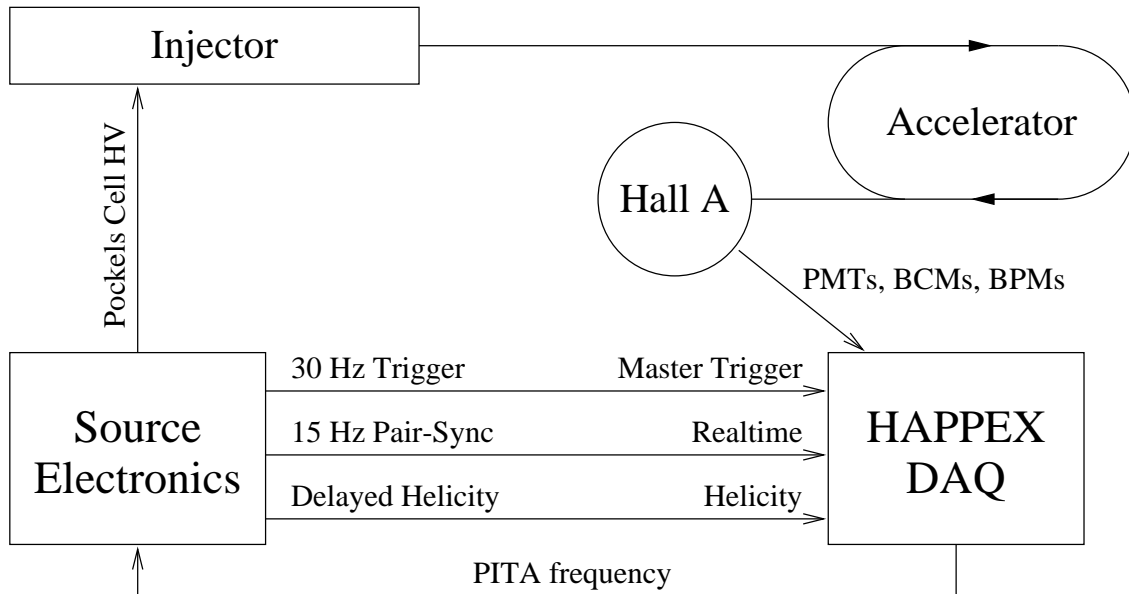
Figure 4.45: Schematic of HAPPEX DAQ system.

4.10.2.1 VME Crate

The HAPPEX VME crate in the counting-house contained the VME computer, VME trigger interface, scaler, and ADC boards.

VME Computer

The VME computer was an MVE-162 controller card with an embedded Motorola 68000 series microprocessor running the VxWorks operating system. The VME computer collected data from the VME trigger interface, scaler, and ADC boards and sent the data via ethernet to a Hewlett Packard workstation running CODA version 1.4.

VME Trigger Interface

The VME Trigger Interface (version 1) was designed as a way for the VME computer to communicate with non-VME electronics through various input and output bits. The *VME trigger*, *delayed helicity*, and *realtime* signals were sent into the VME Trigger Interface so that they could be read by the VME computer. The VME computer also programed the PITA DAC through the output bits of the VME Trigger Interface. The VME Trigger Interface has a 34-pin I/O port which was

connected via ribbon cable to the VME Transceiver board inside the helicity control box. Logic level translators on the VME Transceiver board allowed the VME Trigger Interface (which uses ECL logic) to talk with the electronics (which use TTL logic).

Scaler

The scaler scaled the *master trigger* signal from the Source Electronics and thereby counted helicity windows. The scaler was read each time the VME computer received a trigger and was used to monitor for dead time.

ADC Boards

The ADC boards were custom-built at Harvard University. They are designed to integrate essentially-DC signals for times on the order of ten milliseconds. The heart of each ADC channel was an AD7884 16-bit analog-to-digital converter chip which digitized the integrated signal. Each ADC board had four channels.

A special feature of the board was the ability to add a pseudo-random analog voltage offset to the integrated signal prior to digitization using an onboard DAC (not the same as the PITA DAC!). This pseudo-random voltage offset was referred to as "DAC noise". The transfer function between DAC input and ADC output could be calibrated off-line and used to subtract the contribution due to 'DAC noise' from the digitized output. This technique drastically reduced the differential nonlinearity of the ADC.

The ADC boards can integrate either current or voltage inputs by minor board modifications. HAPPEX used current-integrating boards for the detector PMT signals and voltage-integrating boards for BCM and BPM signals. The input signals were fed through BNC-style twinax connectors. The digitized outputs and DAC values were read by the VME computer across the VME backplane. The ADC boards required external timing signals to set the integration period. There were four timing signals, *Baseline*, *Peak*, *Convert-Start*, and *Reset*, which were input through a 10-pin ribbon connector. They were provided by the ADC Timing Board, described in Section 4.10.2.2 below.

Upon release of *Reset*, the ADC input signal was integrated onto the feedback capacitor of an op-amp. Since the input signal was essentially DC, the integrator's output was essentially a smooth ramp. The ramp was sampled at two points, deter-
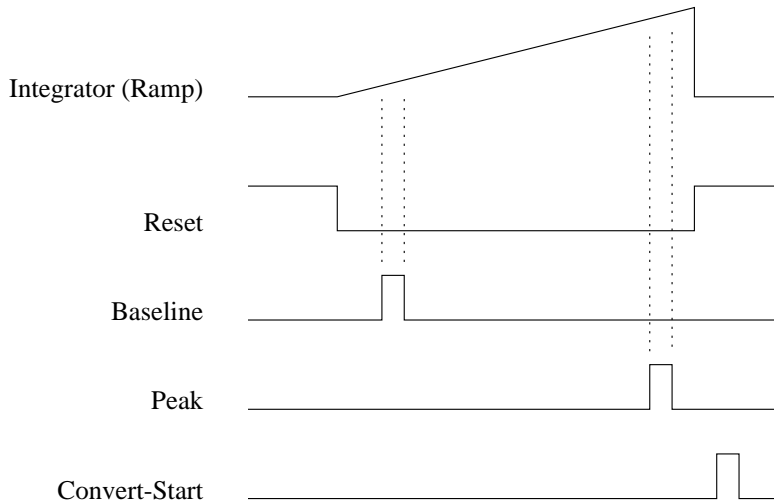
Figure 4.46: ADC timing signals.

mined by *Baseline* and *Peak*, and the difference between them was fed to a summing amplifier which added in the DAC offset and presented the resulting signal to the input of the AD7884. Thus the separation between *Baseline* and *Peak* determined the integration time. After the *Peak* sample has been acquired, *Reset* was asserted once again to clear the integrator. The AD7884 digitized the signal at the rising edge of *Convert-Start* to complete the integration cycle.

4.10.2.2 Helicity Control Box

The helicity control box housed the ADC timing board, VME transceiver board, and trigger generator board. The trigger generator board was for test systems and was not used in the HAPPEX run.

ADC Timing Board

The ADC timing board provided the external timing signals required by the ADC boards. Upon receipt of the *master trigger* signal from the source electronics indicating the start of a new helicity window, the ADC timing board waits a suitable amount of time for the beam polarization to stabilize (around 200 μs) and then generates four timing signals: *Baseline, Peak, Convert-Start*, and *Reset*, all carried on the ADC ribbon cable. These signals are shown in Figure 4.46 and are described in Section 4.10.2.1 above. A fifth signal, *VME Trigger*, was also generated by the timing board. It comes about 5 μs after *Convert-Start* and was sent to the VME

Trigger Interface by way of the VME transceiver board. This signal lets the VME computer know that there is valid ADC data to be read.

VME Transceiver Board

The VME transceiver board has two main functions: logic level translation and generation of the PITA frequency.

The *delayed helicity*, *realtime*, and *VME Trigger* signals were fed through the VME transceiver board on their way to the VME Trigger Interface. The signals were optically isolated at their inputs in order to prevent ground loops which might couple the helicity signal into the ADC measurements, although use of the delayed helicity instead of the actual helicity probably made this feature unnecessary. After passing through the opto-isolators the signals were converted to ECL and sent on to the VME Trigger Interface.

The VME transceiver board also contained the PITA DAC, voltage-to-frequency converter, and fiber-optic transmitter. The DAC set-point (reflecting the desired PITA offset) was sent by the VME computer through the VME Trigger Interface to a 12-bit DAC on the VME transceiver board. A V-to-F chip converted the 0-10 V output of the DAC to a 0-100 kHz square wave. This square wave drove a fiber-optic transmitter which sent the PITA frequency to the source electronics via optical fiber (see Fig 4.45).

'The fundamental principle of science, the
definition almost, is this: "the sole test of the
validity of any idea is experiment."'

– Richard P. Feynman

Chapter 5

Analysis

Calculation of the physics asymmetry, A^{pv}, was accomplished with two analysis
programs dictated by the design needs of the experiment.

The pulse-pair asymmetry was calculated with a HAPPEX-specific analysis pro-
gram called Anpar. Anpar is a Fortran program which read the data from a .hbook
file provided by the HAPPEX DAQ, applied cuts as specified, and decrypted the
helicity information to assign event windows to left or right helicity states.

The kinematic information which provides information on backgrounds, Q^2,
alignment and performance of the detectors, and target performance was extracted
using the analyzer ESPACE.

The basic elements of the asymmetry calculation are to:

- Calculate the raw asymmetry from the pulse-pairs.

- Measure and correct helicity-correlated systematic asymmetry contributions
  of the beam transport system to the raw asymmetry.

- Measure and calculate the Q^2 of the $H(\vec{e}, e')$ reaction.

- Combine polarimetry and beam energy measurements.

- Calculate the corrected asymmetry and its error.

5.1 Kinematic Analysis

5.1.1 ESPACE

The data analysis code for Hall A is the Event Scanning Program for hall A Collaboration Experiments (ESPACE)[93]. It was adapted from an event analyzer developed in MAINZ by E. Offerman. ESPACE is fairly flexible and can be used for direct analysis or as preliminary data reduction for other analysis programs. ESPACE reads events in the CODA format and decodes them. During this process it can:

- Generate N-dimensional ntuples and fill histograms of any raw detector TDC or ADC signals or perform analysis and reporting of relevant signal information.

- Reduce VDC information to calculate focal plane positions and trajectories $(x_{fp}, y_{fp}, \theta_{fp}, \phi_{fp})$.

- Perform particle traceback, using the HRS optics database, to calculate the target vertex $(\theta_{tg}, \phi_{tg}, y_{tg})$.

- Provide conditional cuts for spectra analysis and event reconstruction.

5.2 Q^2

At the moderate energies used to resolve the nucleon's complicated interior, on the order of 500 $(\text{MeV/c})^2$, target recoil can not be neglected. To calculate the momentum transfer we must use the Lorentz-invariant four momentum of the electron scattered through angle θ with incident momentum, $\mathbf{p}_0$ and final momentum, $\boldsymbol{p'}$. Neglecting the electron's mass $(m_e^2 \ll Q^2)$ the momentum transfer, Q^2 is then [3]:

$$Q^2 = (\mathbf{p}_0 - \mathbf{p}')^2 - (E_0 - E')^2 = -2m_e^2 - 2pp_0\cos\theta + 2EE_0$$

$$= 2pp_0(1 - \cos\theta) = 4pp_0\sin^2\frac{\theta}{2}. \tag{5.1}$$

Q^2 is a critical element for the interpretation of the physics asymmetry. The asymmetry, A_{th} is inherently a function of Q^2 as is shown in Eqn. 3.35, where all form factors are functions of Q^2. While the calculation of Q^2 is simple, accounting for the systematic errors of the ingredients which go into Q^2 is more involved. The analysis of the systematic errors generally involves understanding how the kinematic

elements are seen and interpreted by the various detectors, electronics and analysis packages.

5.2.1   Ingredients of Q^2

During the 1999 runs, the incident energy was measured via the Hall A ARC and the 'EP' apparatus. The EP was designed for the E93-050 experiment[94] and uses elastic scattering off of 30μm tape of CH_2. The arc measurement uses the beam entrance and exit angles of the hall A beam-line curve. Both the EP and the arc methods have an energy acceptance from 0.5 GeV to 6 GeV and an absolute energy resolution of $\delta p/p \leq 2 \times 10^{-4}$. The incident energy of the 1998 run was initially determined by the accelerator group. In considering the systematics below, it became apparent that the 1998 energy needed to be adjusted by -8 MeV (-0.2%) to make certain kinematic variables consistent, as described below.

The second ingredient for determining Q^2 is the scattered energy, E', as measured by the spectrometers. It was originally expected that the spectrometer's resolution of $\Delta P/P < 4 \times 10^{-4}$ would contribute negligible error. It was found necessary, however, to adjust the momentum scale of the spectrometers by a few tenths of a percent in order to satisfy the missing mass constraint for elastic scattering. The spectrometer magnet constants we obtained agreed to within 0.1% of values recently attained from an independent study[95].

The third ingredient is the scattering angle. The angle determination has two parts:

1) ESPACE is used to reconstruct horizontal and vertical angles at the target where these angles are relative to the spectrometer's optic axis. In order to calibrate the ESPACE angle reconstruction, 'sieve-slit' runs are done as will be explained below. Information on the sieve-slits are provided by optical survey.

2) The angle of the spectrometers optic axis must be known relative to the incoming beam. This information is also provided by optical survey.

Finally, the Q^2 values must be weighted by the ADC pulse heights of the HAPPEX detector signals. This is addressed below.

The beam energy, E_0, must be corrected for losses while the electron transits the target. The correction gives the incident energy as

$$E = E_0 - \frac{dE}{dz}dz \qquad (5.2)$$

where E_o is the beam energy provided by the accelerator group in 1998 or provided by the e-P and ARC measurements in 1999, dE/dz is the energy deposited in liquid hydrogen per unit length; $dE/dz = 0.029245\,GeV/m$. dz is the depth into the target that the event occurs. This is computed with ESPACE using

$$dz = \frac{-(\text{Target\_exit\_window}) - \text{spec\_e.y\_tg}}{\sin\theta} \qquad (5.3)$$

where θ is calculated by ESPACE as

$$\theta = A\cos\left[\frac{\cos\theta_{\text{survey}} - \phi_{tg}\sin\theta_{\text{survey}}}{\sqrt{1 + \phi_{tg}^2 + \theta_{tg}^2}}\right] \text{ [93, 96]} \qquad (5.4)$$

and Target_exit_window, spec_e.y_tg, ϕ_{tg}, θ_{tg} are variables defined in ESPACE and θ_{survey} is provided by the JLab survey team. The electron's scattered energy, E' is a calculated ESPACE variable.

5.2.2 Q^2 Weighting

The Asymmetry measurement is biased by the signal strength of the detectors. Due to geometric and bulk light attenuation in the detectors, the signal strength is proportional to the distance from the PMT where the electron enters the detector. Lower energy electrons transit the detector further from the PMT and deposit less energy in the detector. Also the Čerenkov light is attenuated as it travels to the PMT. Both conspire to lower the ADC signal and this biases Q^2 towards higher (apparent) momentum. As the interpretation of the asymmetry relies on Q^2 dependent form factors, this bias will shift the A_{th}. To correct for this, the Q^2 values are weighted by the ADC pulse heights according to $Q^2 = \left(\sum Q_i^2 A_i\right) / \left(\sum A_i\right)$ where A_i are the ADC amplitudes in bin i and and Q_i^2 is the corresponding measurement. This weighting shifts the central Q^2 by (-0.38±0.05)%. Some typical Q^2 distributions, without weighting, are shown in figure 5.1. The top two plots are from 1998 data, electron and hadron arm respectively. 1999 Part I data is shown in the middle plots and 1999 part II is shown on the bottom. The difference between the shapes of these distributions are discussed below, especially in section 5.2.3.6
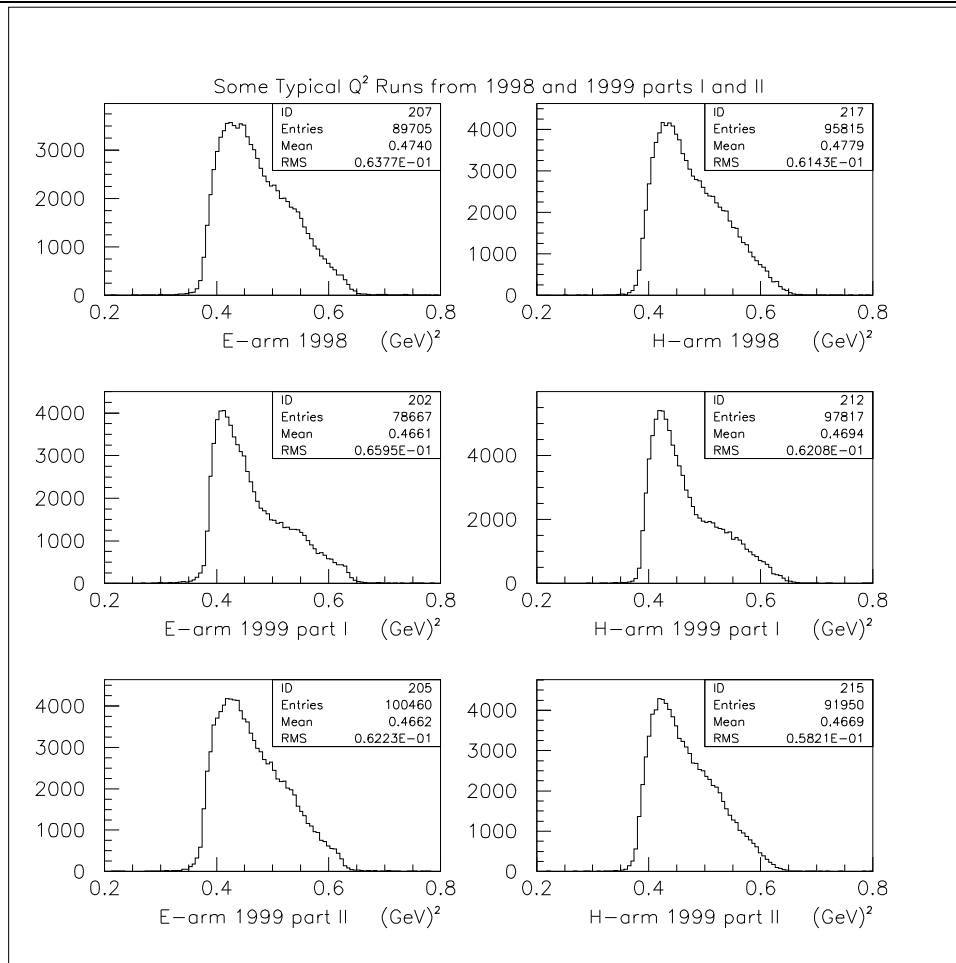
Figure 5.1: Typical Q^2 measurements from 1998(top), 1999 part I (middle) and 1999 part II (lower).

5.2.3   Systematic Errors

The mechanisms involved with the measurement of the Q^2 variables are analyzed here.

The VDCs are used exclusively for the angle and momentum reconstruction. As such, VDC efficiency and trigger timing may be of critical importance for the Q^2 calculation. As will be discussed in the following section, these factors contributed negligible errors to Q^2.

5.2.3.1   Time calibrations and VDC efficiency

The momentum calculation and angle reconstruction which rely on the VDCs are functions of the VDC performance. Contributions come from T_0 (the timing off-

set), the track-fit (measured by χ^2), and the VDC reconstruction efficiency. By determining $\partial\chi^2/\partial T_0$, $\partial\epsilon/\partial T_0$, and

$\partial Q^2/\partial T_0$ the effects of the VDC track reconstruction on Q^2 can be seen.

The timing offset, T_0 can be varied in ESPACE during initial data processing. By varying T_0 by several nanoseconds, effects on the tracking efficiency, the χ^2 of the track fit, and the effect on Q^2 were observed. When T_0 is adjusted to minimize χ^2, the shift in Q^2 is negligible. The effects of varying T_0 are shown in Fig. 5.2.
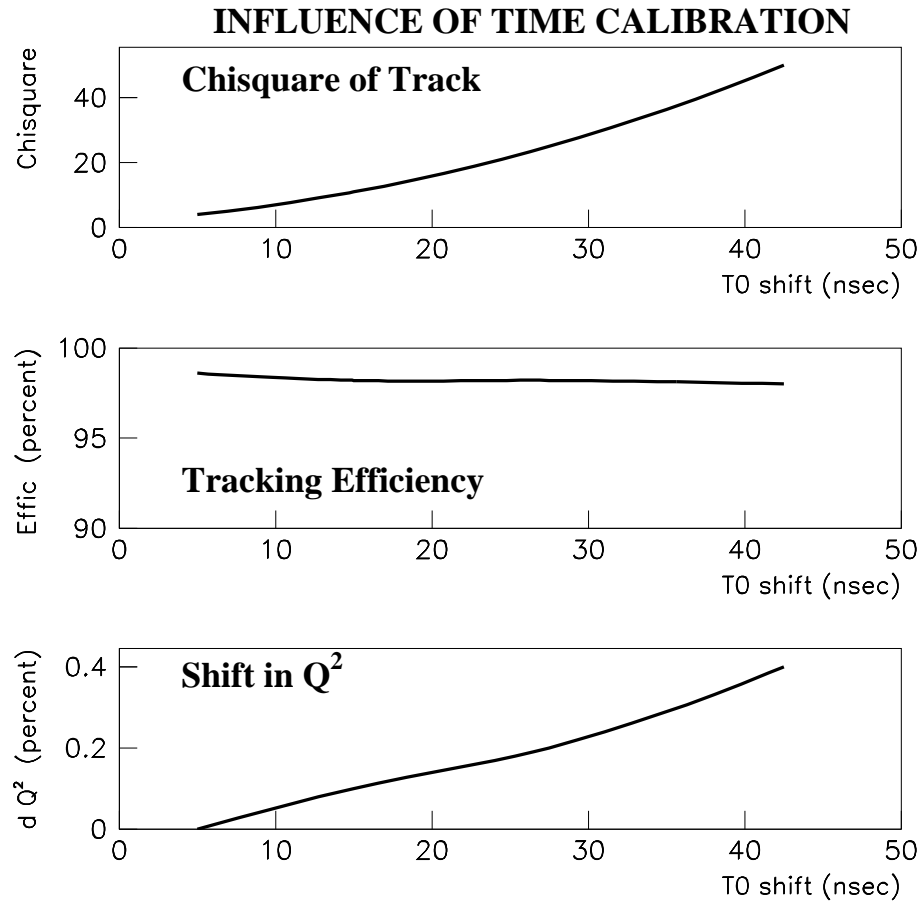

Figure 5.2: Q^2 response to T_0 indicate that large shifts in the trigger timing result in small deviations in Q^2.

Redundant Q^2 determination

For elastic scattering the variables E, E', and θ are not independent [1] and we may eliminate one in favor of the other two to provide consistency checks on the

determination of Q^2. The different methods for calculating Q_i^2 are

$$Q_1^2 = 2EE'(1 - \cos\theta) \quad \text{(uses all variables)} \tag{5.5}$$

$$Q_2^2 = 2E^2 f_r(1 - \cos\theta) \quad \text{(independent of } E') \tag{5.6}$$

$$Q_3^2 = 2E'^2 f_r'(1 - \cos\theta) \quad \text{(independent of } E) \tag{5.7}$$

$$Q_4^2 = 2Mc^2(E - E') \quad \text{(independent of } \theta) \tag{5.8}$$

where f_r and f_r' are recoil factors defined by $f_r = (1 + \frac{E}{Mc^2}(1 - \cos\theta))^{-1}$ and $f_r' = (1 - \frac{E'}{Mc^2}(1 - \cos\theta))^{-1}$ and M is the mass of the proton.

5.2.3.2 Spectrometer Surveys

Some systematic error in the event-angle reconstruction, and thus in Q^2, is contributed from the spectrometer surveys. These surveys determine the pointing of the central optic axis of the spectrometers and are then used to calibrate other spectrometer attributes.

There are three primary contributions to survey error.

First, there is a variation in the spectrometer 'mis-pointing' or 'off-set'. This is the alignment of the spectrometer central optic angle with respect to the target center (Fig. 5.3). This contributes about ±0.5 mrad to the angle calibration. The second is a ±0.3 mrad variation in the spectrometer-beam angle. The third is an ≈ ±0.5 mm variation in the position of the sieve-slit collimator relative to the optic axis. The sieve-slit is used to calibrate the reconstruction angles to that of the central optic axis.

It is not known if these variations are due to movement in the spectrometer system or are due to reproducibility errors in the survey. The time frame for these variations is large. The ±0.5 mm variation in sieve-slit location was observed over a three year period.

The combined error from the total spectrometer survey is 0.8 mrad[1] added in quadrature. Table 5.1 shows survey results from 1998 and 1999.

5.2.3.3 Angle Reconstruction

The primary source of error in Q^2 calculation is the event-angle reconstruction. Using equations 5.5, 5.6, or 5.7 and the half-angle relation for sine and cosine we

---

[1]Sieve offset / distance to collimator = 0.5 mm/1109 mm = 4.5 mrad
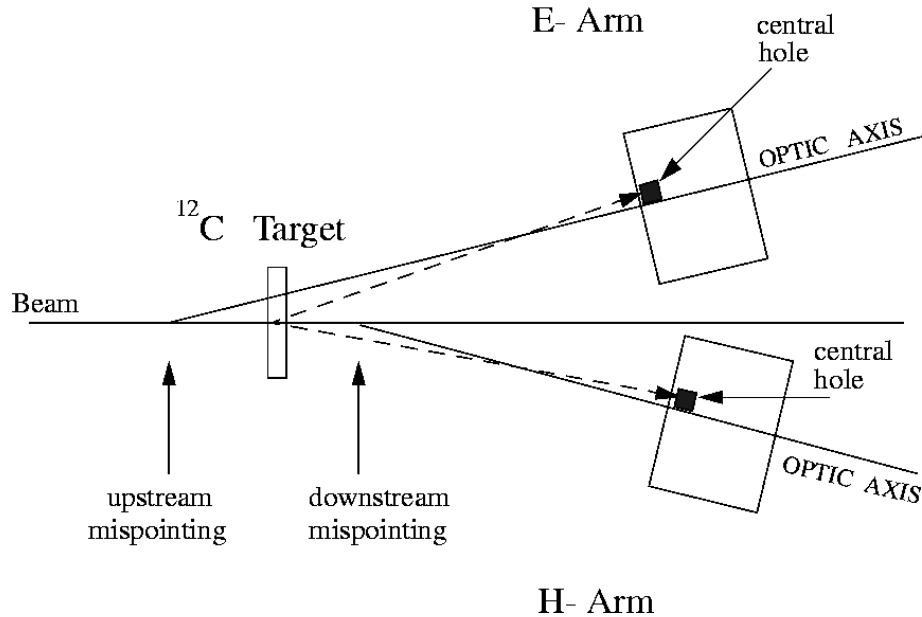
Sieve Slit Setup

Figure 5.3: Sieve-slit setup for the calibration of the angle reconstruction. The surveys give the angle of the optic axis relative to the beam direction and the "mispointing error" which is the distance along the beam axis from the center of the target to where the optic axis intersects the beam.

have (for small angles) an estimate of the uncertainty.

$$\delta Q^2 / Q^2 \approx 2\delta\theta/\theta \qquad (5.9)$$

Taking the total uncertainty in angle $\delta\theta$ to be ≈ 1 mrad and $\theta = 218.6$ mrad this gives a rough estimate of the uncertainty in Q^2 due to the error in angle to be $2 \times 1/218.6 = 0.91\%$. A detailed list of error contributions to Q^2 is shown in Table 5.3.

The angle reconstruction was checked with 'sieve-slit' runs. This is a comparison of the spectrometer optics database used by ESPACE with the optical surveys of the spectrometers and the sieve-slits.

The sieve runs were done with a thin solid carbon target which uniformly illuminated the spectrometer focal plane with events. Using the sieve-slits, and knowing their mechanical attributes and distance from the scattering center, one can calculate the relative angle of the scattering event and compare this to the ESPACE

Date		Electron arm		Hadron arm	
		Angle (degrees)	Mispointing (mm upstream)	Angle (degrees)	Mispointing (mm downstream)
May 1	1998	12.529	1.85	12.558	3.07
April 5-7	1999	12.527	1.11	12.561	2.83
April 28	1999	12.527	0.95	12.564	3.28
June 1-2	1999	12.526	1.26	12.563	3.23
July 20-21	1999	12.527	0.92	12.560	2.64

Table 5.1: Survey data from 1998 and 1999 HAPPEX Runs.

calculated event angle [97]. This information can then be used to calibrate the optics database. Spectra from sieve-slit data and the sieve-slit mechanical attributes are shown in Figs. 5.4 and 5.4 respectively.

Since 1998 we were given three optics databases which we were told had good kinematic reconstruction [98, 95, 99]. They were "db vcs new 10", "db opt tc4", and "db cebaf 3.0". In principle, using these databases, comparisons of the ESPACE kinematic reconstruction of the sieve-slit data should give angle measurements consistent with the survey calculated location of the sieve-slits. The scribe marks in Fig. 5.4 show the expected location of the central holes based on the survey data. The database "db cebaf 3.0" was used with the 1999 data and required an angle adjustment of ≈ 1 mrad for both spectrometers. The reconstructed sieve data shown is *after* adjustment. For the 1998 data, only the hadron arm needed adjustment. In practice, the reconstructed horizontal angle adjustment varied ± 0.3 mrad between the databases.

5.2.3.4   Beam Energy Measurements

Information on beam energy is required for the calculation of the momentum transfer in electron-nucleon scattering experiments. All terms of the HAPPEX asymmetry calculation are functions of Q^2, and as such, the beam energy and errors in its determination figure into the final parity-violating asymmetry, A^{PV}.

For the 1998 run a beam energy of 3.358 GeV $\pm$ 0.15% ((3358 ± 5) MeV) was provided by the accelerator control group. This method suffered from systematic errors which, when later corrected for, lowered the reported beam energy by 8 MeV. This is discussed in section 5.2.3.5.
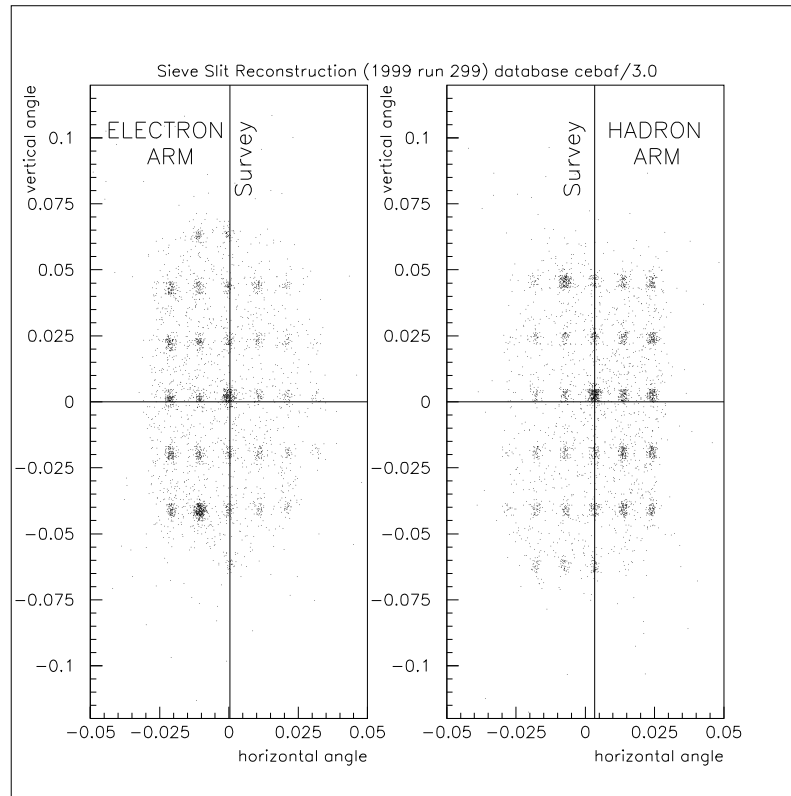
Figure 5.4: Sieve-slit data. These spectra were calculated with ESPACE using the optics database 'cebaf_3.0'. The vertical and horizontal axis are in radians.
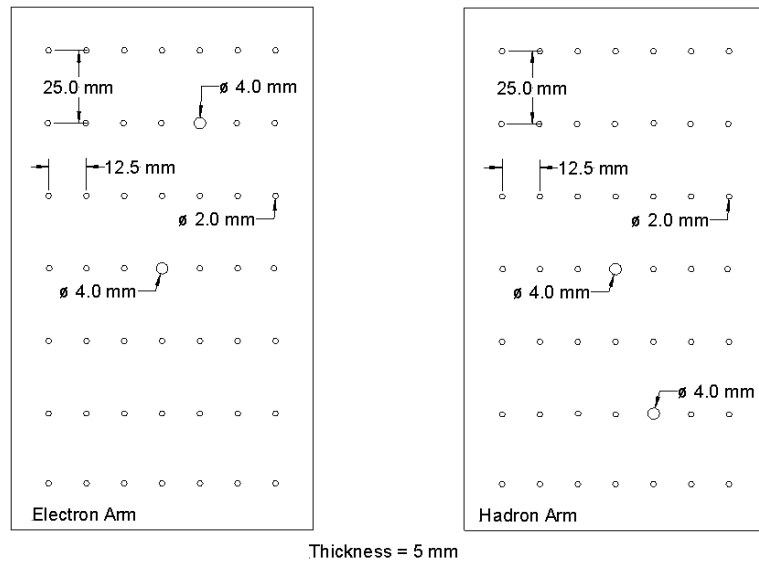

Figure 5.5: Sieve Slit geometry and mechanical attributes.

In the 1999 I and 1999 II runs, the beam energy was measured by two independent devices, the "e,p" and the "ARC". Both methods are accurate to better than 1 MeV.

The "e,p" beam energy measurement is determined by an independent measurement of the scattered electron angle, θ_e and the recoil proton angle in the ^{1}H(e,e'p) elastic reaction. The "e,p" measurement is made with a dedicated device located 17 m upstream from the target in Hall A. The "e,p" device has two identical arms, each consisting of an electron and a corresponding proton detector system made up of a set of 2×8 silicon strip detectors in the reaction plane. These strip detectors are placed symmetrically with respect to the beam along the vertical plane. Making simultaneous measurements with both arms cancels, to first order, uncertainties arising from the knowledge of the beam's position and direction. The target is a 13 μm thick rotating tape of $(CH_2)^n$. There are two main sources of systematic error for this device. The first is uncertainty in target position along the beam axis ($\pm 10\mu$m typically). This translates into error in the angle calculation necessary for the kinematics. of this reaction. The second is uncertainty in the detector positions ($\pm 15\mu$m typically). The expected resolution of this device is $\Delta E/E \sim 1.5 \times 10^{-4}$.

The Hall A "ARC", is a 40 m bending section of the Hall A beamline from the beam switch-yard into Hall A. The Arc method uses the 8 dipole and 9 quadrupole magnets of the beam line along this section as a spectrometer. By turning off the quadrupoles, the dipoles make the 34.3° bend of the ARC dispersive, and the beam energy is related to the field integral of the dipoles (along the path of the beam) and the arc angle, θ_{ARC} through which the beam is bent. The dipoles were designed to provide a constant field integral over most of the available dispersive beam path so the field integral remains a well defined quantity. The method requires simultaneous measurement of the magnetic field in the bending elements (provided by a reference magnet - 9$^{\mathrm{th}}$ dipole) and the actual bend angle for the arc, provided by set of wire scanners. One pair of wire scanners locates the beam center as it enters the arc, another pair locates the center as the beam exits the arc. A $\pm 15\mu$m position accuracy is typical for the scan wires. This technique requires a beam position stability better than 15μm. The expected resolution for this device is $\Delta E/E \sim 6.8 \times 10^{-5}$.

5.2.3.5 Momentum Adjustments

As a check on the ESPACE reconstruction of the kinematic variables, Eqn. 5.8 may be re-written in terms of missing-mass squared:

$$dm^2 = 2\text{M} \left(E - E'\right) - Q^2 \qquad (5.10)$$

This quantity should be identically zero but in fact (as initially calculated) deviated by $\pm 0.08 (\text{GeV/c})^2$. This deviation indicated a systematic shift in one or more of the variables. This shift can be accounted for if 1) the beam energy E, was off by 10 MeV, 2) The reconstructed momentum E', was off by 10 MeV (ESPACE), or 3) Q^2 was wrong by 4%. Note that an angle shift of ≈ 1 mrad cannot explain a 4% shift in Q^2.

We assumed for the 1999 run, that the beam energy was measured with sufficient accuracy and therefore we needed to adjust the spectrometer momentum scale in the database "db cebaf 3.0". For this database we decreased the Electron-arm momentum by 0.6% and increased the Hadron-arm momentum by 0.2%. Fig. 5.7 shows the shifts in missing mass squared as a percentage of Q^2 before and after this momentum scaling. By adjusting the momentum scales in "db cebaf 3.0", dm^2 for the 1999 data was made consistent with zero. If we then use this database to calculate missing mass from the 1998 data, the same momentum corrections must be used. The only variable left to adjust was the beam energy. In adjusting the 1998 beam energy to make the 1998 dm^2 consistent with zero, we found the 1998 beam energy was 8 MeV lower than was reported. The results are shown in Fig. 5.7. Figure 5.6 shows representative missing mass plots of the 1999 and 1998 data after these corrections. The peaks are reasonably centered at zero. These adjustments to the spectrometer momentum constant was later confirmed in a separate, independent study (see Appendix B).

For consistency, this procedure was applied to all three databases, with consistent results. In summary, using missing mass as a constraint on the kinematic variables we 1) corrected the angle reconstruction in each database using the sieve-slit data, 2) we assumed the 1999 arc and e-p measurements of beam energy to be correct, 3) adjusted the spectrometer constants in the databases to scale the missing mass to zero, and lastly 4) corrected the 1998 reported beam energy to scale the 1998 missing mass to zero. If correct, this procedure should give the same results for
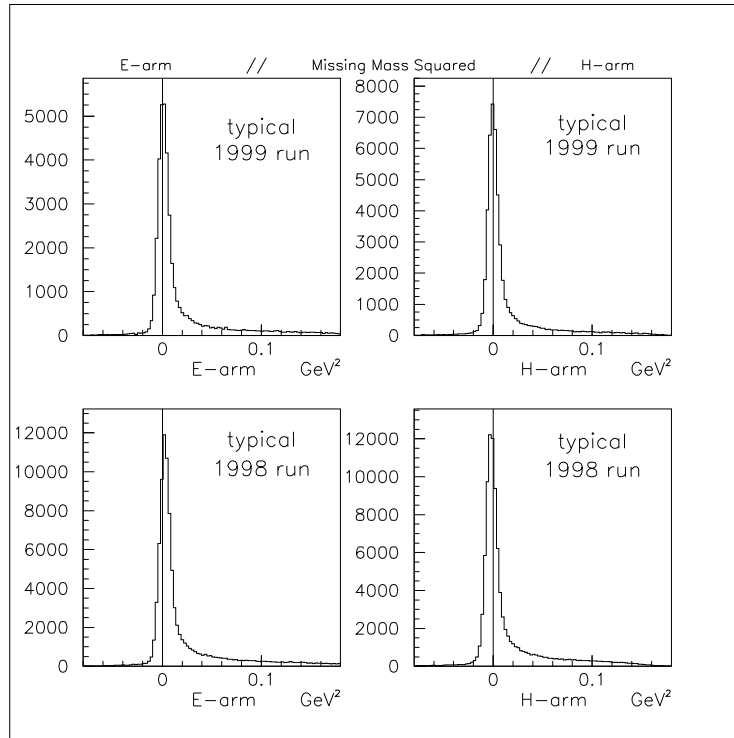
Figure 5.6: Typical missing mass peaks for 1999 and 1998 runs, after momentum scale adjustments. Data for Electron-arm on the left, the Hadron-arm on the right.

Q^2 for all three databases. In comparing the results, averaging over the databases and the two spectrometers, we were left with a residual variation in Q^2 of ± 0.4 %. This, we presume, is due to instability of the reconstruction matrix elements, and is assigned as such in the error budget shown in Table 5.3.
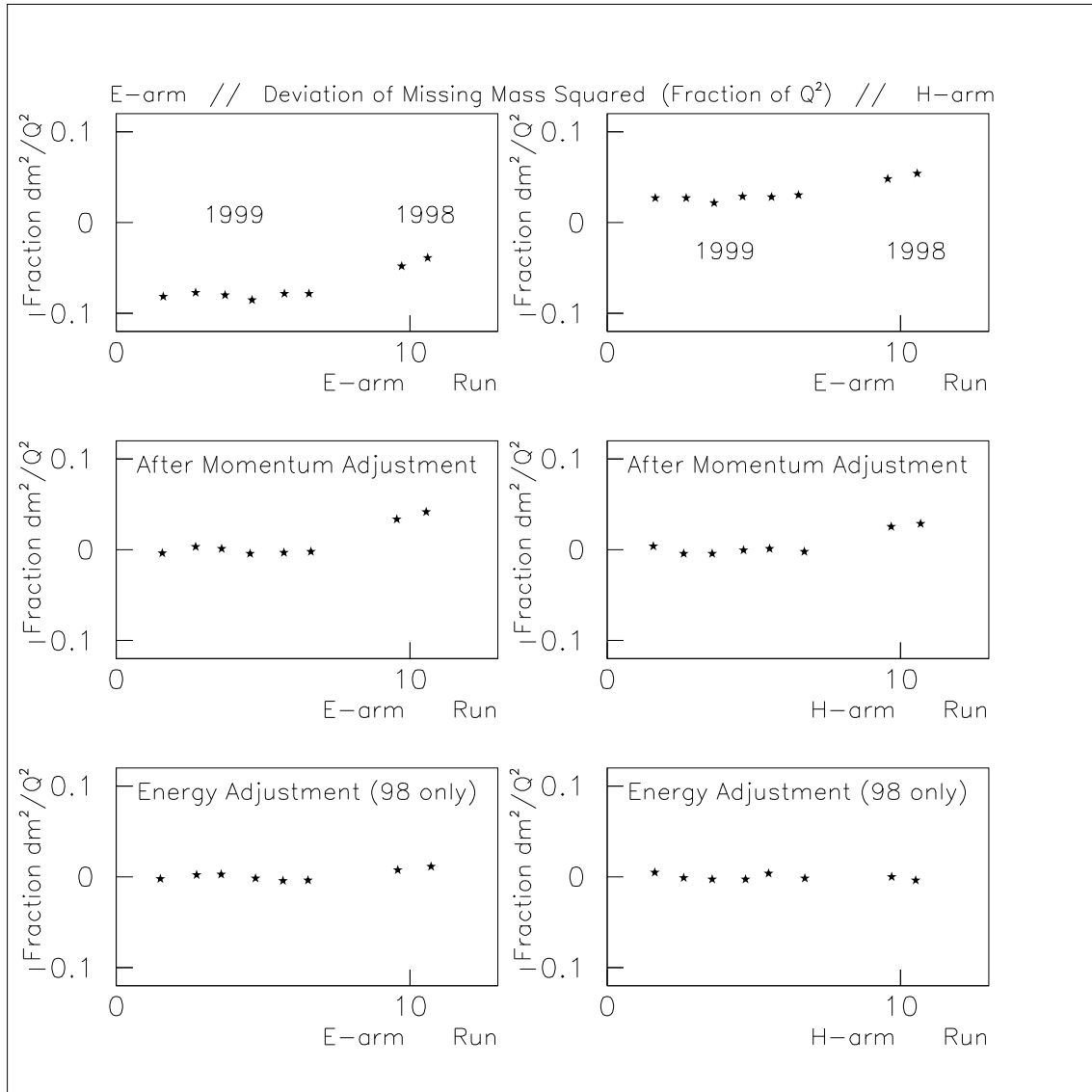
Figure 5.7: Missing mass squared (as a percentage of Q^2) for various runs. The E-arm is in the left plots; the H-arm on the right. The top two plots are with no correction to the momentum scale (angle correction has been done.). In each plot the first 3 points are runs from 1999 part I, the next 3 points are runs from 1999 part II and the last 2 points are for 1998. The middle group of 2 plots are after corrections to the momentum scale (of order 0.5%). The bottom group of two plots is after adjusting the 1998 beam energy by -8 MeV (-0.2%).

5.2.3.6   Trigger Bias

Momentum spectra from 1999 I runs, shown in Fig. 5.1, exhibited a strange 'shoulder' in the histograms which seemed to indicate missing momentum or missing events within a particular momentum range.

Q^2 was normally measured with using the 'HAPPEX' trigger which used the HAPPEX detector signal as the event trigger to strobe the MLU (memory lookup unit). When the MLU receives a strobe, it checks its inputs against pre-programmed logic conditions. When the strobe from a detector or scintillator comes in, the MLU makes a decision whether or not to signal the Trigger Supervisor (TS) to accept event data.

Under normal operation, only the HAPPEX detector would send trigger strobes to the MLU. During the 1999 I run, however, Q^2 was sometimes measured with the HAPPEX and the S1 and S2 scintillator planes turned on. This was a problem because signals from the S1 plane caused a non-uniform trigger inefficiency which distorts the momentum distribution, which thus biases Q^2 calculations. Trigger inefficiencies were caused when either S1 or S2 scintillator planes were turned on. Only the S1 plane caused a non-uniform inefficiency. The S1 plane was not uniformly populated as the lower 3 paddles had been removed to accommodate the HAPPEX detector (see Fig. 4.25).

The problem was caused by the 65 ns time lag of the HAPPEX detector to the scintillators. When the scintillators were turned on, any signal from them would kill the HAPPEX trigger from the HAPPEX detector. The MLU would then instruct the TS to ignore the HAPPEX detector signal. This produces a 'hole' in the momentum measured by the HAPPEX trigger. This momentum hole is illustrated in Fig. 5.1 in the center panels (1999 part I). It was important to verify this theory of the momentum bias so as to rule out other pathological problems with the data from the 1999 I run period. An empirical study of scintillator timing distortions with the MLU was undertaken[100] to compare momentum distributions with S1(on)-biased distributions. The results of this study are shown in Fig. 5.8. A list of trigger combinations and their effects is listed in Table 5.2.

The data from runs with the HAPPEX+S1(on)+S2(on) were not used to compute Q^2. Instead, Q^2 for the 1999 part I was computed from data using only the S2(on) trigger. For 1999 part II, the S2(on) and the HAPPEX+S(off) data was used

Trigger configuration	Description	Bias to Q^2
H-S(off)	HAPPEX Trigger, Scint S1 and S2 off. this provided the cleanest measurement of Q^2	none
Standard S-Ray Trigger	HAPPEX detector removed. This was used for raster tests.	none
S2(on)	Require S2, Leave S1 on or off. This was used for detector alignment studies.	none
H-S1(off)-S2(on)	Require HAPPEX trigger, S1 off, S2 on. This was used for 1998 Q^2 measurements.	small
H-S1(on)-S2(on)	Require HAPPEX trigger, S1 on, S2 on. This was used for some of the 1999 part I runs.	severe

Table 5.2: Triggers Used to Measure Q^2.

to calculate Q^2.

5.2.4 Q^2 Summary

Table 5.3 shows the summary of the errors in the Q^2 determination. The largest error contributions to Q^2 are position uncertainties from either the beam location or spectrometer surveys. Final Q^2 values are shown in Table 5.4.

Error Source	Error (in source units)	Percent Error in Q^2
VDC Timing Calibration (T_0)	$\leq$5 nsec	$\leq 0.1\%$
Factors Affecting the Angle:		
Beam position	0.5 mm	0.5%
Survey of Spectr. Angle	0.2 mrad	0.3%
Survey of Mispointing	0.5 mm	0.5%
Survey of Collimator	0.5 mm	0.5%
Target Z position	2 mm	0.3%
Spectrometer Momentum Scale	3 MeV	0.1%
Beam Energy	10 MeV	0.3%
Matrix Elements		0.4%
Total Systematic Error		1.2%
Statistical Error		$\leq 0.1\%$
TOTAL ERROR		1.2%

Table 5.3: Summary of errors in Q^2.

	1998 Run	1999 Run (part I)	1999 Run (part II)
Incident Energy (GeV)	3.345	3.353	3.316
E-arm Angle (degrees)	12.528	12.527	12.527
H-arm Angle (degrees)	12.558	12.562	12.562
E-arm Q^2 (GeV/c)^2	0.473±0.006	0.477±0.006	0.466±0.006
H-arm Q^2 (GeV/c)^2	0.475±0.006	0.477±0.006	0.466±0.006

Table 5.4: Q^2 summary for 1998 and 1999 HAPPEX runs.
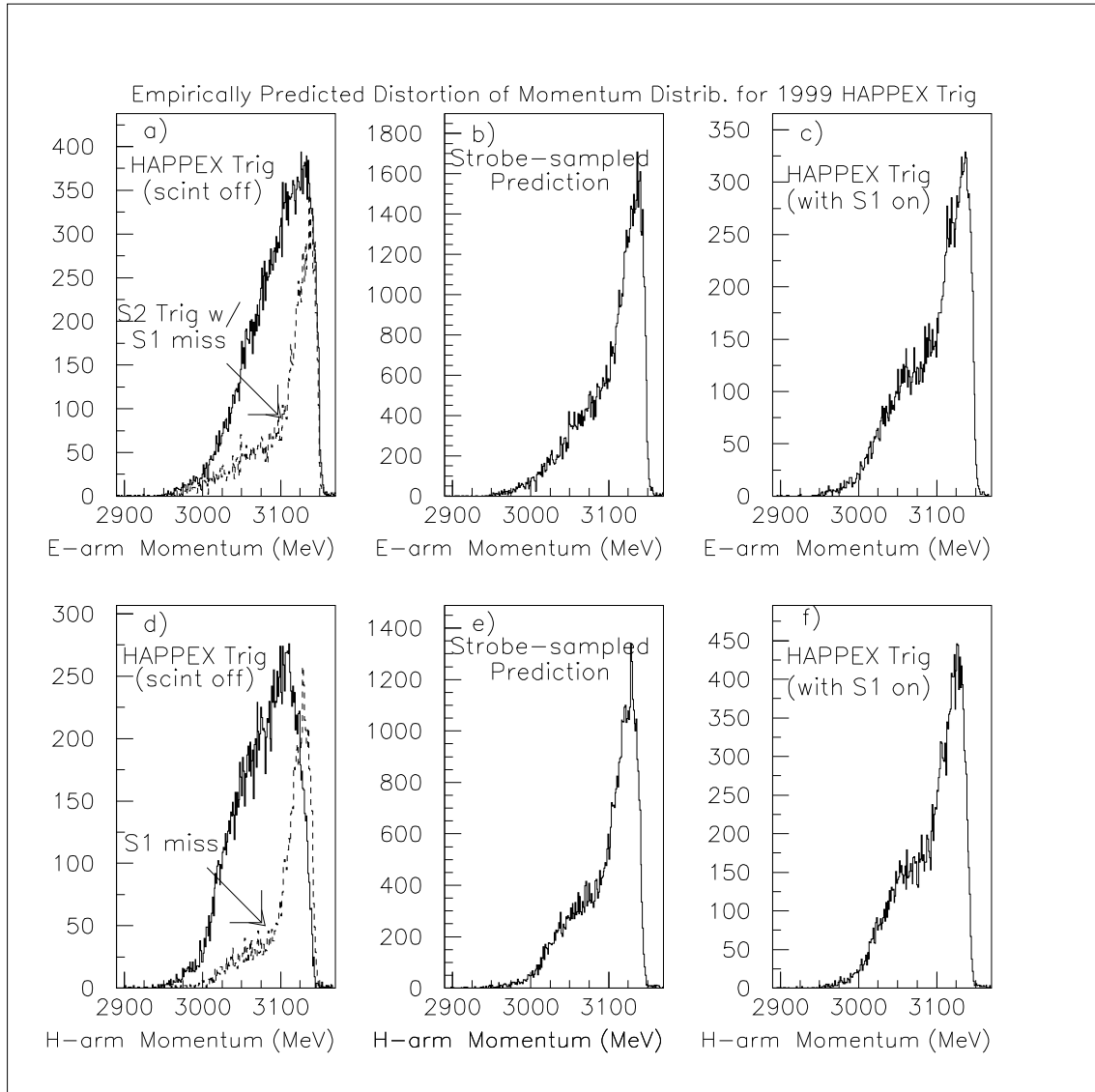
Figure 5.8: Momentum Distortion Distributions from Trigger Bias. Using scintillator data to predict the distortions observed in the HAPPEX trigger when S1 is left on, panel a) shows the momentum for HAPPEX trigger with scintillator off. The hatched line shows the momentum for S2 trigger when S1 is missing. This would be the momentum distribution if we used the HAPPEX trigger and left S1, but not S2, turned on. The inefficiency due to S1 causes this shape. S2 also causes an inefficiency but not a distortion. Adding these two distributions together with weighting by the independent contributions of S1 yields the prediction in panel b). This is compared with the H-S1(on) trigger shown in panel c).

5.3   Polarimetry

Polarization results measured with the Møller turn out to be dependent upon the slit-attenuator configuration which is used to limit the beam current. If the aperture is narrow, as was the case for the beam current limits of the Møller measurements, the Møller sees only a small part of the beam(time) profile, or phase. Different parts of the beam phase were shown to have different polarizations. The beam polarization drops off by about 5% on the tail of the beam phase. Thus depending on which part of the phase the Møller measured, this could systematically lower the average beam polarization. Møller polarization measurements during HAPPEX, using a default phase on the tail of the beam profile, would then be $\approx 5\%$ lower than the HAPPEX average polarization which used a completely open aperture. Beam current also follows a similar dependence on the beam phase and drops off 10% to 20% on the tail. Cuts were made at $\approx 0.5\%$ beam current to ensure the Møller measurements used were those from the full polarization peak and not the lower polarization tail. Fig. 5.9 shows a comparison of Mott and Møller measurements from April-May 1999.

5.4   Backgrounds

There were two primary sources of background events which could affect the HAPPEX asymmetry measurements. The first are electrons from the target cell's aluminum end-caps. The second is backgrounds contributed from inelastically scattered electrons which rebounded into the detector.

Aluminum Target Cells

Scattering from the target aluminum end-caps contributed $(1.4 \pm 0.1)\%$ of the detected signal. This was measured by using "dummy cells" which are constructed to mimic an empty beer-can cell. The aluminum of the dummy-cell "windows" was 10 times thicker than the aluminum end-caps of the lH_2 cell to compensate for the radiative losses in the hydrogen cell.

The measured HAPPEX asymmetry needs to be corrected for the asymmetry due to the quasielastic scattering of electrons from protons and neutrons in the aluminum. For quasielastic scattering from a nucleus with Z protons and N neutrons,
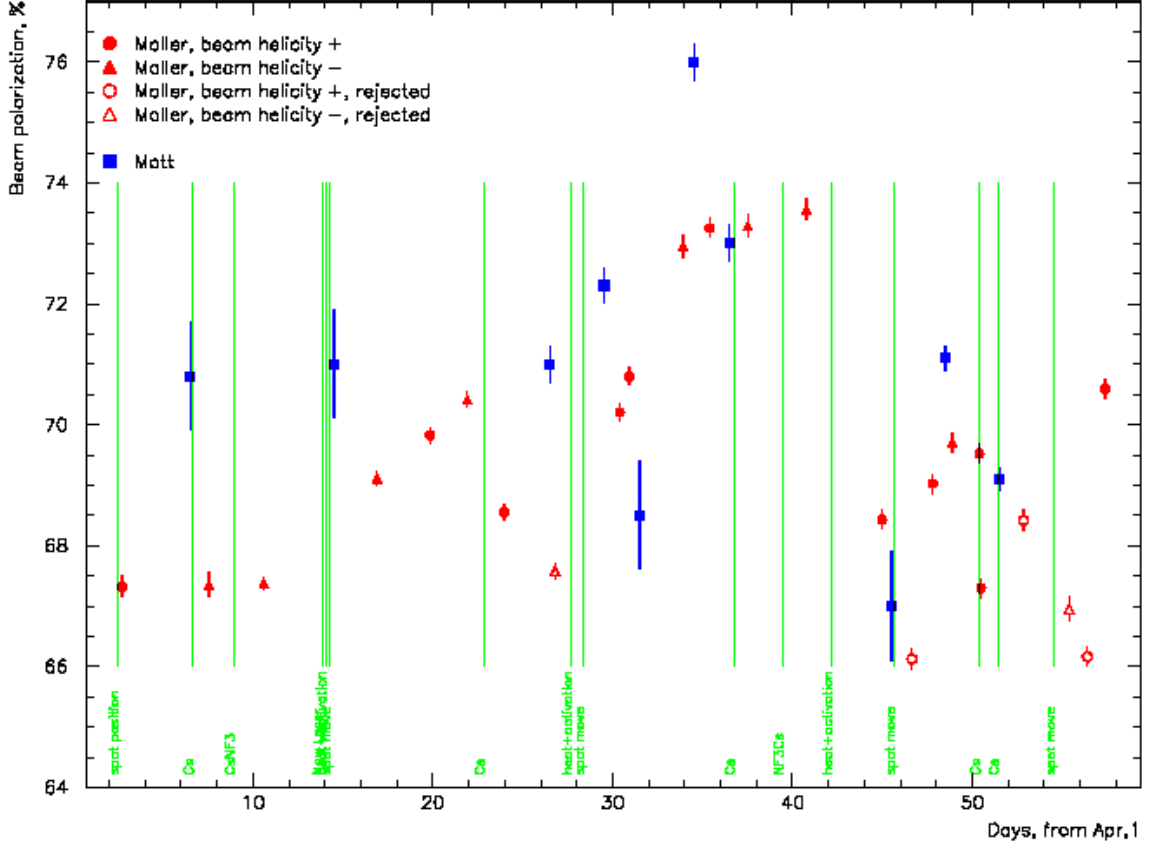
Figure 5.9: Møller and Mott polarization measurements. The green lines indicate various changes in the source or adjustments to the photocathode, such as re-cesiation, laser beam-spot relocation to improve QE, etc.

the parity violating asymmetry is [101]

$$A_{\text{aluminum}} = \frac{-G_F |Q^2|}{4\sqrt{2}\pi\alpha} \frac{W^{\text{PV}}}{W^{\text{EM}}} \tag{5.11}$$

where

$$W^{\text{EM}} = \epsilon[Z(G_E^{\gamma p})^2 + N(G_E^{\gamma n})^2] + \tau[Z(G_M^{\gamma p})^2 + N(G_M^{\gamma n})^2] \tag{5.12}$$

and

$$W^{\text{PV}} \approx \epsilon[ZG_E^{\gamma p}G_E^{Zp} + NG_E^{\gamma n}G_E^{Zn}] + \tau[ZG_M^{\gamma p}G_M^{Zp} + NG_M^{\gamma n}G_M^{Zn}] \tag{5.13}$$

Small axial vector and radiative corrections terms have been neglected. The asymmetry for quasielastic aluminum scattering is predicted to be -24 ppm at our Q^2. Assuming a 30% relative accuracy for this prediction, an asymmetry correction of 0.12 ± 0.04 ppm was calculated.

Inelastic Scattering

Inelastic scattering is the main contributor to background processes in electron-proton scattering. Inelastic electrons from this process can re-scatter inside the spectrometers and may reach the focal plane detectors. Most of these re-scattered particles are low-energy charged or neutral particles which contribute little to the integrated signal in the detectors. An optics simulation of the spectrometers was used to study this re-scattering hypothesis. In addition, the data were taken with the spectrometers "mis-tuned" to force elastically scattered electrons into following trajectories of inelastic electrons. Measurements were done with both the HAPPEX DAQ, and the standard Hall A DAQ.

Contributions from inelastic events, such as the Δ resonance, are suppressed two orders of magnitude by the spectrometers. Fig. 5.10 shows the re-scattering contribution at HAPPEX kinematics as a function of spectrometer miss-tune. The asymmetry from the Δ resonance, A_{PV}^{Δ}, is predicted to be -47 ± 10 ppm at our kinematics[45] which is 3 times as large as the asymmetry for elastic scattering. It is important, therefore, that contributions from this source were suppressed as there was no event veto or particle ID in this experiment.

Another potential source of background is the Møller scattering off of electrons in the magnetized iron of the spectrometer. Tests for this were done using "proton tagging" where protons from elastic ^{1}H(e,e'p) scattering were used to tag the electrons. The spectrometers were mis-pointed so protons well within the acceptance of the Hadron-Arm coincided with electrons on the very edge of the Electron-Arm acceptance. Thus, the protons can tag potential pole-tip scattering electrons. No significant 'pole-tip scattering' candidates were seen. An upper bound of energy deposited in the HAPPEX detectors was set at $\leq 10^{-4}$ percent of the total energy. In addition, simulations of the spectrometer optics confirmed that no particle trajectories which strike magnetized iron can survive the remainder of the trip. Analysis shows that the correction to the asymmetry data is a product of the detector signal fraction, the polarizations of the electron and 'Møller electron' in the iron, and the analyzing power of this event. The result is a very conservative $dA \leq 0.26$ ppm and no corrections were made for this effect[102].

Table 5.5 lists the backgrounds and corrections to our data and the systematic error to the data.

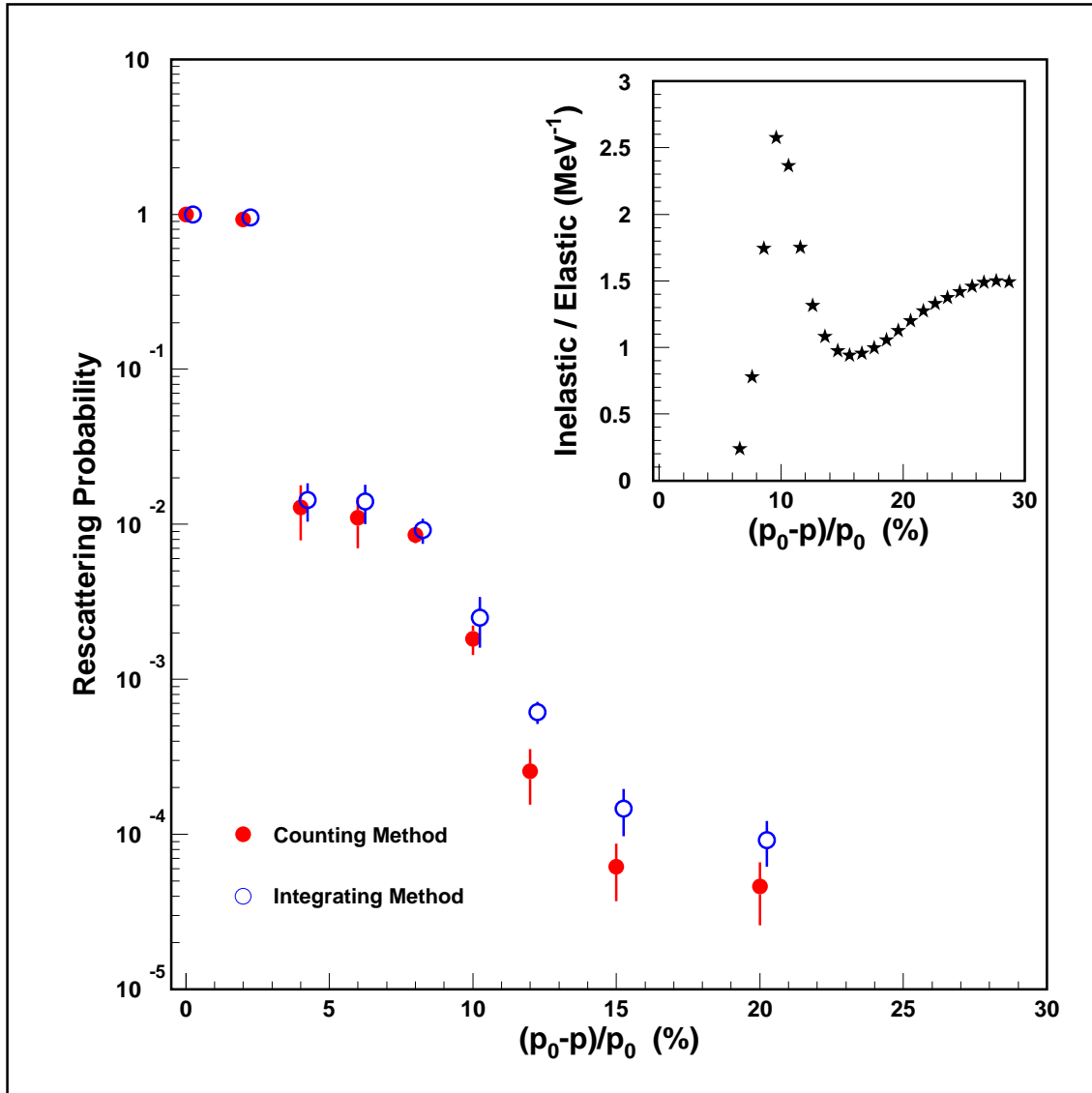| Source	Fraction of Events	A (ppm)	Correction (ppm)
Inelastic (Δ)	0.2 %	-47	0.06 ± 0.02
Quasielastic (Aluminum)	1.4 ± 0.1 %	-24	0.12 ± 0.04
Scattering from Poles	$\leq 10^{-4}$	0	0

Table 5.5: Backgrounds and Corrections.

Figure 5.10: Background re-scattering probability as a function of spectrometer mis-tune. This shows the probability that low-energy particles will evoke a DAQ trigger as a function of the percent momentum difference from the nominal spectrometer tune. The inset shows the inelastic/elastic relative momentum spectrum in these same units of % mistune.

5.5   Detector Performance

Čerenkov Angle

The Čerenkov light from the electromagnetic shower in the lead/Lucite layers will transit the length of each layer, directly and by internal reflection, to the PMT. Given the geometric properties of the Lucite layers, a variation in light transmission can be expected as a function of angle of the incident particle. This geometric-optical property was modeled using the optics modeling code GUIDEM[103]. The model, set up for simulation of a single Lucite layer, suggested a maximum light transmission would occur at roughly 42° degrees and a minimum of transmission at roughly 100° degrees. A bench test using through-going, minimum-ionizing cosmic rays (shown in Fig. 5.11) was set up to measure this angle dependence. The model of
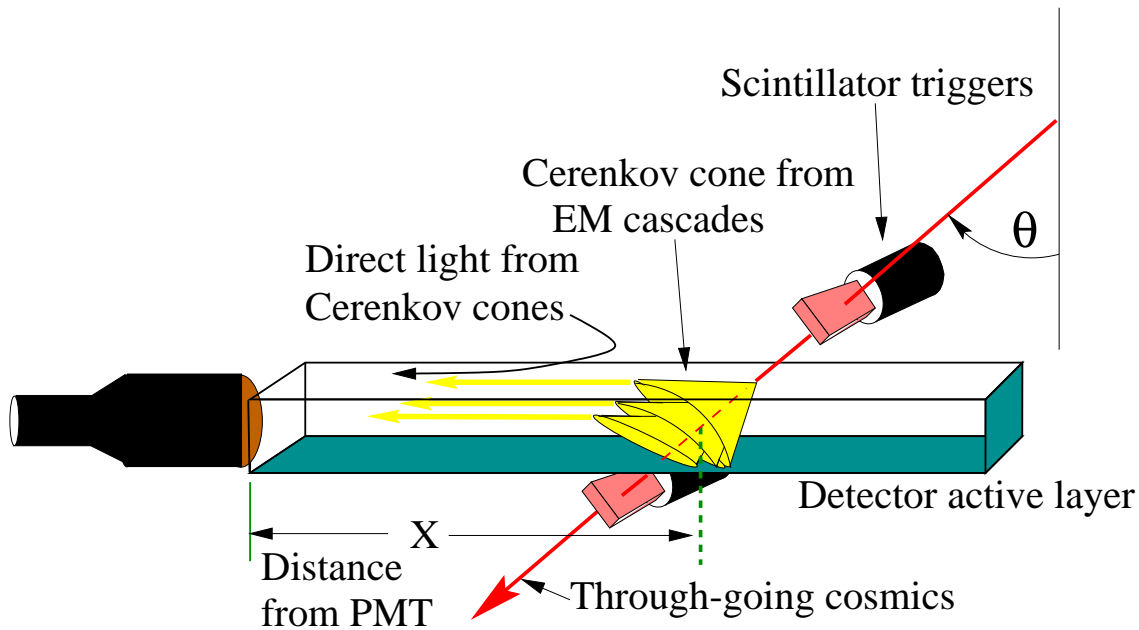
Figure 5.11: Bench test of detector angle response.

this angular dependence agreed qualitatively with the bench testing with the noted difference that only one layer of Lucite was modeled while a full shower through all five layers was measured. The results of the simulation and the bench tests are shown in Fig. 5.12, and 5.13 respectively. Knowledge of this maximum-gain-angle allowed adjustment of the detector 'pitch' (figure 4.31) to optimize the signal yield of the incident electrons, since their trajectory angle was known. This angular dependence
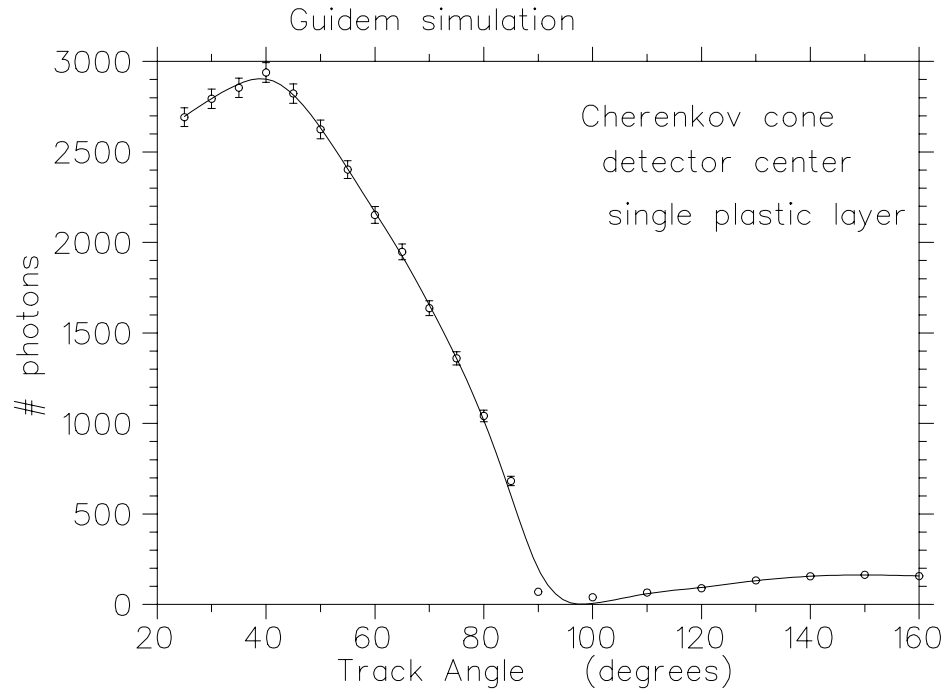
Figure 5.12: GUIDEM Simulation of detector angle response.
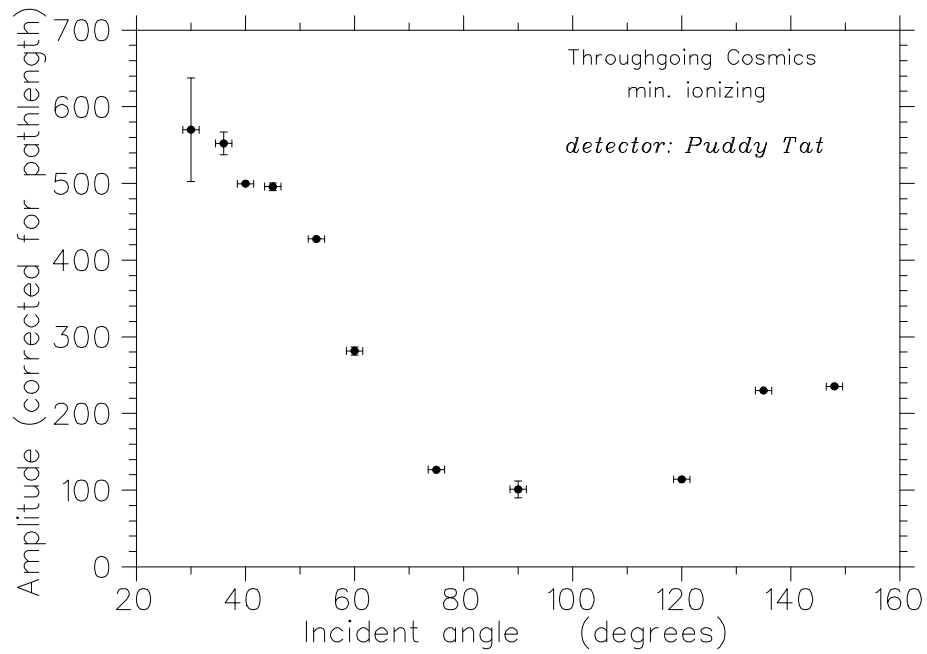
Figure 5.13: Results of Bench test of detector angle response.

was important for other reasons as well. By setting the pitch to the maximum angle of the known trajectories, electrons from background effects (especially from re-scattering in the spectrometers) would not cross the detector at the 'magic' angle and thus contribute significantly less signal than proper events.

Also, since we knew the electron's Q^2 as a function of its focal plane angle, adjusting the pitch of the detector allowed us to maximize the detector response for a particular Q^2. This allowed us to enhance detector response for a particular Q^2 and decrease the sensitivity for others. In this way we could pick an angle for which the detector's signal was less dependent upon Q^2.

Light Attenuation

Light attenuation in the HAPPEX detectors, as discussed in section 4.8.3.1, is due to the strong UV absorption properties of the Lucite used as the optical elements of the detectors. To neutralize the signal dependence on length due to the UV absorption, a UV filter was inserted between the Lucite and the PMT. This made the light attenuation in the detector more linear and more homogeneous by effectively blocking out all UV regardless of where it occurs in the linear length of the detector. Attenuation versus length data, comparing the detector with and without the UV filter, are shown in Fig. 5.14. Through-going cosmic rays, at 45°, are used for these data.

Linearity

Detector nonlinearity is a potential source of systematic error and as such was monitored regularly. It was critical that the detector pedestals did not drift or fluctuate on time scales on order of the helicity flipping frequency.

Detector signal linearities were monitored by comparing one detector's asymmetry drift with the other detector's asymmetry drift. The principle idea here is the low probability that both detector pedestals will drift the same way at the same time. If there is no drift, both detector's asymmetry will respond identically and thus plotting one vs. the other will give a slope of one. This is shown in Fig. 5.15. Pedestal drifts signaling possible systematic errors will show up as deviations from a fit to unity.

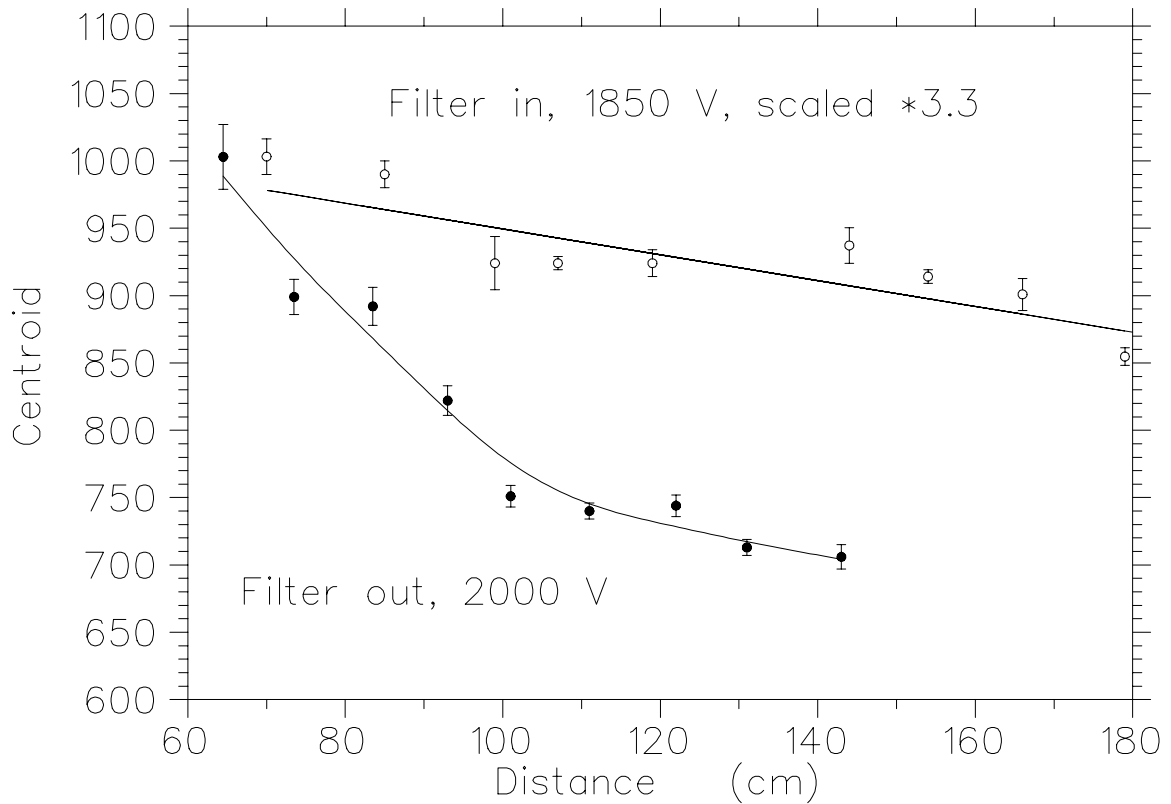A similar test was to monitor the slope deviations from detector asymmetries vs.

Figure 5.14: Detector UV Attenuation as a function of length. The solid-circles show the attenuation per unit length with no UV filter. The open-circles show the attenuation per unit length with the filter installed. The vertical axis is the centroid of the ADC distribution for each position.

beam current asymmetries. Again, since the detectors measure a signal proportional to the beam current, the helicity-correlated asymmetry in the detectors should respond identically with the helicity-correlated asymmetry of the BCMs. Deviations from a slope of one would signal possible systematic errors or pedestal drifts in the equipment. Shown in Fig. 5.16 is the calculated slope from these tests as a function of run number for data taken from 1998. This shows the long term stability of the pedestals. Most of the slopes are consistent with 1 and the larger error bars on some indicate low statistics runs. 1999 data was similar.

Similar methods were used to check BCM linearity performance by comparing one BCM with another. Again, the idea being that the BCMs being compared will exhibit the same asymmetry if neither are drifting with respect to the other (Fig. 5.17).

(det1r−det1l)/(det1r+det1l)*1.e6 VS. (det2r−det2l)/(det2r+det2l)*1.e6
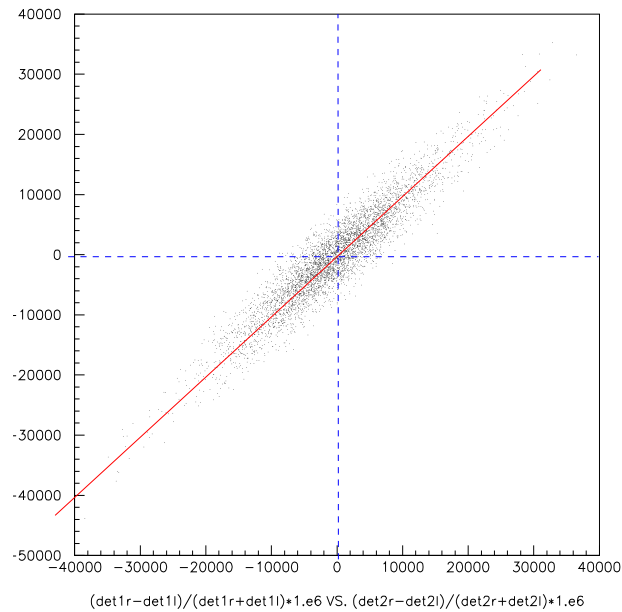
Figure 5.15: Detector asymmetry comparison. The axes are detector asymmetries in parts per million.

Detector linearity - Slope of (A_{det} vs. A_{BCM1})

<slope> = 0.994 ± 0.004

<slope> = 0.998 ± 0.004
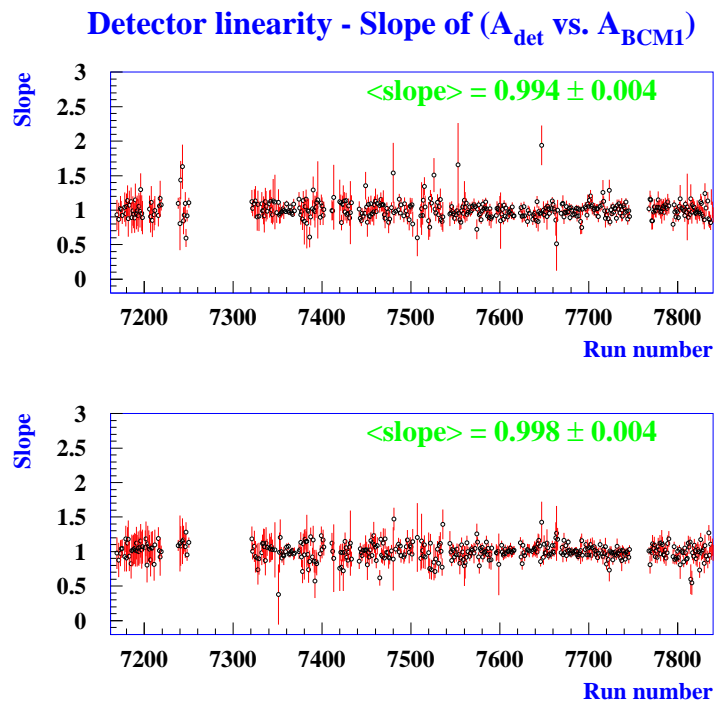
Figure 5.16: Detector-BCM linearity. Shown here are deviations from 1.0, per run, for each detector, for 600 runs. The hadron arm detector is shown in the top plot, the electron arm detector in the lower plot. These data are from 1998. The 1999 data are similar.
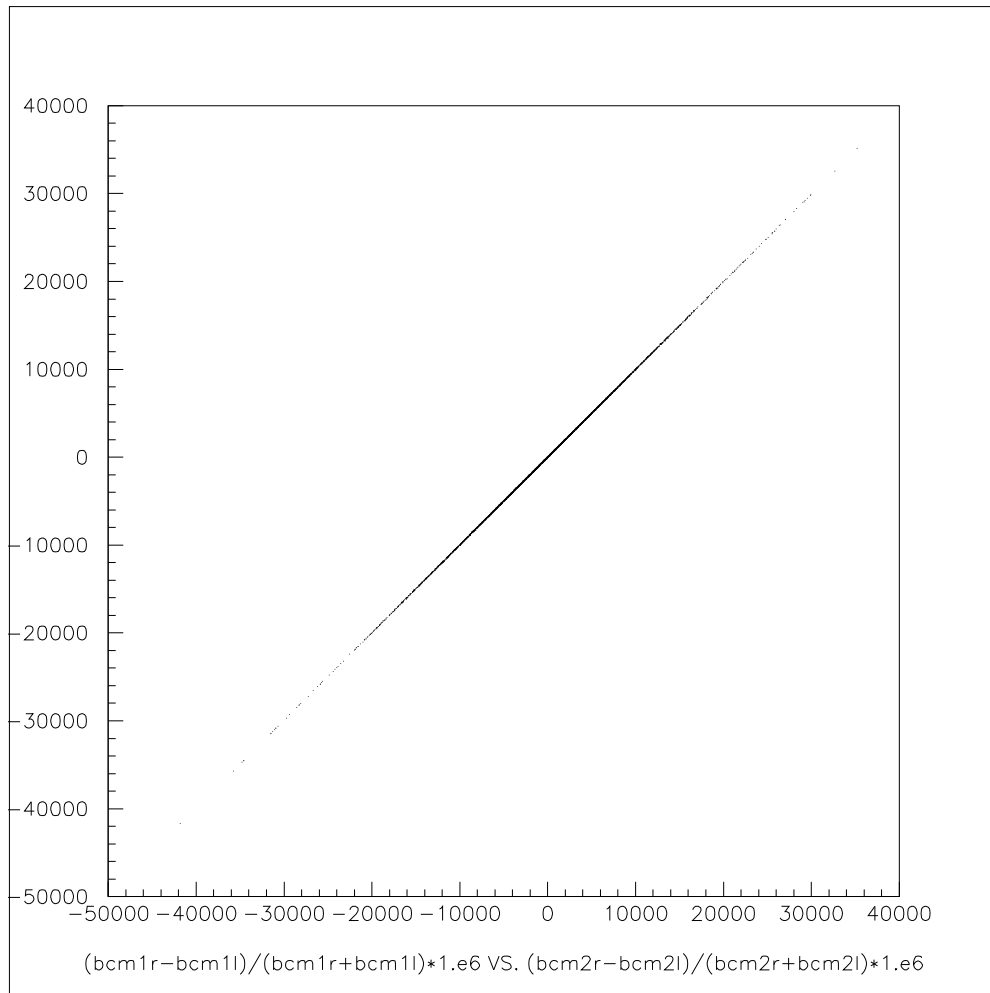
Figure 5.17: Asymmetries of BCM1 vs. BCM2. These data are from the 1999 run.

Detector Stability and Drift

As an additional check on detector performance and stability, the light attenuation per unit length was monitored periodically throughout the HAPPEX experiments. These studies looked for relative changes in the per-unit length attenuation as a way to monitor radiation damage to the Lucite. Shown in Fig. 5.18 is a plot of the ratio of the electron's momentum (as measured with the VDCs) to the ADC signal of the PMT. This is plotted as a function of relative distance from the PMT. The slopes were compared for changes over the period of all HAPPEX runs. Radiation damage would be indicated by an increase in this slope over time. The slope of relative attenuation per unit length did not change throughout the 1998 or 1999 runs. It was concluded that the Lucite elements of the detectors suffered no radiation damage.
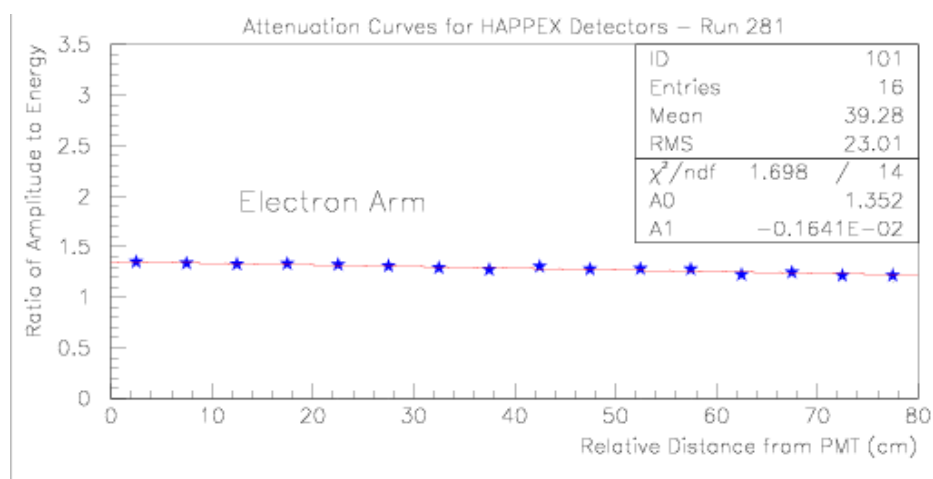
Figure 5.18: The ratio of electron momentum to ADC amplitude as a function of detector length. The data for the Hadron-Arm are similar.

5.6 Asymmetry Analysis

The analysis of the physics asymmetry was a multi-step process which falls into the following categories:

- **Analysis technique**

  Dedicated analysis software, ANPAR, was written specifically for this purpose. The analysis was designed to include several automated cross-checks and checks on systematics.

- **Cuts**

  Not all of the data are usable. Various methods and 'cuts-rules' are created to deal with expected rejections such as equipment malfunctions as well as subtle data errors which affect parity data in particular. In addition, to prevent biasing the results, the 'cuts-rules' must protect against 'over-cutting' questionable but otherwise good events.

- **The raw-asymmetry**

  The measured raw asymmetry and its sign must be checked against statistical expectations. Also a systematic test affecting only the sign of the asymmetry can be employed to ensure the asymmetry is a physics effect not an instrumental construct. This check is independent of any other systematic errors.

- **Systematics**

  Various systematic errors are produced by a number of instrumental and machine effects. These effects can all appear to be part of a helicity-correlated cross section asymmetry. If undetected and uncorrected, these helicity-correlated systematics would bias the physics asymmetry calculations.

5.6.1 Cuts

Cuts on the data used for calculating the raw asymmetry were made as loose as possible. Cuts were made largely only when equipment was malfunctioning. For example, data cuts were made when the beam current dropped below 3μA. Shown in Fig. 5.19 is a typical cut triggered by beam drop-out. The cut interval is set to precede the dropout point by 10 windows and to resume 50 windows after beam is reestablished. The 50 window delay (~ 1.667 seconds) allows the beam and

target to stabilize. Cuts were also made when the DAQ failed, detector HV voltages tripped off or if the spectrometer's magnetic field setting drifted. Table 5.6 shows the percentage of data lost for each type of cut.

It is important to note that decisions on cuts were made *before* the data were analyzed. In addition, *no* cuts were made on the asymmetry. Thus choice of cuts were not tempted by the quality of the data.
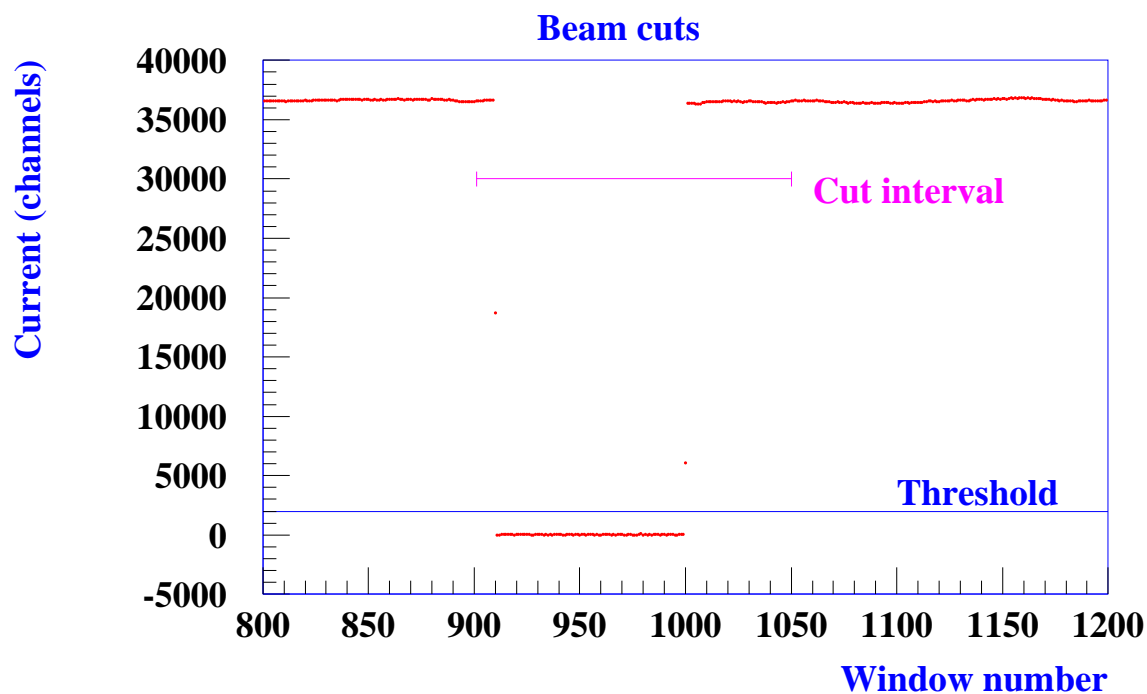

Figure 5.19: Data cut interval as a function of window number, for a region of time around a beam drop-out period.

Cut	Percent data loss
Detector HV off	0.1%
Target boiling	0.4%
Data acquisition failure	2.2%
Spectrometer mis-tuned	3.8%
Beam unstable or off	5.2%
Total cuts	11.7%

Table 5.6: Percentage of data lost due to the cuts

Beam Modulation cuts were used during the calculation of the helicity-correlated beam transport corrections of beam systematics. These cuts use separate criteria than the cuts used for the raw asymmetry data. These cut criteria were:

1. Beam energy modulation was too small or off.

2. PITA slope measurements were taking place.

3. Accelerator was using 'fast-feedback'. This affected the beam modulation control used to establish the beam transport helicity matrix.

4. DAQ errors or failures.

5.6.2 Asymmetry

The simple premise of the asymmetry calculation is to measure the difference in detector signal between the left and right electron helicity interaction rates,

$$A = \frac{\sigma_R - \sigma_L}{\sigma_R + \sigma_L} = \frac{D_R - D_L}{D_R + D_L} \tag{5.14}$$

where $\sigma_{R(L)}$ is the cross-section and $D_{R(L)}$ is the event rate seen by the detector, corresponding to right(left) beam helicity states. The event rate is directly proportional to the differential cross-section and the beam intensity. Because the event rate is also a function of beam intensity, this signal must be normalized to the beam current so that only helicity-correlated cross-section differences are computed. Thus the raw asymmetry is

$$A_{\text{raw}} = \frac{D_R/I_R - D_L/I_L}{D_R/I_R + D_L/I_L} \tag{5.15}$$

where $D_{R(L)}$ is the detector signal and $I_{R(L)}$ is the beam current signal corresponding to right(left) beam helicity states. As discussed in section 4.3.1.4, the electron helicity is reversed at a frequency of 30Hz. The signal from the differential cross section is integrated over the 33 msec windows for each right(left) helicity state. The asymmetry is then computed as 66.6 msec 'window-pairs' or 'pulse-pairs' of opposite helicity states. The helicity state of the first window of the pair is chosen randomly, the second window of the pair is opposite.

The data acquisition electronics built for HAPPEX integrated the signals from all sources directly and the integrated ADC values were read by the CODA run control

system. Given the relatively slow rate of the data acquisition, the asymmetry could be computed in real time. This allowed for much of the preliminary analysis to be done on line by ANPAR to check for signal pathologies or statistical anomalies as the data came in.

5.6.2.1   Sign of Asymmetry

An important systematic check for parity experiments is to reverse the electron helicity pattern without changing any other device systematics. This was accomplished by inserting a $\lambda/2$ plate in the laser beam. This procedure reverses the helicity of the electrons relative to normal operation and reverses the apparent sign of A^{PV}. The $\lambda/2$ plate position information, in or out of the laser beam, was not recorded in the data stream. Instead, information was recorded by hand in the Hall A log book. This technique precludes any information about the helicity-reversal status affecting any of the DAQ electronics which might bias the data with a systematic sign reversal. Any asymmetry sign reversal seen therefore, is an indication of the physics asymmetry. Averaging the asymmetry with this sign included cancels any systematic errors that do not depend on the status of the $\lambda/2$ plate[69].

The original assignment of the sign of the asymmetry with respect to the $\lambda/2$ plate was arbitrary. We used the Møller polarimeter to verify that the sign of the asymmetry was correct [92].

The Møller Helmholtz coils produce a magnetic field anti-parallel (parallel) to the beam when the voltmeter connected to their power supply reads + (-). A magnetic field parallel to the beam causes a net alignment of the magnetic moments of the Møller target electrons along the direction of the beam. Since electrons are negatively-charged particles, their spins are then aligned anti-parallel to the direction of the beam. In this case right-handed incident electrons have a larger cross section for scattering than left-handed electrons, and we expect to see a positive R-L asymmetry in the integrated Møller coincidence signal. For the 1998 runs we found that when the half-wave plate was in and the coil voltage read negative (indicating that the magnetic field was anti-parallel to the beam), the measured R-L asymmetry was positive. This shows that our arbitrary assignment of the beam helicity as right or left was correct when the half-wave plate is in and opposite when the half-wave plate is out. Again we concluded that the correct sign of our measurement of the

parity-violating asymmetry is minus. This was opposite for the 1999 runs. Typical results from these tests in 1998 are shown in Table 5.7. The magnitude of the asymmetry and the statistical error on the measurement are not relevant except to show that the measured sign is not statistically ambiguous. During the experiment

Date	Run Number	$\lambda/2$	Møller Coil	Asymmetry
April 26	7309	In	+	-1.87 ± .03
	7310	In	-	+1.81 ± .03
28	7370	In	+	-1.45 ± .05
May 3	7517	Out	+	+1.63 ± .04
	7518	Out	-	-1.49 ± .05
9	7593	Out	-	-1.76 ± .04
	7595	In	+	-1.62 ± .04
10	7620	In	-	+1.80 ± .02
15	7762	Out	+	+1.82 ± .02
	7767	In	-	+1.86 ± .02

Table 5.7: Data from Møller runs

the $\lambda/2$ plate was toggled into or out of the laser path every other day. Each group of $\lambda/2$ plate sets contained, on average, 48 one-hour runs. The average asymmetry for each group was calculated and normalized to 1.0. Plotting these results, as shown in Fig. 5.20, shows the effect of the asymmetry sign reversal with the toggling of the $\lambda/2$ plate. The sign reversal in the asymmetry indicates the asymmetry is a physics phenomenon not a systematic construct.

5.6.2.2 Other Systematics

Helicity-correlated beam intensity was the only non-zero (to first order) systematic quantity. This systematic was kept to less than 1 ppm by a slow feedback on the PITA effect as discussed in section 4.3.1.3.

Another source of systematics is helicity-correlated changes in parameters that affect the measured scattering rates. Again, to first order, the detector rates, $D_{R(L)}$ are a function of beam parameters incident on the target. Excepting beam intensity, which is handled separately, the rate differences seen by the detectors is a function of Beam energy, E, Beam position at the target, X, Y; and Beam angle at the target, θ, ϕ. Helicity-correlated changes in any of these parameters will affect
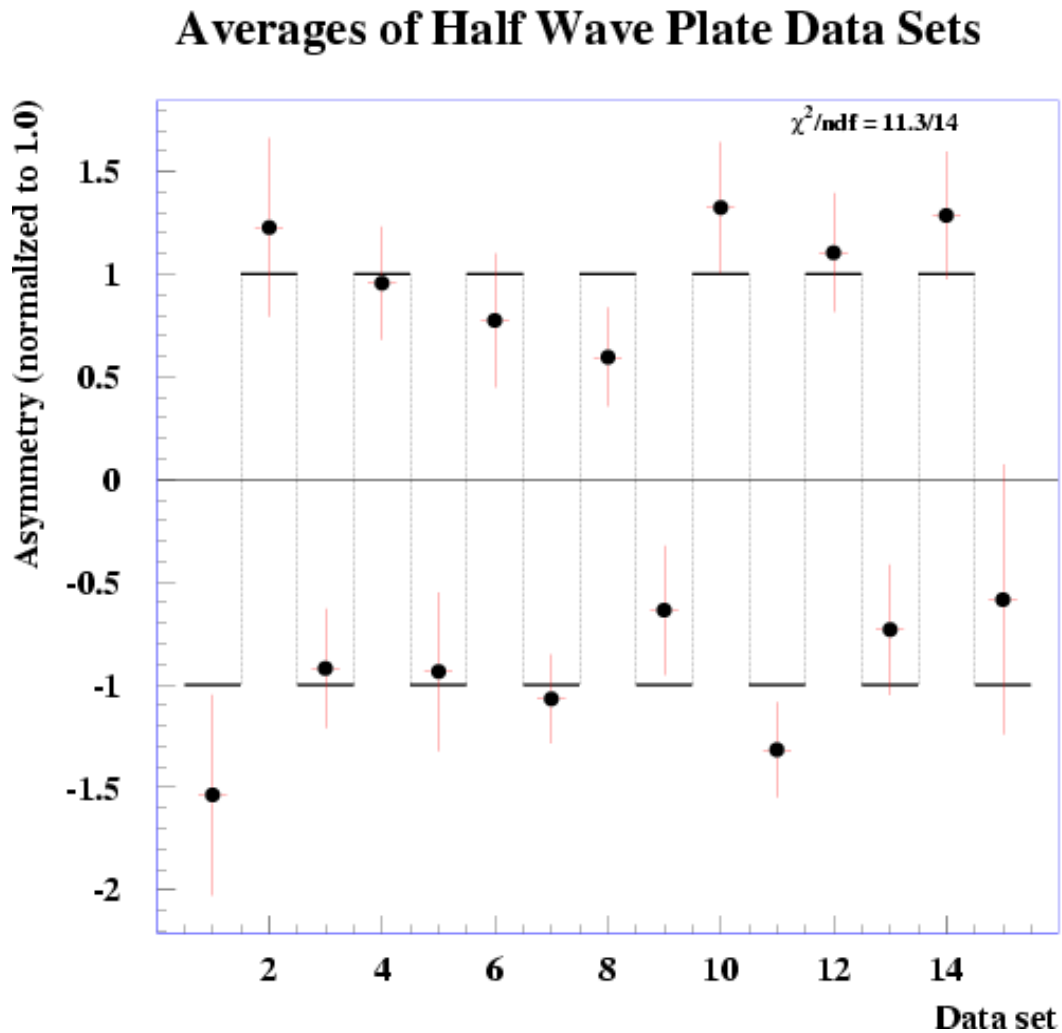
Figure 5.20: $\lambda/2$ plate asymmetry sign reversal. The physics asymmetry, here normalized to 1.0, is tested by inserting a $\lambda/2$ plate into the laser beam path before the photo-cathode at the source. These data are from the 1999 part I run; shows the $\lambda/2$ plate was inserted for the even data sets.

the detector rate and thus affect the apparent physics asymmetry, A^{PV}. Helicity-correlated fluctuations in these parameters, however, can be measured and later corrected for using the Beam Modulation Technique.

Beam Modulation Analysis

By modulating the beam parameters and measuring the cross-section sensitivity of the detector signal to these parameters, we obtained coefficients with which we can calculate corrections to the asymmetry caused by helicity-correlated fluctuations in these parameters. The raw asymmetry is then corrected for the systematic asymmetry

$$A_{\mathrm{exp}} = A_{\mathrm{raw}} - A_{\mathrm{sys}} \tag{5.16}$$

where A_{exp} is the experimental asymmetry and A_{sys} is the asymmetry due to helicity correlated systematic effects.

The systematic correction for the beam parameters can be written

$$\sigma_{sys} = \sum_{i=1}^{5} \frac{\partial \sigma}{\partial X_i} X_i \tag{5.17}$$

where X_i represents the parameters $(X,\ Y\ \theta,\ \phi, E)$ respectively. The fluctuations in the detector signal are linear combinations of these measured beam parameters. Beam modulation is the technique used to obtain the correction coefficients, $\partial \sigma / \partial X_i$.

In order to find $\partial \sigma / \partial X_i$, we need to perturb the beam parameters and observe the $\partial \sigma$ fluctuations. To this end, as described in section 4.5.3, we use steering or 'modulation' coils on the beamline and a energy vernier in the accelerator. These modulation coils are designated C_j, $j = 1 \ldots 5$. By pulsing the modulation coils we can measure the fluctuations per coil in the monitors, X_i and the detector signal σ_{sys}.

$$\frac{\partial \sigma}{\partial C_j}, \ \ \frac{\partial X_i}{\partial C_j}, \ \ i, j = 1 \ldots 5. \tag{5.18}$$

Next we need to invert the 5×5 matrix $\frac{\partial X_i}{\partial C_j}$:

$$\frac{\partial X_i}{\partial C_j} \longrightarrow \left(\frac{\partial X_i}{\partial C_j} \right)^{-1}. \tag{5.19}$$

This can be done only if $\frac{\partial X_i}{\partial C_j}$ is not singular. To meet this requirement we note that with seven coils (six coils and one energy vernier) , and twelve monitors (ten BPM plus two detectors) gives a total of ninety-six slopes from which to choose $\frac{\partial X_i}{\partial C_j}$. While only twenty-five values are needed to span the space of $\frac{\partial X_i}{\partial C_j}$, they are required to be orthogonal. That is, horizontal and vertical perturbations of the beam must be decoupled from each other. A horizontal deflection coil should move the beam only horizontally. Similarly vertical deflections should show vertical motion and little or no horizontal motion. If the beam perturbation of one coil was coupled to movement in both horizontal and vertical beam displacement, the matrix $\frac{\partial X_i}{\partial C_j}$ would be singular and non-invertible. An additional requirement is that each coil must perturb the corresponding monitor with sufficient amplitude or nonnegligible errors will propagate through the inversion process.

A typical matrix of $\frac{\partial X_i}{\partial C_j}$ is

$$
\begin{matrix}
-218.7 \pm 0.2 & -6.1 \pm 0.2 & 223.3 \pm 0.2 & 15.8 \pm 0.2 & 2.4 \pm 0.2 \\
-6.2 \pm 0.3 & 268.6 \pm 0.3 & 7.5 \pm 0.3 & -404.0 \pm 0.3 & 10.0 \pm 0.2 \\
-145.5 \pm 0.3 & -0.3 \pm 0.2 & 365.5 \pm 0.2 & 4.2 \pm 0.3 & -5.5 \pm 0.2 \\
-7.4 \pm 0.2 & -219.5 \pm 0.2 & 25.1 \pm 0.2 & -135.4 \pm 0.2 & 10.7 \pm 0.2 \\
-344.2 \pm 0.7 & 12.9 \pm 0.7 & -80.3 \pm 0.8 & -1.1 \pm 0.8 & 238.9 \pm 0.7
\end{matrix}
\tag{5.20}
$$

Once $\left(\frac{\partial X_i}{\partial C_j}\right)^{-1}$ is obtained we can build

$$
\frac{\partial \sigma}{\partial X_i} = \sum_{j=1}^{5} \frac{\partial \sigma}{\partial C_j} \left(\frac{\partial X_i}{\partial C_j}\right)^{-1}
\tag{5.21}
$$

Then substituting this into Eqn. 5.17 we have

$$
\sigma_{sys} = \sum_{i=1}^{5} \sum_{j=1}^{5} \frac{\partial \sigma}{\partial C_j} \left(\frac{\partial X_i}{\partial C_j}\right)^{-1} \langle X_i \rangle
\tag{5.22}
$$

The systematic asymmetry (ignoring beam-current normalization) is then

$$
A_{sys} = \frac{\sigma_{sys\,R} - \sigma_{sys\,L}}{\sigma_{sys\,R} + \sigma_{sys\,L}}
\tag{5.23}
$$

and the experimental asymmetry, with corrections is

$$
A_{exp} = A_{raw} - A_{sys}
$$

$$= \frac{\sigma_R - \sigma_L}{\sigma_R + \sigma_L} - \frac{\sigma_{sys\,R} - \sigma_{sys\,L}}{\sigma_{sys\,R} + \sigma_{sys\,L}} \tag{5.24}$$

Cross Talk

Electronic cross-talk among the components in the detector or DAQ system is another concern that might introduce helicity-correlated systematic errors. To monitor cross talk, several channels of the DAQ were connected to 1.5 volt batteries configured as current and voltage sources. Signals from these current and voltage sources were treated and cabled identically with the HAPPEX data signals. As the batteries cannot know of any helicity-correlated events, they provided signal sources which were, by definition, helicity-invariant. Helicity-correlated signal then, seen on these DAQ channels, would indicate helicity-correlated cross-talk or signal pick-up amongst the electronics. Results of these tests (shown in Table 5.8) are consistent with zero thus indicating negligible cross-talk.

Signal Source	Asymmetry
$V_{battery}$	-0.005 ± 0.007 ppm
$I_{battery1}$	-0.001 ± 0.015 ppm
$I_{battery2}$	0.005 ± 0.016 ppm

Table 5.8: Results of electronics cross-talk check.

As an additional precaution, the PMTs were isolated from earth-ground and shielded from all electronic noise in a grounded faraday-box. The shielded signals lines were electrically isolated from earth-ground until they reached the HAPPEX DAQ in the counting house. This method avoided ground-loops which could pick up helicity-correlated signals.

Chapter 6

Results and Discussion

6.1 Overview

The extraction of values for the strange quark form factors, G_E^s and G_M^s from the measured asymmetry requires interpretation of the theoretical asymmetry in terms of the electromagnetic form factors.

HAPPEX recorded a total of 179.6 coulombs of beam on target over three experimental runs. Shown in Fig. 6.1 are the statistical fluctuations in the pulse-pair asymmetries for 1999. Note the vertical scale; the data are Gaussian for over 7 decades.

Shown in Fig.6.2, panel a) are the raw asymmetry data. The data are grouped into $\frac{\lambda}{2}$ plate "slugs", where a 'slug' is a group of data sets taken with the $\frac{\lambda}{2}$ plate in. The next 'slug' is a group of data sets with the $\frac{\lambda}{2}$ plate out. The solid black bars of the square-wave like line indicate the average raw asymmetry, in ppm, for slugs with the $\frac{\lambda}{2}$ plate out and in, respectively.

The data from the three runs have been corrected for run-specific systematics and scaled in order to merge them into the final data point. The first step was to correct the 1998 data for a systematic error in the incident electron energy and background contributions due to the target windows. These corrections are discussed in sections 5.2.3.5 and 5.4 and are summarized below.

Next, this final number was adjusted for the finite acceptance of the spectrometers into a 'point' asymmetry value so that it can be compared to the theoretical
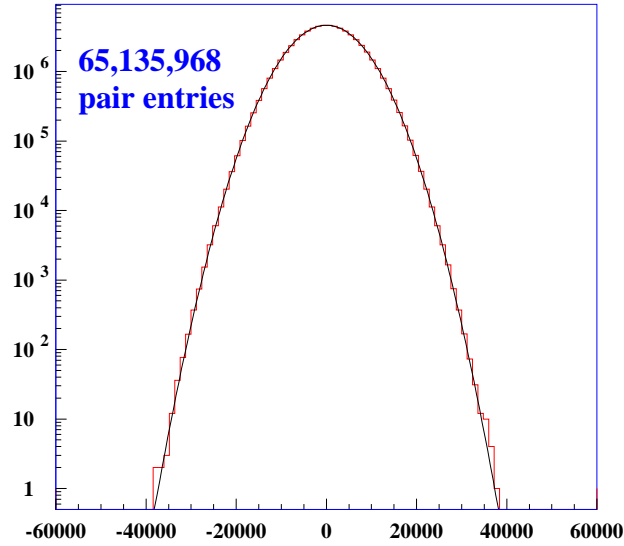
Figure 6.1: Pulse pair asymmetry for 1999. The 1998 data are similar.

asymmetry at a specific Q^2 value. The finite acceptance correction, calculated via Monte Carlo, was the same for all three Q^2 kinematics.

Third, the corrected 1998 and 1999 II asymmetries were scaled to the Q^2 of the 1999 I data. The corrections required for scaling in Q^2 were small and on the order of 1%. These scaled values were then combined into a weighted, final number.

Using some interpolation of the electromagnetic form factors, the theoretical asymmetry was calculated and then compared with A_{exp} to extract $(G_E^0 + 0.392 G_M^0)/(G_M^{p\gamma}/\mu_p)$.

6.1.1 Corrections

The 1998 data needed three small corrections to what was originally published [104], based on subsequent data analysis. These are discussed in sections 5.2.3.5 and 5.4. Corrections for backgrounds are listed in Table 5.5.

A summary of corrections and uncertainties is listed below in Table 6.1.1.

6.1.2 Finite Acceptance

In order to compare the measured asymmetry, which varies with Q^2, with the theoretical asymmetry which assumes a point value for Q^2, the Q^2 must be adjusted for the finite acceptance of the spectrometers. This is done by comparing the Monte Carlo scattering results to a point calculation assuming the effective kinematics.
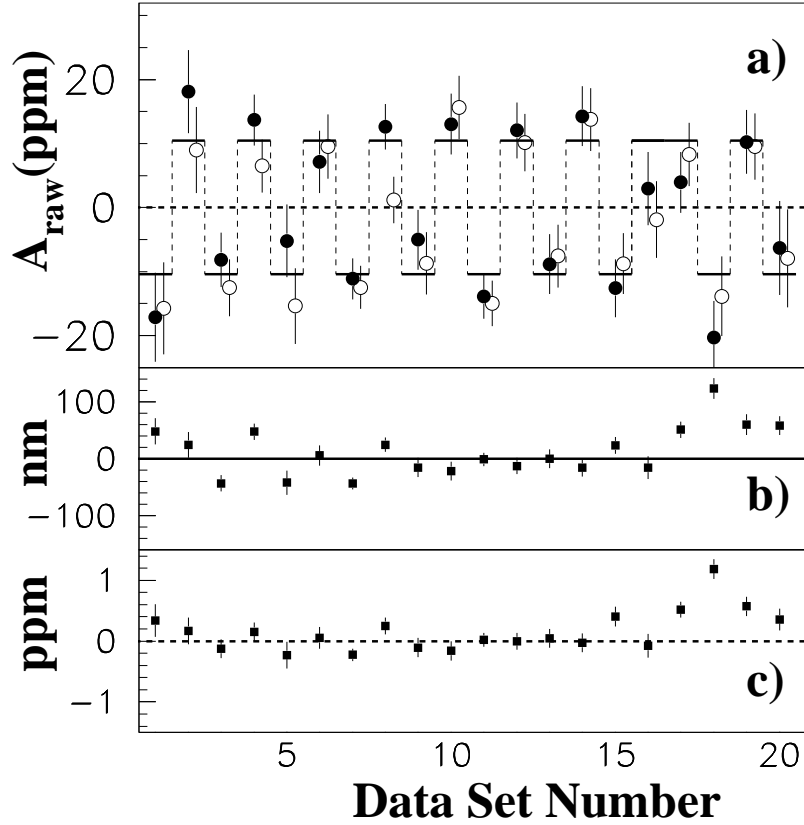
Figure 6.2: a) Raw asymmetry versus data set. Solid(open) circles are from the Electron(Hadron) spectrometer. The step pattern is due to the periodic insertion of the half-wave plate. The $\chi^2 = 33.7$ for 39 degrees of freedom. b) Helicity-correlated horizontal position difference measured near the target. c) Correction to left spectrometer data due to all of beam parameter differences.

The Monte Carlo assumes the same parameterization as the A_{th} calculation, namely the Galster parameterization for G_E^n and the Mainz data for G_M^n.

Taking the ratio of the average acceptance and point calculations yields a correction factor needed to extrapolate the measured asymmetry to the theoretical point calculation.

$$\mathrm{Correction\ \ Factor} = \frac{A(E_i, \theta_{eff})}{\langle A \rangle_{\mathrm{MC}}} = 0.993 \pm 0.003. \tag{6.1}$$

where E_i is the effective incident beam energy adjusted for target losses.

θ_{eff} is the effective scattering angle

and $\langle A \rangle_{\mathrm{MC}}$ is the Monte Carlo prediction of the asymmetry.

Source	Correction	$\delta A/A(\%){:}1998$	$\delta A/A(\%){:}1999$
Statistics	-	13.3	7.2
P_e	-	7.0	3.4
Q^2	-	1.8	1.8
Background	1.2	0.6	0.6

Table 6.1: Summary of corrections and contributions to the errors in % for the measured asymmetry.

The final asymmetry is multiplied by this number for adjustment to the finite acceptance.

6.1.3 Q^2 scaling

The asymmetry from 1999 II and the corrected asymmetry from 1998 were scaled to the Q^2 value of the 1999 I measurement. These values were then combined into a final result shown in Table 6.1.3.

The combined asymmetry for all three run periods is

$$
\langle A \rangle = \frac{\sum\limits^{Run_i} A'_i(Q_i^2)W_i}{\sum\limits^{Run_i} W_i} = \frac{\sum\limits^{Run_i} \left(A_i(Q_i^2) + \Delta A_i \right) W_i}{\sum\limits^{Run_i} W_i}
$$

$$
= \frac{\sum\limits^{Run_i} \left(A_i(Q^2) + \left(\frac{\Delta A_{th}}{\Delta Q^2} \right) (Q_2^2 - Q_i^2) \right) W_i}{\sum\limits^{Run_i} W_i}
\tag{6.2}
$$

where Run is the data set: 1998, 1999 I, or 1999 II.

$\frac{\Delta A_{th}}{Q^2}$ is the Monte Carlo-calculated dependency of the theoretical asymmetry upon Q^2; $\frac{\Delta A_{th}}{Q^2} = 0.993$.

W_i is the weighting factor: $W_i = 1/\delta A_i^2$

6.1.4 Form Factors

The form factors used in the parameterization of A_{th} are given in Table 6.3. Also included are the percentage error in the asymmetry which is attributed to the particular form factor.

---

[1] "as published" discussed in 6.1.1

	A_{exp} (ppm)$\pm$(stat)$\pm$(sys)	Q^2 $(GeV/c)^2$
1998 (original[1])[104]	-14.50$\pm$ 2.0 $\pm$ 1.1	0.48
1998 (Corrected)	-14.720$\pm$ 2.23 $\pm$0.26	0.474
1999 I	-15.515$\pm$ 1.18 $\pm$0.27	0.477
1999 II	-14.040$\pm$ 2.83 $\pm$0.25	0.466
Combined	-15.049$\pm$ 0.98 $\pm$0.56	0.477

Table 6.2: Asymmetries after finite acceptance correction.

Form Factor	Value	Ref.	$\delta A_{th}/A_{th}$
$G_E^p/(G_M^p/\mu_p)$	0.99 ± 0.02	[105, 9]	3%
$G_E^n/(G_M^p/\mu_p)$	0.16 ± 0.03	[32, 33, 34, 35, 36]	4%
$(G_M^p/\mu_p)/(G_M^p/\mu_p)$	1.05 ± 0.02	[21]	2%
$G_M^n/\mu_n)/(G_M^p/\mu_p)$	1.12 ± 0.04	[20]	4%

Table 6.3: Electromagnetic form factors, normalized to (G_M^p/μ_p). For our kinematics, $(G_M^p/\mu_p) \sim 0.36$. The last column is the error in A_{th} due to the quoted error in the corresponding form factor.

6.2 Results

We measured a parity-violating electroweak asymmetry of

$$A_{\mathrm{pv}} = -15.05 \pm 0.98(\text{stat}) \pm 0.56(\text{syst}) \text{ ppm}. \tag{6.3}$$

at the kinematic point $\langle\theta_{\mathrm{lab}}\rangle = 12.3°$ and $\langle Q^2\rangle = 0.477(\text{GeV/c})^2$.

By using Eqn. 3.42 we extract a value for G^0 of

$$\frac{(G_E^0 + 0.392G_M^0)}{G_M^{\gamma p}/\mu_p} = 1.527 \pm 0.048(\text{stat}) \pm 0.027(\text{syst}) \pm 0.011(\text{theor}). \tag{6.4}$$

where the last term arises from uncertainties in the axial-vector term, A_A.

Using Eqn.3.43 next and the Mainz value for G_M^n[21], we extract a value for the linear combination of the strange quark form factors of

$$\frac{(G_E^s + 0.392G_M^s)}{G_M^{\gamma p}/\mu_p} = 0.069 \pm 0.056 \pm 0.039. \tag{6.5}$$

where the first error are the errors in G^0 combined in quadrature, and the second error is due to the uncertainties in the electromagnetic form factors.

From this we can extract the strangeness radius parameter as

$$\rho_s + 2.892\mu_s = 0.513 \pm 0.415 \pm 0.228 \tag{6.6}$$

Or, using the Bonn data for G_M^n[20], we have

$$\frac{(G_E^s + 0.392G_M^s)_{\mathrm{Bonn}}}{G_M^{\gamma p}/\mu_p} = 0.122 \pm 0.056 \pm 0.047, \tag{6.7}$$

from which we extract

$$\rho_s + 2.892\mu_s = 0.899 \pm 0.415 \pm 0.346 \tag{6.8}$$

The electromagnetic form factors remain a major source of uncertainty for $(G_E^s + 0.392G_M^s)$. There are experiments in progress [38, 39, 106, 107, 108]which will significantly improve the accuracy of the electromagnetic form factors. These new measurements could have significant impact on interpretations and the conclusions we may draw about strange form factors.

Also, there is yet considerable uncertainty in the calculation of the axial vector radiative corrections[57]. Determination of G_A is therefore of significant interest and addressing this will be a goal of future experiments[66].

While recent work has improved measurements of G_E^n[38, 36, 34] which reduces the uncertainties due to this form factor, error contributions from the electromagnetic form factors are still significant (see Table 6.3).

6.3 Summary and Implications

Separation of the strange form factors is difficult because all three of the electromagnetic form factors, $G_{E,M,(A)}^{n,p,s}$ contribute to the elastic scattering of electrons from the nucleon.

Large strange quark contributions to the vector matrix elements of the proton are ruled out by the present results. To contribute significantly to G_E^s, we require the $s\bar{s}$ pairs to have different radial distributions. This can be described by forming virtual meson-baryon intermediate states such as a ΛK^+ loops, etc.

Another possible explanation for the small signal of strangeness in the nucleon is that the signs for G_E^s and G_M^s might be opposite and thus tend to cancel each

other. This explanation can be tested by experiments which measure these form factors separately, such as the ^{4}He experiment discussed below.

In contrast to the small values indicated by the present work, the $\pi N\sigma$ term from pion-nucleon scattering is very different from theoretical values calculated with chiral perturbation theory at low energies. This suggests $\approx 35\%$ of the nucleon's mass may be carried by strange quarks.

Also, DIS experiments suggest strange quarks carry 10-20% of the nucleon's spin[46, 48].

Nevertheless, the present result is sufficient to reject the more extreme models for strange quark vector current contribution to the nucleon. Fig. 6.3 shows the present result in the parameter space of $\rho_s + 2.892\mu_s$ compared with the predictions of various models.
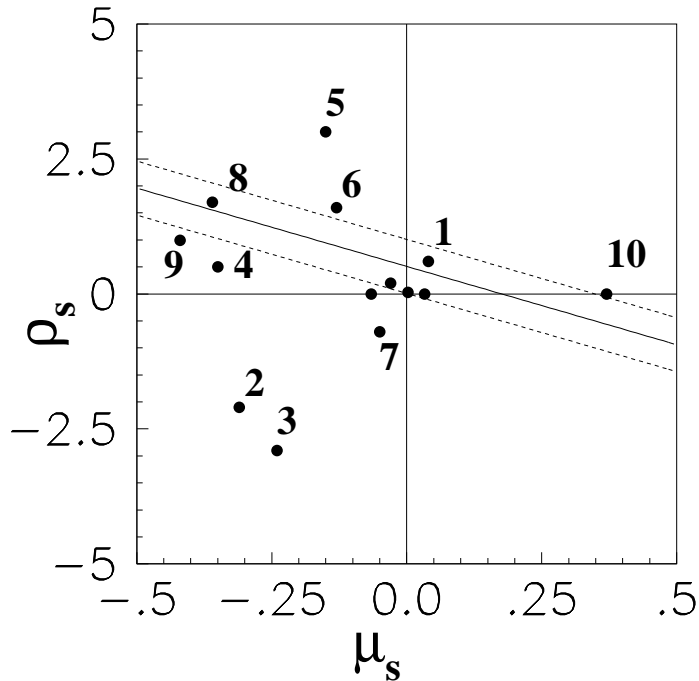
Figure 6.3: Parameter space of leading strangeness terms at low Q^2. The band is the allowed region from our results with assumptions listed in text. The points are estimates from various models.

| 1 | P. Geiger[56] | 3 | H. Hammer[50] | 5 | H Weigel[52] | 7 | N. Park[54] | 9 | H. Hammer[51] |
| 2 | R. Jaffe [49] | 4 | J Musolf[109] | 6 | N. Park[53] | 8 | S. Dong[55] | 10 | S.Hong[110] |

6.4 Future

The strange quark form factors may play a significant role in the important degrees of freedom for describing the nucleon. This experiment, HAPPEX I, has contributed one constraint on the size of strange quark contribution to the nucleon, at a particular Q^2. Additional work still needs to be done to determine the behavior of $G^s_{E,M}$ as a function of Q^2.

There are several experiments in work or planned to address this problem:

PVA4[111]: This parity violation experiment is currently running at Mainz (with $\frac{1}{2}$ of the detector complete). PVA4 will measure a forward angle asymmetry centered around $35°$ ($Q^2 = 0.23(GeV/c)^2$)). This will measure the combined form factors, $G^s_E + 0.21 G^s_M$. PVA4 uses a 20 μA, 855 MeV beam of 80% polarized electrons incident on a 10cm LH2 target. The detector is comprised of PbF_2 crystals arranged in a ring for a total solid angle of 0.7sr (see Fig. 6.4). The inelastic rates
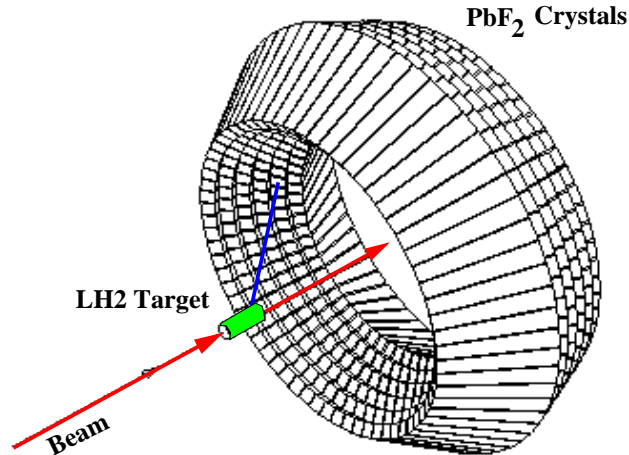
Figure 6.4: Schematic of PVA4 at Mainz.

will be about $\times 10$ larger than the elastic rates, however the fast Čerenkov signal in the PBF_2 allows electronic discrimination between the elastic and the inelastic events. PVA4 has taken approximately 800 hours of beam with about 150 hours analyzed showing that a sensitivity of $\Delta A = 2 \times 10^{-6}$ has been achieved.

SAMPLE01[64, 66]: This will run summer of 2001 at MIT-Bates; the goal is to further isolate G^s_M and to measure the effective axial current, G_A. SAMPLE

measures the Čerenkov signal of 200 MeV electrons elastically scattered from LH2 and deuterium targets (see Fig.6.5). A 40 μA beam of 35% polarized electrons is
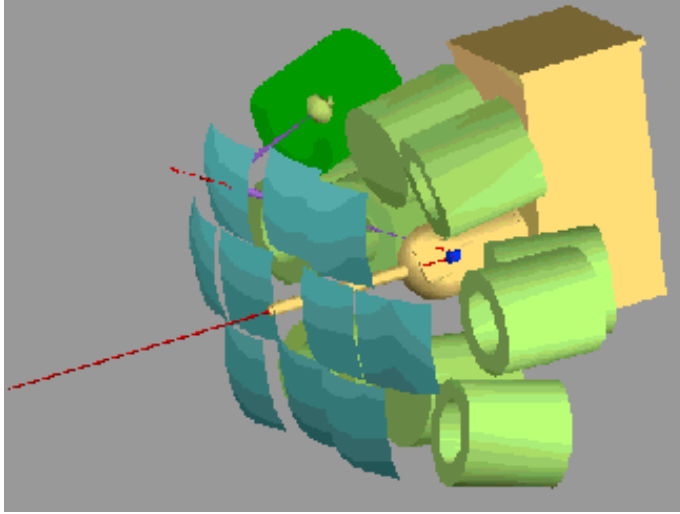
Figure 6.5: Schematic of SAMPLE at MIT-Bates.

scattered at backward angles of 130° to 170° ($Q^2 = 0.1(GeV/c)^2$)). As the counting rate in any one of the ten detector segments is on the order of 100 MHz, the signals are integrated as in HAPPEX. Where HAPPEX is sensitive to a combination of $G_E^s + \kappa G_M^s$, SAMPLE is sensitive to the combination of the strange magnetic form factor G_M^s and the axial form factor, G_A^s. Results from earlier data from SAMPLE are shown in Fig. 6.6.

G^0[72]: E91-017 is under construction at JLab. G^0 will measure the parity violating electroweak interference in the scattering of polarized electrons from the nucleon. At momentum transfers in the range of $Q^2 = 0.12 \leftrightarrow 1.0(GeV/c)^2$, G^0 will measure G_E^s, G_M^s and G_A and provide new data on these form factors at $Q^2 > 0.5(GeV/c)^2$. Asymmetries predicted by the Standard Model in the absence of strange quark contributions, vary from -3 to -35 ppm in this momentum regime. The measurement precision is designed to be $\Delta A/A < 5\%$. Fig. 6.7 shows the expected experimental error and some Lattice QCD theory predictions[55].

This experiment is a counting experiment with a spectrometer style detector system designed around a dedicated superconducting torodial magnet, as shown in Fig.6.8. The magnet is built of 8 coils to generate a 1.6 Tesla field. Elastically scattered particles will be momentum separated and focused by the magnet onto
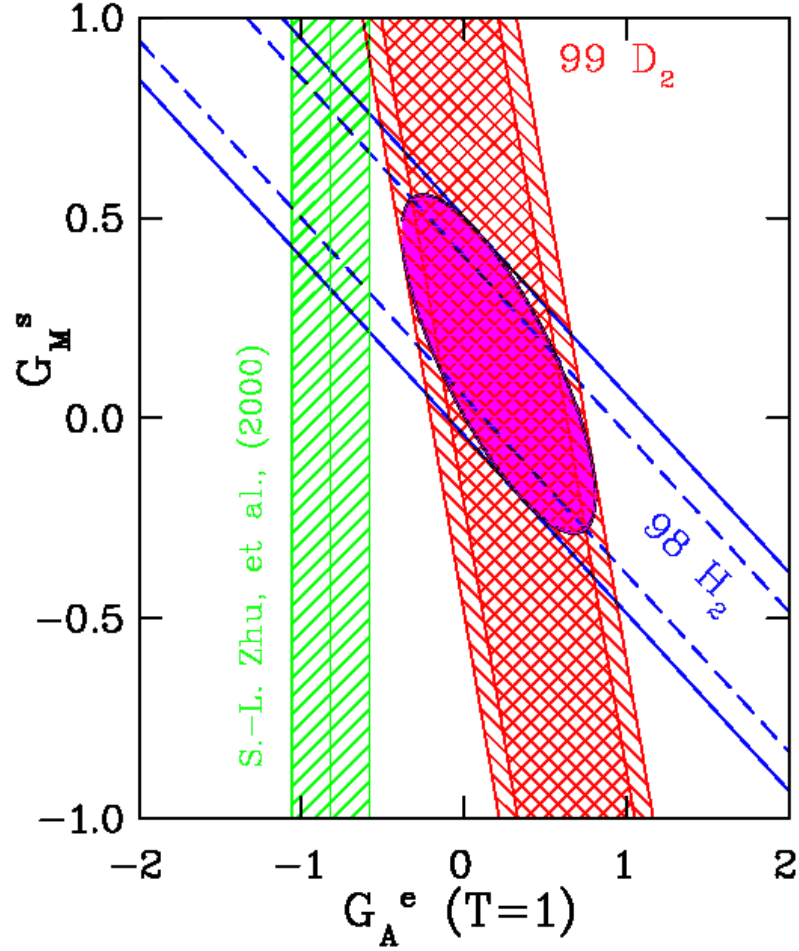
Figure 6.6: Results from SAMPLE on deuterium[66] and hydrogen targets[112]. The strange quark contribution to the protons magnetic moment (at $Q^2 = 0.1(GeV/c)^2$) is plotted vs. the isovector axial current.

a set of 16 pairs of scintillators located at various Q^2 positions on the focal plane. There are eight of these detector sets or 'octants' placed around the symmetry axis of the spectrometer to give a total solid angle of $\sim$0.8 sr. The G^0 experiment will be conducted in two phases.

In phase one, a 40μA beam of 70% polarized electrons will be scattered from protons in a 20cm LH2 target. G^0 will measure recoiling elastic protons from H($\vec{e}$,p) scattering at 3 GeV. Proton recoil angles of $\theta_p \simeq 70° \pm 10°$ correspond to an electron forward scattering angle of $\theta_e \simeq 7°$. To offset this small forward angle and its impact on the figure of merit, the 40μA beam will give an event rate on the order of 1 Mhz per octant.
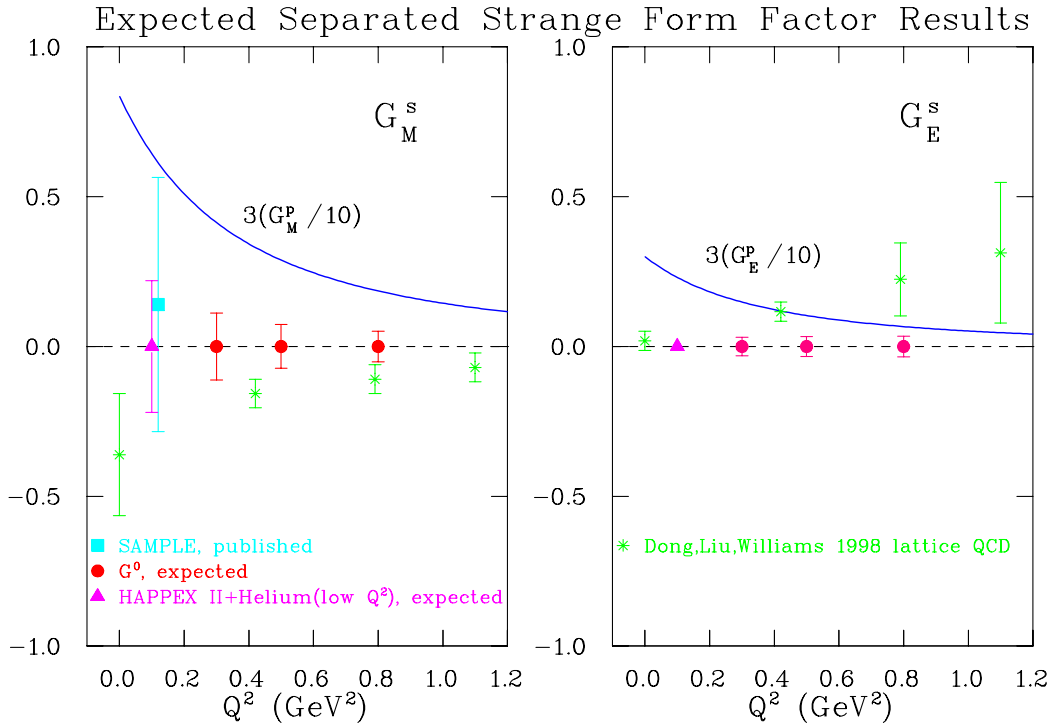
Figure 6.7: G^0 expected errors and some theoretical predictions[55].

In phase two, electrons will be detected scattered at backward angles of $\theta_e \simeq 110° \pm 10°$. This will be accomplished by rotating both the magnet and detector systems by 180° and reversing their relative positions. This puts the target and spectrometer downstream from the detector system allowing the detectors to then measure the backward scattered electrons. Separation of the form factors will follow a Rosenbluth method with $Q^2 =$ 0.3, 0.5, & 0.8 $(GeV/c)^2$ on a proton target. A deuterium target will also be used to separate the axial form factor, G_A, for a total of 6 measurements.

HAPPEX II[113]: E99-115 is tentatively scheduled to run in 2003. This experiment is an extension of HAPPEX I and will run at a significantly lower $Q^2 = 0.11(GeV/c)^2$ and will use a septum magnet to attain a $\theta_{\text{lab}} = 6°$ scattering angle. This forward angle will increase the cross-section at the low momentum transfers and hence the overall figure of merit. Much higher rates are expected than we saw in HAPPEX thus HAPPEX II will require a different detector setup. HAPPEX II will use a layered detector approach replacing the Lucite with Quartz which is
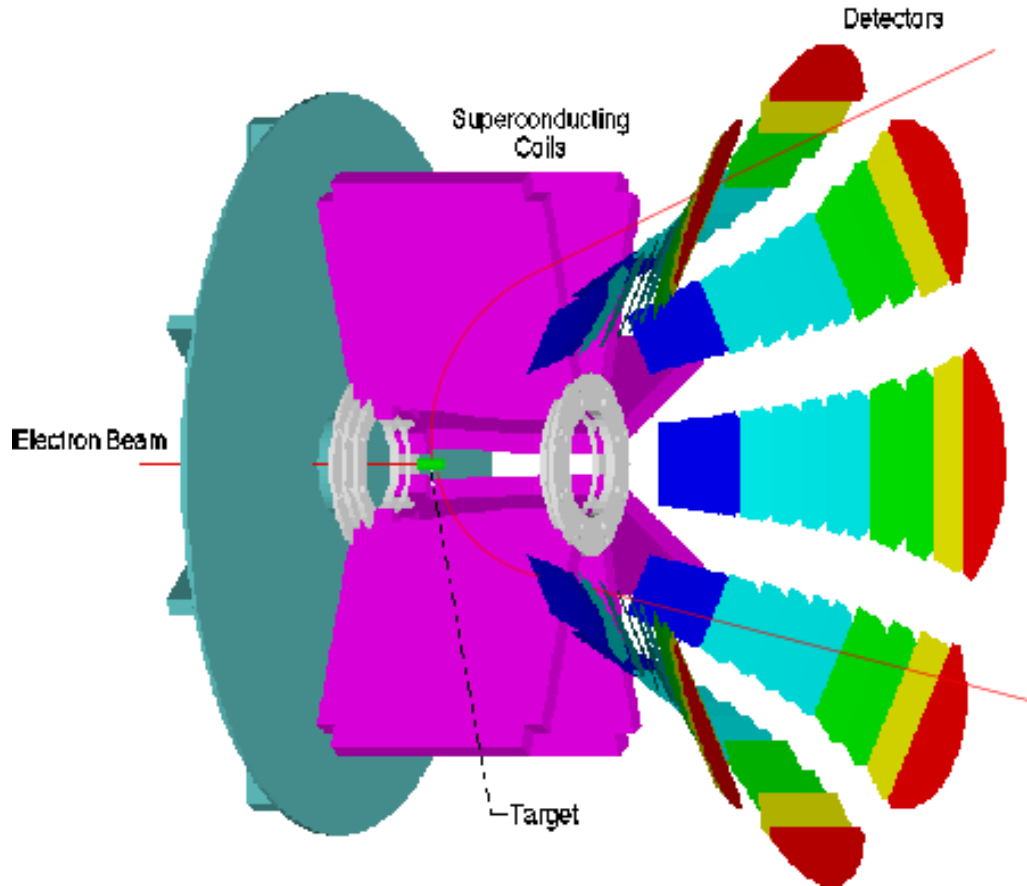
Figure 6.8: G^0 Detector schematic.

radiation hard. In addition, the detectors will be segmented to refine Q^2 weighting. The experiment will measure the elastically scattered electrons from the nucleus in a H($\vec{e}$,e') reaction using a 3.2 GeV beam of 75% polarized electrons. At these energies, the predicted asymmetry is estimated to be ~1.7 ppm. Running for 700 hours would yield a statistical error of 4.5% and a projected systematic error of 2.9%. This experiment will provide detailed information on the linear combination of $\rho_s + \mu_p \mu_s$ and set a direct constraint on the nucleon's strangeness radius. Results from this experiment combined with the results of the SAMPLE experiments will allow disentangling of ρ_s from μ_s.

^{4}**He**[114]: E-00-114. This experiment has been approved for 35 days running at

JLab using the $^4He(\vec{e}, e')$ reaction. ^{4}He will also use the Hall A septum magnets to attain a scattering angle of $\theta_{\text{lab}} = 6°$. With a beam energy of 3.2 GeV, the average momentum transfer will be $Q^2 = 0.1(GeV/c)^2$. Statistical errors are expected to be about 2.2%. As He is a 0^+, $T = 0$ nucleus, there can be no contribution from G_M or G_A making this a particularly clean measurement of G_E^s. This will allow extraction of the leading strange charge coefficient $\rho_s = \frac{dG_E^s(\tau)}{d\tau}$ at $\tau \to 0$ to an expected accuracy of ± 0.5. This should provide considerable insight as model predictions for ρ range from $-3 \leftrightarrow +3$. Combined with results from HAPPEX II, this will allow a complete extraction of ρ_s and μ_s from the linear combination $\rho_s + \mu_p\mu_s$.

These works will add significantly to the data required to establish the importance of the role of the strange sea of the nucleon. This information will go towards constraining current theoretical models and provide guidance for further development of the phenomenology of QCD.

"There is no excellent beauty that hath not some strangeness in the proportion."
— Sir Francis Bacon

Appendix A

Limits of LED Linearity

In order to simulate the PMT/base response to Čerenkov light (see Section 4.8.3.1), the signal LEDs were driven with 10ns to 50ns pulse-widths from a signal generator. These short pulse-widths are consistent with the pulse-widths of Čerenkov light. At these timing intervals, however, the LEDs do not operate in a linear fashion.

Driven with 10ns to 50ns pulse-widths the LEDs were not turning on fully. As a consequence the PMT was seeing only the early part of the rise time and some of the fall time as the LEDs turned off. The amount of rise and fall time were not constant due to diode characteristics in this fast transient regime of 10ns or so. The time dependent charge depletion across the diode junctions causes a change in the diode potential, which in turn affects the hole-carrier drift rate, which changes the recombination rate, which in turn, affects the charge depletion across the diode. The diode junction voltage (in a quasi-steady state approximation) during the turn-off transient varies according to:

$$v(t) = \frac{kT}{q} ln \left(\frac{I\tau_p}{qAL_pP_n} e^{-t/\tau_p} + 1 \right) \tag{A.1}$$

where P_n is the excess hole concentration.

τ_p is recombination time.

L_p is the hole diffusion length.

q is stored charge in the n-region.

This indicates that the voltage across a p-n junction cannot be changed instantaneously, and the stored charge can present a problem in fast switching applications with short transients. In addition, at the 10ns switching rate we needed, the diode behaves with a marked capacitance[115].

In short, the hole distribution does not remain in the convenient exponential form it has for a steady state. It is neither linear, nor predictably exponential. It is also temperature dependent. As light output follows the hole distribution and recombination, it also is neither linear nor predictably exponential. This limited the resolution of the linearity tests. To counter this problem, the LED pulse width was increased to $\approx$100ns. This increased the consistency of amount of light per pulse by allowing the diodes to turn on more fully. Due to the gain of the Burle 8854 PMTs[1] the resulting increase in light required increasing the width of the ADC gate and adding some delay. We increased the ADC gate width to the maximum of our equipment and subsequent testing, while better, still showed a non-linear effect due to the transient vagaries of the LEDs.

---

[1]typically 5.1×10^7 at $\sim$ 2000 volts

Appendix B

Optics Commissioning of the Hall A High Resolution Spectrometers[95]

Thanks to a lot of planning and hard work by many people we now have good optics databases that cover a large fraction of the momentum range of the HRS pair. During the last few months we have taken data required to calibrate the spectrometers at the remaining momenta. We are hoping to finish the analysis of this data by the end of the year. These would complete the set of databases that would cover the available momentum ranges of the HRS pair.

The optics data used for the recent optimizations were acquired during experiments e93050 (VCS) and e94010 (GDH). During these optimizations several improvements to the ESPACE optimizations procedures were made. These improvements would be extremely useful for the future optimization projects.[95]

B.1 Databases at 0.85 GeV/c

The Linear range of the high resolution spectrometers extends up to ~ 3.0 GeV/c. Thus a database optimized at 0.8 GeV/c works well over this whole range. The optics data obtained during the GDH experiment with a ^{12}C target stack covering the full y_{tg} range of the spectrometers were used to optimize the databases for both HRSE and HRSH at 0.85 GeV/c. As expected the obtained databases work well

155

from 0.4 GeV/c to 3.0 GeV/c for the whole y_{tg} range of $\pm$ 5 cm.

B.2   HRSE Databases above 3.0 GeV/c

The optics data taken during the VCS experiment provided the opportunity to optimize the HRSE optics database at 3.0 GeV/c and 3.5 GeV/c. These databases have similar resolutions and accuracies as the databases obtained at lower momenta. However the y_{tg} coverage is limited.

B.3   Summary of available databases

Spectrometer	Database	P range	Y_{tg} range
	0.85 GeV/c	up to 3.0 GeV/c	$\pm$ 5.0 cm
HRSE	3.0 GeV/c	2.8 GeV/c - 3.4 GeV/c	$\pm$ 3.0 cm
	3.5 GeV/c	3.3 GeV/c - 3.7 GeV/c	$\pm$ 2.0 cm
HRSH	0.85 GeV/c	0.4 GeV/c - GeV/c	$\pm$ 5.0 cm

Table B.1: Spectrometer Database Summary.

We have taken optics calibration data for HRSE at 4 GeV/c and for HRSH at 2.75 GeV/c. This data is being analyzed now.

Here are the accuracies and resolutions achieved with the available databases:

For 0.85 GeV/c electrons scattered off a a thin ^{12}C

- Angle determination accuracy

  - Transverse   0.15 mr

  - Dispersive   0.5 mr

- Angular resolution (FWHM)

  - Transverse   1.5 mr

  - Dispersive   6.8 mr

- Momentum resolution (FWHM)

    For $y_{tg} = 0$ 3×10^{-4}

    Overall 4.5×10^{-4}

- Transverse position determination

    $\pm$ 0.5 mm

- Transverse position resolution

    4.0 mm

The above angular and position resolutions are close to what can be expected at 0.85 GeV/c for this target configuration. However, the momentum resolution is about factor of 2 worse than expected. This can be attributed to the beam energy spread which has been measured to be about 2.5×10^{-4} (FWHM). Improvements in the beam energy width is expected to improve the momentum resolution to about 1×10^{-4} (FWHM) at the middle of the focal plane and to about 3×10^{-4} (FWHM) overall at 0.85 GeV/c.

B.4   Spectrometer constant calibration

The HRS spectrometer constants (Γ) have been known only at about the 2×10^{-3} level. The precision beam energy measurements using EP and Arc have made it possible to measure the spectrometer constants much more accurately. Therefore whenever a beam energy measurement was performed we have gathered data necessary for the calculation of Γ.

We use two methods to calculate the Γ's:

The direct method, where we measure elastic scattered electrons from 12C to directly calculate Γ for that spectrometer

The indirect method where we measure the missing energy of $1p_{1/2}$ state in ^{12}C(e,e'p) coincidence data. We then use this information with the already measured spectrometer constant of one spectrometer to derive Γ for the other spectrometer.

Using these two methods we have calculated the spectrometer constants of the two spectrometers at the momenta summarized below. We are planing to take more data in the next few months which would allow us to calculate the spectrometer

constants of both spectrometer over the full momentum ranges to 4×10^{-4} accuracy. Once both spectrometer constants have been measured to this level, a short ^{12}C(e,e'p) run can be used to calculate the beam energy to a similar accuracy eliminating the need to perform energy measurements frequently.

The tables below summarize the spectrometer constant values we have calculated with the available data.

Momentum (GeV/c)	Γ_{HRSH}	
2.73	269.4 ± 0.15	^{12}C(e,e'p)
1.88	269.2 ± 0.2	^{12}C(e,e'p)
0.61	268.4 ± 0.9	H(e,e'p)

Table B.2: Γ_{HRSH}

Momentum (GeV/c)	Γ_{HRSE}	
1.26	270.1 ± 0.1	^{12}C(e,e)
3.88	269.9 ± 0.2	^{12}C(e,e'p)

Table B.3: Γ_{HRSE}

Appendix C

List of Collaborators

K. A. Aniol,[1] D. S. Armstrong,[24] M. Baylac,[20] E. Burtin,[20] J. Calarco,[13]
G. D. Cates,[17] C. Cavata,[20] J.-P. Chen,[6] E. Chudakov,[6] D. Dale,[8] C. W. de Jager,[6]
A. Deur,[6,2] P. Djawotho,[24] M. B. Epstein,[1] S. Escoffier,[20] L. Ewell,[11] N. Falletto,[20]
J. M. Finn,[24] K. Fissum,[12] A. Fleck,[18] B. Frois,[20] J. Gao,[12] F. Garibaldi,[5]
A. Gasparian,[3] R. Gilman,[19] A. Glamazdin,[9] J. Gomez,[6] V. Gorbenko,[9]
O. Hansen,[6] F. Hersman,[13] R. Holmes,[22] M. Holtrop,[13] B. Humensky,[17] S. Incerti,[23]
J. Jardillier,[20] M. K. Jones,[24] J. Jorda,[20] C. Jutier,[16] W. Kahl,[22] D. H. Kim,[10]
M. S. Kim,[10] K. Kramer,[24] K. S. Kumar,[17] M. Kuss,[6] J. LeRose,[6] M. Leuschner,[13]
D. Lhuillier,[20] N. Liyanage,[12] R. Lourie,[21] R. Madey,[7] D. J. Margaziotis,[1]
F. Marie,[20] J. Martino,[20] P. Mastromarino,[17] K. McCormick,[16] J. McIntyre,[19]
Z.-E. Meziani,[23] R. Michaels,[6] G. W. Miller,[17] D. Neyret,[20] C. Perdrisat,[24]
G. G. Petratos,[7] R. Pomatsalyuk,[9] J. S. Price,[6] D. Prout,[7] V. Punjabi,[14]
T. Pussieux,[20] G. Quéméner,[24] G. A. Rutledge,[24] P. M. Rutt,[6] A. Saha,[6]
P. A. Souder,[22] M. Spradlin,[17,4] R. Suleiman,[7] J. Thompson,[24] L. Todor,[16]
P. E. Ulmer,[16] B. Vlahovic,[15] K. Wijesooriya,[24] R. Wilson,[4] B. Wojtsekhowski[6]

[1] California State University - Los Angeles, Los Angeles, CA 90032

[2] Universite de Clermont-Ferrand, F-63177 Auibière Cédex, France

[2] LPC, Universitè Blaise Pascal/IN2P3, F-63177 Aubière Cédex, France

[3] Hampton University, Hampton, VA 23668

[4] Harvard University, Cambridge, MA 02138

[5] Istituto Nazionale di Fisica Nucleare, Sezione Sanità, 00161 Roma, Italy

[6] Thomas Jefferson National Accelerator Laboratory, Newport News, VA 23606

[7] Kent State University, Kent, OH 44242

[8] University of Kentucky, Lexington, KY 40506

[9] Kharkov Institute of Physics and Technology, Kharkov 310108, Ukraine

[10] Kyungpook National University, Taegu 702-701, Korea

[11] University of Maryland, College Park, MD 20742

[12] Massachusetts Institute of Technology, Cambridge, MA 02139

[13] University of New Hampshire, Durham, NH 03824

[14] Norfolk State University, Norfolk, VA 23504

[15] North Carolina Central University, Durham, NC 27707

[16] Old Dominion University, Norfolk, VA 23508

[17] Princeton University, Princeton, NJ 08544

[18] University of Regina, Regina, SK S4S 0A2, Canada

[19] Rutgers, The State University of New Jersey, Piscataway, NJ 08855

[20] CEA Saclay, DAPNIA/SPhN, F-91191 Gif-sur-Yvette Cédex, France

[21] State University of New York at Stony Brook, Stony Brook, NY 11794

[22] Syracuse University, Syracuse, NY 13244

[23] Temple University, Philadelphia, PA 19122

[24] College of William and Mary, Williamsburg, VA 23187

Appendix D

LED Attenuation

Driven with 10ns to 50ns pulse-widthsthe LEDs were not turning on fully. As a consequence the PMT was seeing only the early part of the rise time and some of the fall time as the LEDs turned off. The amount of rise and fall time were not constant due to diode characteristics in this fast transient regime of 10ns or so. The time dependent charge depletion across the diode junctions causes a change in the diode potential, which in turn affects the hole-carrier drift rate, which changes the recombination rate, which in turn, affects the charge depletion across the diode. The diode junction voltage (in a quasi-steady state approximation) during the turn-off transient varies according to:

$$v(t) = \frac{kT}{q} ln \left(\frac{I\tau_p}{qAL_pP_n} e^{-t/\tau_p} + 1 \right) \tag{D.1}$$

Where P_n is the excess hole concentration.
τ_p is recombination time.
L_p is the hole diffusion length.
q is stored charge in the n-region.

This indicates that the voltage across a p-n junction cannot be changed instantaneously, and the stored charge can present a problem in fast switching applications with short transients. In addition, at the 10ns switching rate we needed, the diode behaves with a marked capacitance. [115].

In short, the hole distribution does not remain in the convenient exponential form it has for a steady state. It is neither linear, nor predictably exponential. It

is also temperature dependent. As light output follows the hole distribution and recombination, it also is neither linear nor predictably exponential. This limited the resolution of the linearity tests. To counter this problem, the LED pulse width was increased to ≈100ns. This increased the consistency of amount of light per pulse by allowing the diodes to turn on more fully. Due to the gain of the Burle 8854 PMTs[1] the resulting increase in light required increasing the width of the ADC gate and adding some delay. We increased the ADC gate width to the maximum of our equipment and subsequent testing, while better, still showed a non-linear effect due to the transient vagaries of the LEDs.

---

[1]typically 5.1×10^7 at ~ 2000 volts

Appendix E

Support

Appendix F

VITA

Gary A. Rutledge

College of William & Mary, Williamsburg, Virginia
E-mail: rutledge@jlab.org

EDUCATION

Ph.D., Nuclear and Particle Physics, December 2000
College of William & Mary
Dissertation: *Measurement of the Strange Sea of the Proton*

M.S., Nuclear and Particle Physics, January 1996
College of William & Mary

B.S., Physics, June 1994
Western Washington University

A.A.S., Electronics Technologies, June 1988
Green River Community College.

F.1 Publications

K.A. Aniol *et al.* (The HAPPEX Collaboration), *Measurement of the Neutral Weak Form Factors of the Proton*, Phys. Rev. Lett., **82**, 1096 (1999).

L.C. Alexa *et al.* (The Jefferson Lab Hall A Collaboration), *Measurements of the Deuteron Elastic structure Function $A(Q^2)$ for $0.7 \leq Q^2 \leq 6.0$ $(GeV/c)^2$ at Jefferson Laboratory*, Phys. Rev. Lett., **82**, 1374 (1999).

J.Gao *et al.*, *Dynamical Relativistic Effects Observed in Quasielastic 1p-Shell Proton Knockout from ^{16}O*, Phys. Rev. Lett., **84:15**, 3265, (10 April 2000)

M.K.Jones *et al.*, *G_E^p/G_M^p ratio from 0.5 to 3.5 $(GeV/c)^2$ by polarization transfer in $\vec{e}p \rightarrow e'\vec{p}$*. Phys. Rev. Lett., **84**, 1398, (2000)

K.A. Aniol *et al.* (The HAPPEX Collaboration), *New Measurement of the Weak Neutral Current of the Proton and Implications for Strange Form Factors*, Submitted to Phys. Lett. B, (25 May 2001).
(Preprint at arXiv:nucl-ex/0006002 v3 12 Apr 2001)

N. Liyanage *et al.*, *Dynamics of the $^{16}O(e,e',p)$ Reaction at High Missing Energies*, Phys. Rev. Lett., **86**, 5670, (2001)

S.Malov, *et al.*, *Polarization transfer in the $^{16}O(\vec{e},e'\vec{p})^{15}N$* , Phys. Rev. C., **62**, 57302, (2001)

'A good book is the precious life-blood of a master-spirit,
embalmed and treasured up on purpose to a life beyond life.'
- **Milton,** *Areopagitica*

Bibliography

[1] B. Povh, K. Rith, C. Scholz, and F. Zetsche. *Particles and Nuclei, An introduction to the Physical Concepts.* Springer, (1995).

[2] L.I. Schiff. *Rev. Mod. Phys.*, **30**:462, (1958).

[3] D.H. Perkins. *Introduction to High Energy Physics.* Addison-Wesley, 3 edition, 1987.

[4] R.G. Sachs, F.J. Ernst, and K.C. Wali. *Phys. Rev.*, **119**:1105, (1960).

[5] M.N. Rosenbluth. *Phys. Rev. Lett.*, **79**:625, (1950).

[6] P. Bosted, *et al.,* *Phys. Rev. C*, **51**:409, (1995).

[7] G. Höhler, *et al.,* *Nucl. Phys. B*, **114**:718, (1976). , and references therein.

[8] R. Hofstadter. *Ann. Rev. Nucl. Sci.*, **7**:231, (1977).

[9] M.K. Jones, *et al.,* *Phys. Rev. Lett.*, **84**:1398, (2000).

[10] M.F. Gari and W. Z. Krümpelmann. *Z. Phys. A*, **322**:689, (1985).

[11] P.L. Chung and F. Coester. *Phys. Rev. D*, **44**:229, (1991).

[12] M.F. Gari and W. Z. Krümpelmann. *Phys. Lett. B*, **274**:159, (1992).

[13] D.H. Lu, A.W. Thomas, and A.G. Williams. *Phys Rev. C*, **57**:2628, (1998).

[14] P. Mergell, *et al.,* *Nucl. Phys. A*, **596**:367, (1996).

[15] P. Kroll, M. Scürmann, and W.Schweiger. *Z. Phys. A*, **338**:339, (1991).

[16] R. Arnold, C. Carlson, and F. Gross. *Phys. Rev. C.*, **23**:363, (1981).

[17] B. Milbrath, *et al.,* *Phys. Rev. Let.*, **80**:452, (1998). erratum,*Phys. Rev. Lett.***82**,2221(1999).

[18] D. Dutta. Precision measurement of the neutron magnetic form factor from $^3\vec{H}e(\vec{e}, e')$. CIPAN, (2000).

[19] H. Gao and O. Hansen, (spokespersons). Jlab experiment e94-001. (unpublished).

[20] E.E.W. Bruins, *et al., Phys. Rev. Lett.*, **75**:21, (1995).

[21] H. Anklin, *et al., Phys. Lett. B.*, **428**:248, (1998).

[22] H. Anklin, *et al., Phys. Lett. B.*, **336**:313, (1998).

[23] P. Markowitz, *et al.,* Measurement of the magnetic form factor of the neutron. *Phys. Rev. C*, **48**(1), 1993.

[24] H. Gao, *et al., Phys. Rev. C*, **50**:546, (1994).

[25] S. Platchkov, *et al., Nucl. Phys. A*, **510**:740, (1990).

[26] C.E. Woodward, *et al., Phys. Rev. Lett.*, **65**:698, (1990).

[27] C.E Jones-Woodward, *et al., Phys. Rev. C*, **44**:571, (1991).

[28] A.K. Thompson, *et al., Phys. Rev. Lett.*, **68**:2901, (1992).

[29] T. Eden, *et al., Phys. Rev. C*, **50**:1794, (1994).

[30] M. Meyerhoff, *et al., Phys. Lett. B*, **327**:201, (1994).

[31] K. de Jager. *Nucleon Electromagnetic Form Factors*. Bates 25 Symposium, (2000). JLab internal publication [JLAB-PHY-00-01] and references therein.

[32] I. Passchier, *et al., Phys. Rev. Lett.*, **82**:4988, (1999).

[33] C. Herberg, *et al., Eur. Phys. Jour. A*, **5**:131, (1999).

[34] M. Ostrick, *et al., Phys. Rev. Lett.*, **83**:276, (1999).

[35] J. Becker, *et al., Eur. Phys. Jour.*, A**6**:329, (1999).

[36] D. Rohe, *et al., Phys. Rev. Lett.*, **83**:4257, (1999).

[37] M. Ferro-Luzzi and J.F.J. van den Brand. NIKHEF experiment 94-05. (unpublished).

[38] B.D. Anderson, S. Kowalski, and R. Madey, (spokespersons). Jlab experiment E93-038. (unpublished).

[39] J. Mitchell and D. Day, (spokespersons). JLab experiment E93-026. (unpublished).

[40] U.-G Meissner. *Nucl. Physc. A*, **51**:666, (2000).

[41] S. Galster, *et al., Nucl. Phys. B*, **32**, (1971).

[42] E.W. Hughes and R. Voss. Spin structure functions. *Annu. Rev. Nucl. Part. Sci.*, **49**:303–339, (1999). and references therein.

[43] J. Ashman, *et al.*, (EMC). *Phys. Lett. B*, **206**:364, (1988).

[44] J. Ashman, *et al., Nucl. Phys. B*, 328:1, (1989).

[45] M.J. Musolf, *et al., Phys. Rep.*, **239**:1, (1994).

[46] K. Abe, *et al.*, (E154 Collaboration). *Phys. Rev. Lett.*, **79**:26, (1997).

[47] K. Abe, *et al.*, (E154 Collaboration). *Phys. Lett. B*, **404**:377, (1997).

[48] B. Adeva, *et al.*, (SMC). *Phys. Rev. D*, **58**:112001, (1997). and references therein.

[49] R.L. Jaffe. *Phys. Lett. B*, **229**:275, (1989).

[50] Ulf-G. Meisner, H.-W. Hammer, and D. Dreschel. *Phys. Lett. B*, **367**:323, (1996).

[51] M.J. Ramsey-Musolf, H.W. Hammer. *Phys. Rev. C*, **60**:045204, (1999). [hep-ph/9903367].

[52] A. Abada, H. Weigel, R. Alkofer, and H. Reinhardt. *Phys. Lett. B*, **353**:20, (1995).

[53] J. Schecter, N.W. Park, and H. Weigel. *Phys. Rev. D*, **43**:869, (1991).

[54] N.W. Park and H. Weigel. *Orsay report IPNO*, TH 91-57, (1991).

[55] S.J. Dong, K.F. Liu, and A.G. Williams. *Phys. Rev. D*, **58**:074504, (1998). [hep-ph/9712483].

[56] P. Geiger and N. Isgur. *Phys. Rev. D*, **55**:299, (1997). [hep-ph/9610445].

[57] R.D. McKeown. *Parity Violation in Electron Scattering.* (1997). (presented at PAVI 97).

[58] Ia. B. Zeldovich. *Zh. Eksp. Teor. Fiz.*, **33**:1531, (1957). [*Sov. Phys. -JETP*, **6**, 1184 (1985)].

[59] P.A. Souder. *Parity Violation I: Then and Now.* (unpublished).

[60] C. Prescott, *et al.,* *Phys. Lett. B*, **77**:347, (1978).

[61] P.A. Souder, *et al.,* *Phys. Rev. Lett.*, **65**:694, (1990).

[62] K. Kumar. *Parity Violation in Elastic Electron Carbon Scattering.* PhD thesis, Syracuse University, 1990. (unpublished).

[63] W. Heil, *et al.,* *Nucl. Phys. B*, **327**:1, (1989).

[64] B.A. Mueller, *et al.,* *Phys. Rev. Lett.*, **78**:3824, (1997).

[65] B.A. Mueller. PhD thesis, California Institute of Technology, (1997). (unpublished).

[66] R. Hasty, *et al.,* *Science*, 290:221, (2000). Preprint: arXiv:nucl-ex/0102001 v1 3 Feb 2001.

[67] D.J. Griffiths. *Introduction to Elementary Particles.* Harper & Row, (1987).

[68] F. Halzen and I.A. Martin. *Quarks & Leptons:An Introductory Course in Modern Particle Physics.* Wiley & Sons, (1984).

[69] P.A. Souder. Strange quarks and parity violation. HUGS. (unpublished), TJNAF, 1999.

[70] M.J. Musolf and T.W. Donnelly. *Phys. Lett.*, **B318**:263, (1993).

[71] K.A. Aniol, *et al.,* (HAPPEX Collaboration). *Phys. Lett. B*, **509**(3-4):211–216, (2001).

[72] D. Beck, *et al.,* Jefferson Lab Proposal PR-00006, *G0 Experiment - Forward Angle Measurements.* accepted by PAC17. (unpublished).

[73] CEBAF. *Conceptual Design Report.* 1990. (unpublished).

[74] J. Kessler. *Polarized Electrons,* 2nd ed. Springer Series on Atoms and Plasma, vol. 1. Springer, New York, 1985.

[75] G.W. Miller. PhD thesis, Prinston University, (2000). (unpublished).

[76] G.D. Cates, *et. al. Nucl. Instrum. Methods A*, **278**:293, (1989).

[77] J.D. Bjorken and S.D. Drell. *Relativistic Quantum Mechanics.* McGraw-Hill, 7th edition, 1964.

[78] H.R. Band, *et al.,* *Nucl. Instrum. Methods A*, **400**:24, (1997).

[79] A.Glamazdin, *et al.*, *Fizika*, B(**8**):91, (1999).

[80] E. Chudakov, 1999. private communication. (unpublished).

[81] M. Baylac. PhD thesis, l'Universite Claude Bernard - Lyon I, February (2001). (unpublished).

[82] K. Unser. *IEEE Trans. Nucl. Sci.*, **16**:934, (1969). ; **28**:2344, (1981).

[83] K. Unser. *Design and Preliminary Test of a Beam Intensity Monitor for LEP.* Proc. IEEE Particle Acc. Conf., Chicago, IL, 71, (1989).

[84] K.G. Fissum, *et al.*, *VDC Manual V2.1.* MIT-LNS internal report #03, (1997). (unpublished).

[85] BURLE Company Catalog. *BURLE Photomultipliers*, (1995). pp. 26-27.

[86] T.M. Flynn. *Cryogenic Engineering.* Marcel Dekker, Sept. (1996).

[87] K.R. McCormick. *Measurement of the Deuteron Elastic Struture Functions at Large Momentum Transfers.* PhD thesis, Old Dominion University, VA, August (1999). (unpublished).

[88] R. S. Suleiman. *Measurement of the Electric and Magnetic Elastic Structure Functions of the Deuteron at Large Momentum Transfers.* PhD thesis, Kent State, (1999). (unpublished).

[89] B. Dalesio, *et al.*, *Experimental Physics and Industrial Control System (EPICS) Overview.* Technical report, May (1998). http://www.atdiv.lanl.gov/aot8/epics/training/New/EPICS_Overview/index.htm.

[90] K.R. McCormick. *TJNAF Hall A Cryotarget Density Dependence on Beam Current.* Technical report, TJNAF. (unpublished).

[91] *CODA Users Manual*, (1995).

[92] G.W. Miller, (2000). private communication. (unpublished).

[93] E.A.J.M Offerman. *ESPACE Users Guide.* Technical report, TJNAF, (1997). unpublished.

[94] P. Bertin Spokesperson. Nucleon Structure Study By Virtual Compton Scattering. (unpublished).

[95] N Liyanage. *Optics Commissioning of the Hall A High Resolution Spectrometers.* Technical report, TJNAF, (2000). unpublished.

[96] Juncai Gao. *Beam Energy Measurement at Jefferson Lab Using the Hall A Spectrometers.* Technical Report #04/98, MIT-LNS, (1998). unpublished.

[97] J.J. LeRose. *Collimator Surveys.* Technical report, March (1999). http://hallaweb.jlab.org/news/minutes/collimator-distance.html.

[98] N. Liyanage, (1999). private communication. (unpublished).

[99] L. Tudor, (1998). private communication. (unpublished).

[100] B. Michaels and E. Chudakov. *Empirical study of scintillator timing distortions.* JLab technical note. (unpublished), (1999).

[101] T.W. Donnelly and M.J. Musolf. *Nucl.Phys. A*, **550**:509, (1992). Erratum-ibid **A 550** (1992) 564.

[102] R. Micheals. Happex backgrounds. (1999). Detailed HAPPEX report (in work).

[103] K. McFarlane. *GUIDEM V0.0.* Technical report, TJNAF, (1997). A modified version of GUIDEIT. (unpublished).

[104] K.A. Aniol, *et al.,* (HAPPEX Collaboration). *Phys. Rev. Lett.,* **82**:1096, (1999).

[105] R.C. Walker, *et al., Phys. Rev. D,* **49**:5671, (1994).

[106] V. Punjabi, E. Brash,, M. Jones, and C. Pedrisat, (spokesperson). *Measurement of G_E^p/G_E^p to $Q^2 = 5.6$ $(GeV/c)^2$ by the Recoil Polarization Method.* Jlab experiment E99-007. (unpublished).

[107] R. Segel,and J. Arrington,. *New Measurement of G_E/G_M for the Proton.* Jlab experiment E-01-001. (unpublished).

[108] V. Punjabi, E. Brash, and C. Pedrisat, (spokesperson). *Measurement of G_E^p/G_E^p to $Q^2 = 5.6$ $(GeV/c)^2$ by the Recoil Polarization Method.* Jlab experiment E01-109. (unpublished).

[109] M.J. Musolf, R. Schivailla, and T.W. Donnelly. *Phys. Rev. C,* **50**:2173, (1994).

[110] S-T. Hong, D-P. Min, and B-Y. Park. *Phys. Lettt. B,* **414**:R1750, (1997).

[111] F. Mass, and D. von Harrach, (spokesperson). MAMI-Mainz PV-A4 Proposal. (unpublished).

[112] D.T. Spayde, *et al., Phys. Rev. Lett.,* **84**:1106, (2000).

[113] K.S. Kumar and D. Lhuillier, Spokespersons. Jefferson Lab proposal PR-99115, *Constraining the Nucleon Strangeness Radius in Parity Violating Electron Scattering.* accepted by PAC16.

[114] D. Armstrong and R. Michaels, Spokespersons. Jefferson Lab proposal PR-00-114. accepted by PAC16.

[115] B. Streetman. *Solid State Electronic Devices.* Prentice Hall, 3 edition, (1990).

Colophon

This document was Typeset useing LATEX

Index and displayed reference labels can be acheived by using a latex package called "showkeys.sty". This is invoked in the normal way by '\usepackage{showkeys}'. Very helpful. The keys are turned off by commenting out the invoking command.

Copies available by request in postscript or PDF

GRutledge_thesis.ps.gz
GRutledge_thesis.pdf.gz

Having finished feels....strange...